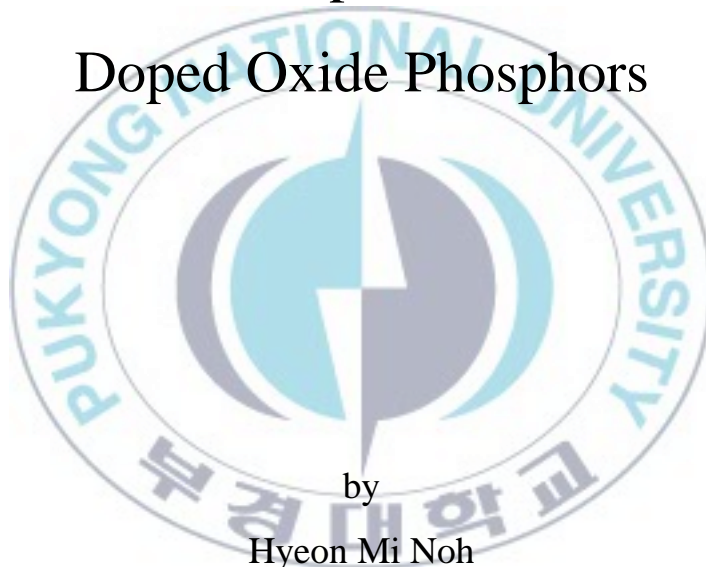


Thesis for the Degree of Doctor of Philosophy

Synthesis and Upconversion
Luminescence Properties of Lanthanide
Doped Oxide Phosphors



by

Hyeon Mi Noh

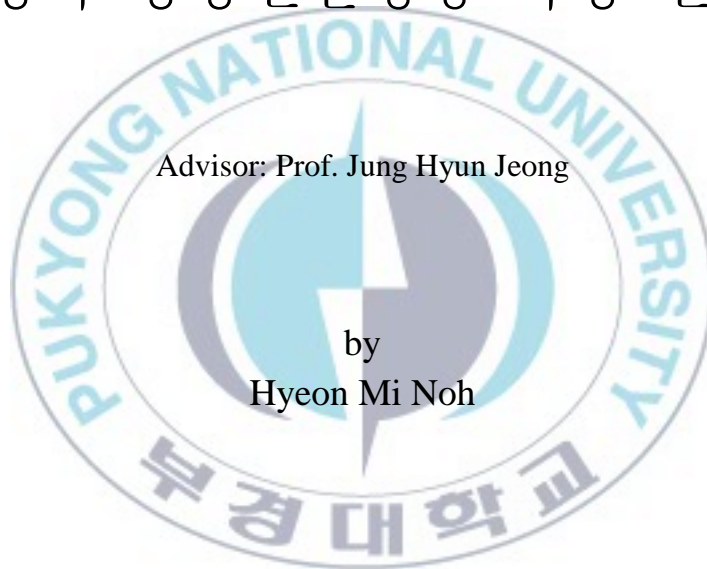
Department of Physics

The Graduate School

Pukyong National University

August 2014

Synthesis and Upconversion
Luminescence Properties of Lanthanide
Doped Oxide Phosphors
(란탄족이 도핑된 산화물형광체의
합성과 상방전환형광 특성 연구)



Advisor: Prof. Jung Hyun Jeong

by
Hyeon Mi Noh

A thesis submitted in partial fulfillment of the requirements
for the degree of Doctor of Philosophy

Department of Physics, The Graduate School,
Pukyong National University

August 2014

Synthesis and Upconversion Luminescence Properties of
Lanthanide Doped Oxide Phosphors

A dissertation
by
Hyeon Mi Noh

Approved by:

Prof. Jung Hwan Kim
Chairman of Committee

Prof. Byung Chun Choi
Member of Committee

Prof. Kiwan Jang
Member of Committee

Prof. Byung Kee Moon
Member of Committee

Prof. Jung Hyun Jeong
Member of Committee

June 24, 2014

Contents

Abstract.....	ix
----------------------	-----------

I. Introduction	1
------------------------------	----------

1.1 Description of phosphors.....	1
-----------------------------------	---

1.2 Upconversion phosphors	2
----------------------------------	---

1.3 Host and activator materials	3
--	---

1.3.1 Yttrium aluminium garnet ($Y_3Al_5O_{12}$) and yttrium aluminium perovskite ($YAlO_3$).....	3
--	---

1.3.2 Zirconium oxide (ZrO_2).....	5
--	---

1.3.3 ABO_4 (A=Ca, Sr; B=W, Mo) compounds	6
---	---

1.3.4 Properties of Er^{3+} , Ho^{3+} and Yb^{3+} ions	7
--	---

1.4 Purpose and outline	8
-------------------------------	---

II. Upconversion processes	10
---	-----------

2.1 Conversion of low-energy incident radiation into higher-energy emitted radiation	10
---	----

2.2 UC mechanisms.....	12
------------------------	----

2.2.1 Excited State Absorption (ESA).....	13
---	----

2.2.2 Energy Transfer Upconversion (ETU).....	16
---	----

2.2.3 Cooperative luminescence.....	18
2.2.4 Cooperative sensitization.....	20
2.2.5 Photon avalanche in UC.....	20
2.3 Rate equations relevant to UC process.....	22
2.3.1 Rate equations in a three-level system.....	22
2.3.2 Pump power dependence in ESA is dominant over ETU.....	25
2.3.3 Pump power dependence in ETU is dominant over ESA.....	26
2.4 Center Luminescence.....	26
2.5 Rare earth upconverter.....	29
2.6 Applications of UC.....	35
2.7 UC nanoparticles.....	37
III. Experimental Methods.....	39
3.1 Synthesis methods.....	39
3.1.1 Conventional solid state reaction and planetary ball milling method	39
3.1.2 Solvothermal method.....	41
3.2 Characterization Techniques.....	43
3.2.1 X-ray diffractometer (XRD).....	43
3.2.2 Field emission Scanning Electron Microscope (FE-SEM).....	45
3.2.3 Upconversion spectrophotometer.....	45

IV. Results and Discussions	47
4.1 UC luminescence properties of Er ³⁺ doped YAlO ₃ (YAP) nanophosphors	47
4.2 UC luminescence properties of Er ³⁺ and Yb ³⁺ co-doped zirconium oxide	60
4.3 UC luminescence properties of Ho ³⁺ and Yb ³⁺ co-doped zirconium oxide	75
4.4 Li doping effects on the UC luminescence of Yb ³⁺ /Er ³⁺ -doped ABO ₄ (A=Ca, Sr; B=W, Mo).....	87
V. Conclusions	101
References	104

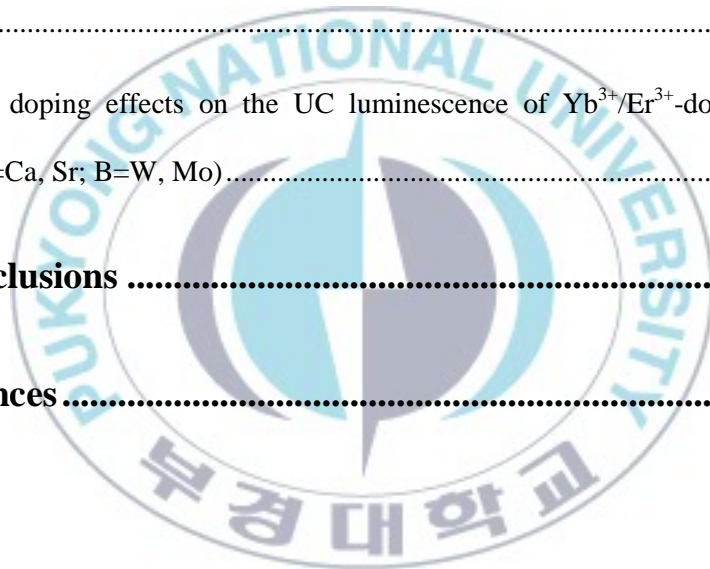


Table List

Table 2.1 Tabulation of the basic properties of the trivalent rare earth elements	30
Table 3.1 Specifications of FE-SEM	45
Table 4.1 Lattice constants of ABO_4 ($A = Ca, Sr; B = W, Mo$) phosphors tri- doped with 5 mol% of Er^{3+} , 10 mol% of Yb^{3+} and different concentration of Li^+ ions	92



Figure List

Figure 2.1 Various processes involved in the conversion of low-energy incident radiation into higher-energy emitted radiation and their typical values are associated with them.....	11
Figure 2.2 Four important upconversion energy transfer processes. (a) Ground-State Absorption (GSA), (b) Excited-State Absorption (ESA), (c) Energy Transfer Upconversion (ETU) and (d) Cross-Relaxation	14
Figure 2.3 (a) Schematic representation of ESA process and (b) characteristic time response curve of the up converted emission	15
Figure 2.4 (a) Schematic representation of ETU process and (b) characteristic time response curve of the up converted emission	17
Figure 2.5 Schematic representation of the cooperative luminescence process	19
Figure 2.6 Schematic representation of a three-level system for understanding avalanche UC.....	21
Figure 2.7 Schematic representations of UC processes in a three-level system	24
Figure 2.8 Schematic representation of the configurational coordination diagram	28
Figure 2.9 Illustration of the <i>Dieke diagram</i> : energy levels of lanthanide ions	31
Figure 2.10 Illustration of the energy level diagrams of Yb^{3+} , Er^{3+} and Tm^{3+}	34
Figure 2.11 Diagrammatic representation of the variety of applications of UC materials	36

Figure 3.1 Depiction of the planetary ball mill “Pulverisette 5” and its working mechanism involved.....	40
Figure 3.2 (a) Autoclave system and (b) schematic diagram of solvothermal synthesis setup. (1) Stainless steel autoclave (2) precursor solution (3) teflon liner (4) stainless steel lid (5) spring	42
Figure 3.3 X-ray diffractometer (X’PERT PRO, PHILIPS).....	44
Figure 3.4 Schematic representation of the UC photoluminescence system.....	46
Figure 4.1 XRD patterns of YAP:Er ³⁺ nanophosphors and the reference data of JCPDS card No. 32-0382 for orthorhombic YAP	49
Figure 4.2 SEM image of YAP:Er ³⁺ nanophosphors.....	51
Figure 4.3 UC luminescence spectra of YAP:Er ³⁺ with different concentrations under the excitation of 975 nm LD.....	52
Figure 4.4 Energy level diagram of the Er ³⁺ ions and mechanisms for the UC luminescence in YAlO ₃	55
Figure 4.5 Pump power dependence of UC photoluminescence in YAP nanophosphors doped with (a) 0.01 mol and (b) 0.07 mol Er ³⁺ ions	56
Figure 4.6 XRD patterns of ZrO ₂ :Er ³⁺ and ZrO ₂ :Er ³⁺ co-doped with different concentrations of Yb ³⁺ sintered at 800 ~ 1200 °C.....	63
Figure 4.7 SEM images for different of Yb ³⁺ co-doped ZrO ₂ :Er ³⁺ phosphors sintered at 1000 °C	64
Figure 4.8 UC emission spectra of Yb ³⁺ co-doped ZrO ₂ :Er ³⁺ at 800 ~ 1200 °C with (a) 0, (b) 0.01, (c) 0.05 and (d) 0.1 mol of Yb ³⁺	66
Figure 4.9 UC spectra of ZrO ₂ :Er ³⁺ , Yb ³⁺ phosphors at 1000 °C. The inset shows the intensity ratio of red to green emission.....	67
Figure 4.10 CIE chromaticity coordinates of Er ³⁺ , Yb ³⁺ co-doped ZrO ₂ with increasing Yb ³⁺ concentrations.....	69

Figure 4.11 Schematic energy level diagrams of the Er^{3+} and Yb^{3+} ions along with the proposed mechanism	72
Figure 4.12 Pump power dependence of the UC emission band centered at (a) 550 and (b) 660 nm.....	73
Figure 4.13 XRD patterns of $\text{ZrO}_2:\text{Ho}^{3+}$ and different concentrations of Yb^{3+} co-doped $\text{ZrO}_2:\text{Ho}^{3+}$ sintered at 1000 °C	78
Figure 4.14 (a) SEM image and (b) energy-dispersive X-ray (EDX) spectroscopy of $\text{ZrO}_2:\text{Ho}^{3+}$, Yb^{3+} sample	79
Figure 4.15 UC emission spectra of 1 mol% Ho^{3+} and various Yb^{3+} concentrations under 975 nm LD	81
Figure 4.16 UC emissions peaked at 550, 660 and 757 nm with the increase of Yb^{3+} concentrations	82
Figure 4.17 Pump power dependence of 550 and 660 nm UC emissions of 1 mol% $\text{Ho}^{3+}/7$ mol% Yb^{3+} co-doped ZrO_2	84
Figure 4.18 Schematic energy level diagrams of Ho^{3+} and Yb^{3+} ions along with the proposed UC mechanism.....	85
Figure 4.19 XRD patterns of (a) CaWO_4 , (b) CaMoO_4 , (c) SrWO_4 and (d) SrMoO_4 tri-doped with 5 mol% of Er^{3+} , 10 mol% of Yb^{3+} and different concentration of Li^+ ions.....	89
Figure 4.20 Enlarged XRD patterns near 27-29° (2 θ) for (1 1 2) main peak of (a) $\text{CaWO}_4:\text{Er}^{3+}/\text{Yb}^{3+}$, (b) $\text{CaMoO}_4:\text{Er}^{3+}/\text{Yb}^{3+}$, (c) $\text{SrWO}_4:\text{Er}^{3+}/\text{Yb}^{3+}$ and (d) $\text{SrMoO}_4:\text{Er}^{3+}/\text{Yb}^{3+}$ doped with different concentration of Li^+ ions	90
Figure 4.21 UC luminescence spectra of (a) $\text{CaWO}_4:\text{Er}^{3+}/\text{Yb}^{3+}$, (b) $\text{CaMoO}_4:\text{Er}^{3+}/\text{Yb}^{3+}$, (c) $\text{SrWO}_4:\text{Er}^{3+}/\text{Yb}^{3+}$ and (d) $\text{SrMoO}_4:\text{Er}^{3+}/\text{Yb}^{3+}$ doped with different concentration of Li^+ ions; the insert shows the enhancement factor of green UC emission as a function of the Li^+ concentration	93

Figure 4.22 Energy level diagrams of Er^{3+} and Yb^{3+} ion..... 96

Figure 4.23 Pump power dependence of the green and red UC luminescence of
(a) $\text{CaWO}_4:\text{Er}^{3+}/\text{Yb}^{3+}$, (b) $\text{CaMoO}_4:\text{Er}^{3+}/\text{Yb}^{3+}$, (c) $\text{SrWO}_4:\text{Er}^{3+}/\text{Yb}^{3+}$
and (d) $\text{SrMoO}_4:\text{Er}^{3+}/\text{Yb}^{3+}$ doped with 15 mol% of Li^+ ions..... 97

Figure 4.24 Dependence of lattice constant on the UC luminescence intensity of
(a) $\text{CaWO}_4:\text{Er}^{3+}/\text{Yb}^{3+}$, (b) $\text{CaMoO}_4:\text{Er}^{3+}/\text{Yb}^{3+}$, (c) $\text{SrWO}_4:\text{Er}^{3+}/\text{Yb}^{3+}$
and (d) $\text{SrMoO}_4:\text{Er}^{3+}/\text{Yb}^{3+}$ doped with different concentration of Li^+
ions 99



Synthesis and Upconversion Luminescence Properties of
Lanthanide Doped Oxide Phosphors

Hyeon Mi Noh

Department of Physics, The Graduate School
Pukyong National University

Abstract

Recently, upconversion (UC) phosphors have attracted much attention because of its broad range of applications, for example in light emitting diodes (LED), flat displays and solar energy converters. Large variety of luminescence materials have been investigated by doping and co-doping of lanthanide and non lanthanide ions to solid matrices. A variety of excellent low phonon frequency oxide host materials have been reported such as $Y_3Al_5O_{12}$, $YAlO_3$, ZrO_2 and Y_2O_3 . These host materials matches well with the lanthanide dopants in terms of its valency and ionic radius and thus, resulting in its high melting point and low cut-off phonon energy.

The present work deals with a detailed investigation on the UC luminescence from lanthanide doped and co-doped oxide phosphors. Various dopants of activator ions and sensitizer ion (Yb^{3+}) have been used in combination

with the oxide host for enhancement of UC luminescence resulting in a green, red (Er^{3+}) and yellow (Ho^{3+}) emissions. Additionally, the UC mechanisms of lanthanide doped oxide materials are analyzed using an energy level diagram and rate equation that includes the energy transfer processes. This thesis work follows a systematic studies and can be summarized as follows:

1. The UC luminescence properties of $\text{YAlO}_3:\text{Er}^{3+}$ nanophosphors are investigated. Initially, the samples are synthesized by a simple solvothermal reaction technique. The structural elucidation and crystallinity studies of the prepared samples are carried out using powder X-ray diffraction (XRD) while, its emission spectra was recorded at 975 nm diode laser. Their UC processes were explained by measuring the UC luminescence spectra and pump power dependence.

2. $\text{ZrO}_2:\text{Er}^{3+}$ and $\text{ZrO}_2:\text{Er}^{3+}, \text{Yb}^{3+}$ phosphors were synthesized *via* a simple solvothermal technique. At low concentrations of Yb^{3+} , the crystalline structure changed from tetragonal to monoclinic phase with the increase of sintering temperature. As the concentration of Yb^{3+} increased to a value above 0.05M, ZrO_2 phosphors displayed a very stable tetragonal phase.

3. The UC luminescence properties of $\text{ZrO}_2:\text{Ho}^{3+}$ and co-doped $\text{ZrO}_2:\text{Ho}^{3+}, \text{Yb}^{3+}$ nanophosphors with various concentrations of Yb^{3+} ions were synthesized *via* solvothermal technique. The prepared samples show a strong green, weak red and near infrared UC. The energy transfer processes between the Ho^{3+} and Yb^{3+} ions and the mechanisms involved have been investigated.

4. ABO_4 (A= Ca, Sr; B=W, Mo): $Er^{3+}/Yb^{3+}/Li^+$ phosphors tri-doped with different concentrations of Li^+ ion ranging from 0 to 22.5 mol% were prepared using a solid-state reaction method. Their UC luminescence properties were investigated under a 975 nm laser diode excitation. The four kinds of phosphors namely $CaWO_4$, $CaMoO_4$, $SrWO_4$, and $SrMoO_4$ showed a strong green UC emission peaks at 530, 550 nm and a weak red UC emission. A detailed investigation on the optimum doping concentration of Li^+ ions and the effects of Li^+ concentration on UC emission intensity were studied in detail.

The experimental results obtained from this thesis can be utilized for the synthesis of UC phosphors and for a variety of applications. To conclude, the lanthanide doped oxide UC phosphors can be strongly established as one of the promising candidates in the field of display and white lighting source for LEDs and for biomedical application.

I. Introduction

1.1 Description of phosphors

Generally, a phosphor is a substance that exhibits the phenomenon of luminescence. It includes both the phosphorescent and fluorescent materials, which is responsible for the slow decay in brightness (> 1 ms), and the emission decay time of over tens of nanoseconds, respectively. Phosphorescent materials are well known for their use in radar screens and glow-in-the-dark toys, while the fluorescent materials are found common in cathode ray tube (CRT) and plasma video display screens, sensors, and white LEDs.

Phosphors are generally made out of a suitable host material in combination with an activator. Few of the notable and known types are the copper-activated zinc sulfide and silver-activated zinc sulfide. The host materials used are typically oxides, nitrides and oxynitrides, sulfides, selenides, halides or silicates of zinc, cadmium, manganese, aluminium, silicon, or various rare earth metals. The activators play a vital role in prolonging the emission time (afterglow). But materials such as nickel are used to quench the afterglow and shorten the decay process of the phosphor emission characteristics.

The production of many phosphor powders involves low-temperature processes such as sol-gel where, they require post-annealing at temperatures of ~ 1000 °C, and it is undesirable for many applications. However, proper optimization of the growth process will eliminate the process of annealing [1].

Phosphors used in fluorescent lamps involve a multi-step production

process, with varied details based on the particular phosphor used. Bulk material must be milled sufficiently to obtain a desired range of particle size, as large particles leads to the production of poor quality lamp coating and the small particles results in the production of less light along with the quick degradation. At the stage of firing the phosphor, a well controlled process conditions must be followed to avoid oxidation of the phosphor activators or contamination from the process vessels. After milling, the phosphor has to be washed to remove the minor excess of activator elements. During the processing the volatile elements should not be allowed to flee. Usually, the lamp manufacturers have altered the composition of phosphors to eliminate few of the toxic elements, such as beryllium, cadmium, or thallium [2].

1.2 Upconversion phosphors

Since the discovery of Auzel [3,4], Ovsyankin and Feofilov [5] in the year 1960s, upconversion (UC) has been the focus of immense research, and especially for the conversion of infrared to visible light, taking advantageous of the cheap laser diode emitting around 975 nm developed in the 1980s. In the past five years, the number of publications has increased significantly in the field. The recent research is oriented towards the assessment of the potential of upconverting materials for photovoltaic or bio-imaging applications. Most of the UC researches were focused on the investigation of lanthanide doped halide [6-11] and oxide [12-15] host materials, sometimes in the form of glasses [16-19].

In the past ten years, upconversion lasing has been observed in a number of materials doped with trivalent rare-earth ions, notably praseodymium [20,21], neodymium [22,23], holmium [24], erbium [25-27] and thulium [28,29]. Upconversion is caused by multiple excitations by a direct pump or energy transfer or both. For instance, an excited ion absorbs a photon and reaches a higher excited level, and when it returns to the ground state the photon so emitted possess a higher energy than that of the absorbed photon.

1.3 Host and activator materials

1.3.1 Yttrium aluminium garnet ($\text{Y}_3\text{Al}_5\text{O}_{12}$) and yttrium aluminium perovskite (YAIO_3)

Yttrium aluminium garnet ($\text{Y}_3\text{Al}_5\text{O}_{12}$, YAG) belongs to the synthetic crystalline material of the garnet group. It is also one among the three phases of the yttria-aluminium composite, whereas the other two being the yttrium aluminium monoclinic (YAM) and yttrium aluminium perovskite (YAP). YAG is commonly encountered as a host material in various solid-state lasers. Rare earth elements such as neodymium and erbium can be doped into YAG as active laser ions, and thus yielding Nd:YAG and Er:YAG lasers, respectively. Cerium-doped YAG (YAG:Ce) is frequently used as a phosphor in the fabrication of cathode ray tubes and white light-emitting diodes, and also as a scintillator.

YAG is a well-known and widely accepted host for laser applications due to its associated low phonon energy ($550 - 600\text{cm}^{-1}$) that makes this nanophosphor

striking for photonic applications, and specifically for the UC processes [41]. High phonon energy of the host induces a fast relaxation of excited states and thus preventing its promotion to upper levels. Thus, it can be concluded that the use of low phonon energy glasses are vital for an efficient UC process. Many other hosts with lower phonon energy are reported in the literature, for the improvisation of the probability of UC. However, YAG nanopowder and YAG ceramic continues to be on top of the most favorable laser host among all other oxide ceramics. Several works have been reported based on the red and green upconverted signals in YAG:Yb³⁺, Er³⁺ nanocrystals. The emission dependence on dopant ion concentration, presence of direct energy transfer (ET) and energy back transfer (EBT) between donor (Yb³⁺) and acceptor (Er³⁺) ion in nanoparticles have already been reported [42,43].

Yttrium aluminium perovskite is a metastable form of the Y₂O₃-Al₂O₃ system, which is produced in addition to the stable oxide phases such as Al-rich cubic YAG, Y-rich monoclinic YAM and a metastable hexagonal phase (YAH) with the similar stoichiometry of YAP [44-47]. In the conventional method of material processing of YAP phase, the cubic and monoclinic forms are thermodynamically favored and are invariably present along with orthorhombic yttrium aluminium perovskites. Further, due to the high growth temperatures of YAP, it is difficult to get fine crystalline materials. Moreover, the crystals thus obtained will have several growth deformities, such as vacancy anti site defects and presence of impurities [48].

1.3.2 Zirconium oxide (ZrO₂)

In the recent times, the use of rare earth doped ZrO₂ is demonstrated as one among the good candidates for the development of visible emission nanophosphor, both by pumping with a UV [49,50] and by near infrared source [51-53]. ZrO₂ is a both chemically and thermally stable material that has a low phonon energy of about 470 cm⁻¹ [54]. This value is very low when compared, with that of other oxide hosts such as Y₃Al₅O₁₂ (850 cm⁻¹) or Y₂O₃ (597 cm⁻¹) [55]. This low phonon energy opens up the venue for the trapping of more efficient luminescence of active ions incorporated into the host [56-58]. It also proves its superiority in terms of its hardness, high refractive index, optical transparency, photothermal stability, and high thermomechanical resistance. Thus, ZrO₂ can be utilized for a variety of photonics and industrial applications. In the last couple of years, we have been studying the luminescence, both in terms of down and upconversion, using rare earth doped ZrO₂ nanocrystal to improve the efficiency of visible emission by optimizing the active ion concentration and appropriate sensitizer, taking advantage of its nanosize effect. The strong green and red upconversion emission of ZrO₂:Er³⁺ nanophosphor was investigated as a function of ion concentration and pumping wavelength [59]. Additionally, the strong green emission of ZrO₂:Yb³⁺-Ho³⁺ and the blue-green emission of ZrO₂:Yb³⁺ was investigated as a function of Yb³⁺ ion [60].

1.3.3 ABO₄ (A=Ca, Sr; B=W, Mo) compounds

The alkaline-earth metal tungstates AWO₄ (A=Ca²⁺, Sr²⁺, Ba²⁺) have been extensively investigated as a self-activating phosphor emitting blue or green light under ultraviolet or X-ray excitation [61,62]. The full-width half-maximum (FWHM) of the blue emission is relatively broad in AWO₄ phosphor (about 100 nm) [61], which is quite disadvantageous in the improvisation of color purity. At present, AWO₄ were reported to be efficient luminescent hosts for rare earth [63-65]. Most of molybdates and tungstates are important luminescence materials with scheelite-type tetragonal structure, belonging to I4₁/a space group with two formula units per primitive cell. In the ABO₄ (A= Ca, Sr; B=W, Mo) compounds, each of B atoms is surrounded by four equivalent O atoms composing the [BO₄]²⁻ tetrahedron configuration and each divalent metal shares its corners with eight adjacent O atoms of [BO₄]²⁻ tetrahedrons [66,67].

The W⁶⁺ and Mo⁶⁺ ions in ABO₄ matrices have a strong polarization because of their large electric charge and small radius; this strong polarization consequently decreases symmetries and enhances the Stark energy splitting of the RE ion in the crystal field [68]. More efforts are put forth towards the improvement of optical properties of molybdate phosphors. Detailed investigations were carried out elucidating the effect of surfactants on morphology and luminescence properties [68], and the effect of the alkali metal compensation on the optical properties [69].

1.3.4 Properties of Er³⁺, Ho³⁺, Yb³⁺ ions

Many lanthanide ions such as Er³⁺, Tm³⁺ and Ho³⁺ have been used as luminescent centers because of the presence of sufficient electronic energy levels for UC luminescence, and a few of them are suitable for direct pumping by near infrared (NIR ~ 980 nm) laser diode [70,71]. Among the suitable candidates for upconversion materials, trivalent erbium Er³⁺ has shown excellent upconversion properties [72,73]. In the NIR region, Er³⁺ has a favorable energy-level structure with two transitions namely (⁴I_{15/2} - ⁴I_{11/2}) and (⁴I_{15/2} - ⁴I_{9/2}), observed at 967 and 800 nm, respectively, which can be excited with semiconductor lasers, yielding blue, green and red emissions. Due to its enriched energy level structure, trivalent erbium ions hosted in fluoride and oxide crystal matrices serve as excellent optical activator that permits the possibility of simultaneous emission in ultraviolet, visible and infrared wavelength range [74-76]. The luminous properties are highly dependent on the excitation energy, concentration of the dopant, and nature of the host crystal. The various emissions thus obtained can be excited with photons of lower energies taking advantage of the ESA and ETU processes. Among the several states of the 4f¹¹ electronic configuration of Er³⁺, a number of pairs show levels whose energy separation matches well with that of another pair of states in a resonant or quasi-resonant condition, and thus allowing for the onset of variety of ETU processes typical to this system. The chances of fulfilling the resonance condition are greatly enhanced by the crystal-field splitting at each level into Stark components whose, position in energy is highly dependent on the host. Furthermore, electron-phonon coupling can bridge

gaps of several hundreds of cm^{-1} , giving rise to phonon-assisted transfer of energy among Er^{3+} ions. The Er^{3+} ion has a relatively low absorption cross-section for the transitions in the near-infrared NIR region, while the Yb^{3+} ion exhibits a higher absorption cross-section. Thus, co-doping with Er^{3+} and Yb^{3+} has proven to be a successful alternative for enhanced upconversion processes. In fact, there is a large spectral overlap between the Yb^{3+} (${}^2\text{F}_{5/2} - {}^2\text{F}_{7/2}$) NIR emission and the Er^{3+} (${}^4\text{I}_{15/2} - {}^4\text{I}_{11/2}$) absorption bands, which results in efficient non-radiative energy transfer processes [77].

The trivalent holmium (Ho^{3+}) appears to be an important candidate for UC due to its favorable energy level scheme. Especially, with the advent of cheaply available and powerful IR laser diodes (LD), there was an upcoming interest for $\text{Ho}^{3+}/\text{Yb}^{3+}$ UC, taking advantage of $\text{Yb}^{3+} - \text{Ho}^{3+}$ energy transfer (ET) [78,79].

1.4 Purpose and outline

The present work has been performed with the objective of investigating the synthesis conditions and UC processes that influence the UC mechanisms. The significance and aims of the study are listed as follows:

1. Lanthanide doped and co-doped oxide phosphors are synthesized by planetary ball mill and solvothermal reaction method and their properties of UC luminescence properties are investigated.
2. Various UC processes were understood and the mechanisms of energy transfer have been investigated.
3. Various UC mechanisms were investigated by pump power dependence

and energy level diagram and the results obtained are confirmed by theoretical investigations based on steady-state rate equations.



II. Upconversion processes

2.1 Conversion of low-energy incident radiation into higher-energy emitted radiation

There are several well known processes that can convert low-energy incident radiation into higher-energy emitted light. The most relevant processes for such light conversion are summarized in Fig. 2.1 [30,31]. In Fig. 2.1, there are non-linear two-photon processes, where two incident photons are converted into one emitted photon of significantly higher energy. The typical emitted power P_{em} densities vary quadratically with the incident power density P_{inc} , with a proportionality coefficient of $P_{em} = uP_{inc}^2$. A comparison of the energy conversion efficiencies of the different processes are depicted in Fig. 2.1. With its high-energy conversion efficiencies and low excitation power thresholds, UC is particularly relevant for future applications.

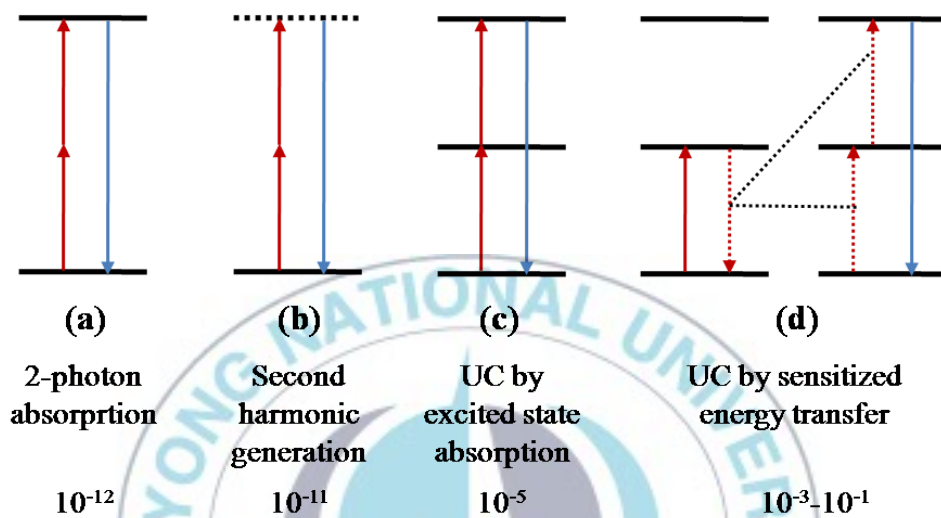


Figure 2.1 Various processes involved in the conversion of low-energy incident radiation into higher-energy emitted radiation and their typical values are associated with them [30,31].

2.2 UC mechanisms

There are two different types of UC: the single-ion excited-state absorption process and the two-ion (sensitized) energy transfer upconversion process. In both the types of UC, the phosphor has to subsequently absorb two excitation photons, followed by the emission of a photon of higher energy. It does not imply that the ion only absorbs two excitation photons before any emission of a photon, as often there is an intermediate nonradiative relaxation step between the absorption of the two excitation photons and the emission.

For the complete understanding of UC mechanisms, four main processes are schematically depicted in Fig. 2.2. The first and second processes, as indicated in Fig. 2.2 (a) and (b), shows as what happens when the material is excited from its ground state or from an excited state, respectively. Considering the case of two ions where both are in an excited state, energy transfer upconversion can take place, as is shown in Fig. 2.2(c). As a result of this process, one ion is de-excited to a lower-energy state (though not necessarily the ground state), while the second is excited to a higher-energy state. The fourth process namely cross-relaxation, is the reverse of energy transfer upconversion where, one ion is excited to a higher-energy state, and the second is de-excited to a lower-energy state. This process is clearly shown in Fig. 2.2(d). The distinction between these last two processes lies in the highest excited state: suppose, after the process has taken place, one of the ions is in a higher excited state than either of the ions prior the process, one details the energy transfer upconversion. If this is not the case, it relies on cross-relaxation. In some materials, several of the UC

mechanisms listed in this part contribute to the UC luminescence emission.

2.2.1 Excited State Absorption (ESA)

Excited state absorption (ESA) is a process that involves the absorption of a photon from a lower excited state to a higher excited state of an atom, molecule or ion. ESA can occur only after an electron has already been excited to the lower excited state. The lower excited state has a higher energy when compared to the ground state level and the higher excited state is higher in energy than the lower excited state. ESA from the first excited state is illustrated in Fig. 2.3(a).

Fig. 2.3(a) shows as what happens to a material when it is excited from its ground state or from an excited state (GSA/ESA). It only involves single dopant typically a trivalent lanthanide ion. The first excitation photon is absorbed by the ground level and populates the intermediate state (1^{st}). The lifetime of this state is long enough, and therefore a second incident photon can be absorbed, further exciting ion from its intermediate state into a higher excited state (2^{nd}), from which UC luminescence originates. In the case of ESA, a simple single exponential decay is measured as shown in Fig. 2.3(b).

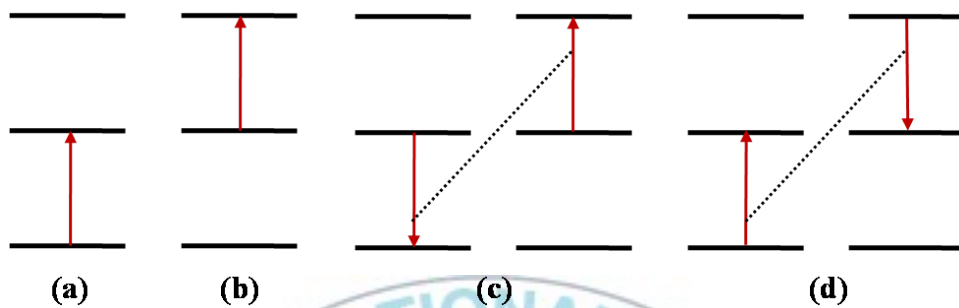
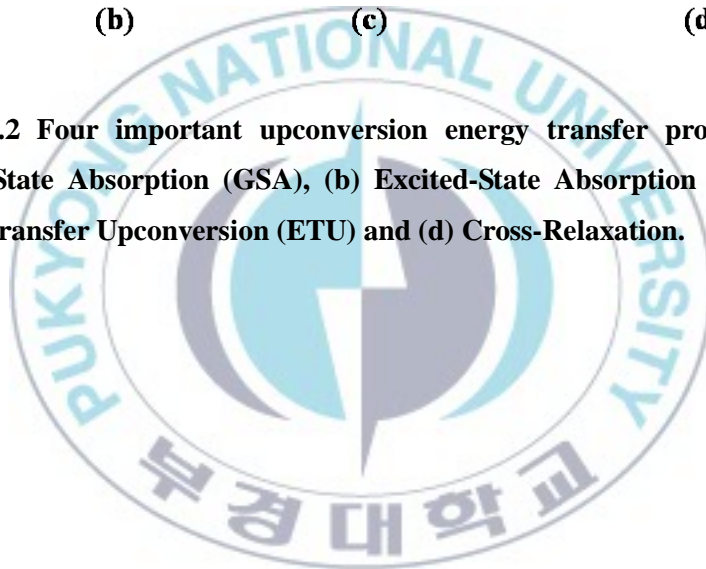


Figure 2.2 Four important upconversion energy transfer processes. (a) Ground-State Absorption (GSA), (b) Excited-State Absorption (ESA), (c) Energy Transfer Upconversion (ETU) and (d) Cross-Relaxation.



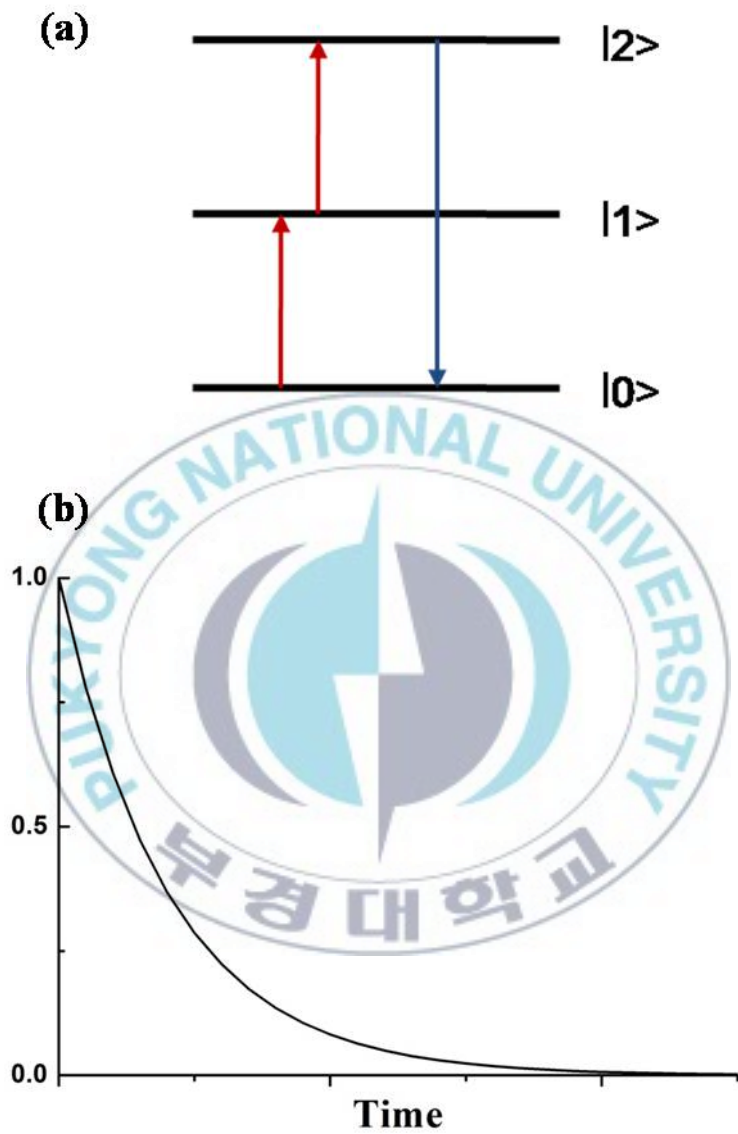


Figure 2.3 (a) Schematic representation of ESA process and (b) the characteristic time response curve of the up converted emission.

2.2.2 Energy Transfer Upconversion (ETU)

Considering the case of two ions where both the ions are in an excited state, energy transfer upconversion takes place as shown in Fig. 2.4(a). As a result of this process, one ion is de-excited to a lower energy state (though not necessarily the ground state), while the second is excited to a higher-energy state. It involves non-radiative energy transfer between both the dopants; a sensitizer and an activator. The sensitizer usually has a strong absorption cross-section at the excitation wavelength. When ETU is responsible for the upconversion excitation the initial intensity was observed to be zero, followed by an increase in the emission intensity and with a further increase in time a subsequent exponential decrease was observed. This behavior is graphically shown in Fig. 2.4(b).

These energy transfer processes generally involves electric dipole-dipole interactions. The typical efficiency value, η for UC by sensitizer ETU is generally in the order of $10^{-3} \text{ cm}^2/\text{W}$ (two orders of magnitude higher than the value associated with GSA/ESA) [32].

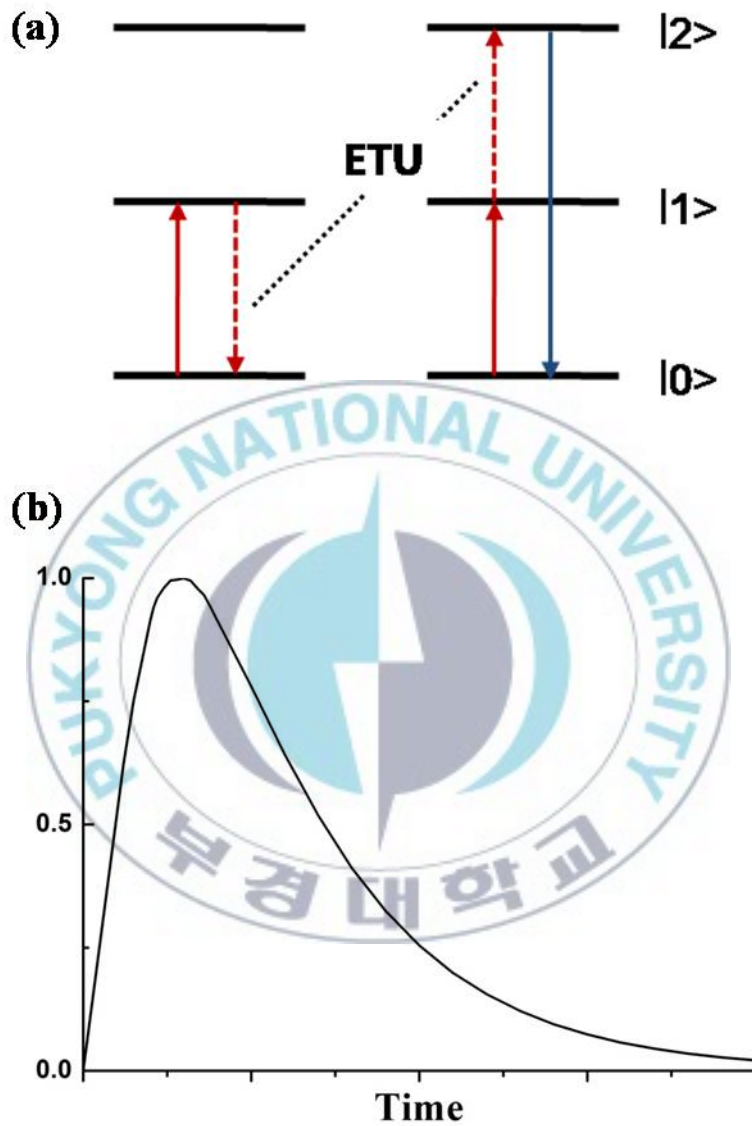


Figure 2.4 (a) Schematic representation of ETU process and (b) the characteristic time response curve of the up converted emission.

2.2.3 Cooperative luminescence

Fig. 2.5 depicts the cooperative luminescence process. It involves the sequential absorption of two excitation photons by two different active ions, and thus bringing both of them into their excited states. Later both the excited ions are simultaneously decayed to their ground states with an emission of a single photon that imbibed the combined energy of both ions. As the cooperative emission occurs from a virtual state, the emission probability is rather low. Also, since only one of the two excited ions needs to decay to its ground state to prohibit cooperative emission, the lifetime of the cooperative emission is given by exactly half of the lifetime of the excited state of the single ion when they are in the same excited states. It is also notable that the two absorbing ions need not be of the same species, or be in the same excited states, although this is often the case. Considering the case where, two of the ions are in excited states with lifetimes of τ_1 and τ_2 , then their cooperative luminescence will have a lifetime which is given by

$$\tau_{\text{Coop}} = ((\tau_1)^{-1} + (\tau_2)^{-1})^{-1} \quad (1.1)$$

A well-known example is $\text{YbPO}_4:\text{Yb}^{3+}$, where it shows cooperative luminescence with an efficiency of $\sim 10^{-8} \text{ cm}^2\text{W}^{-1}$ [5]. Two excited Yb^{3+} ions generate one photon with dual energy, in the green region of the spectrum.

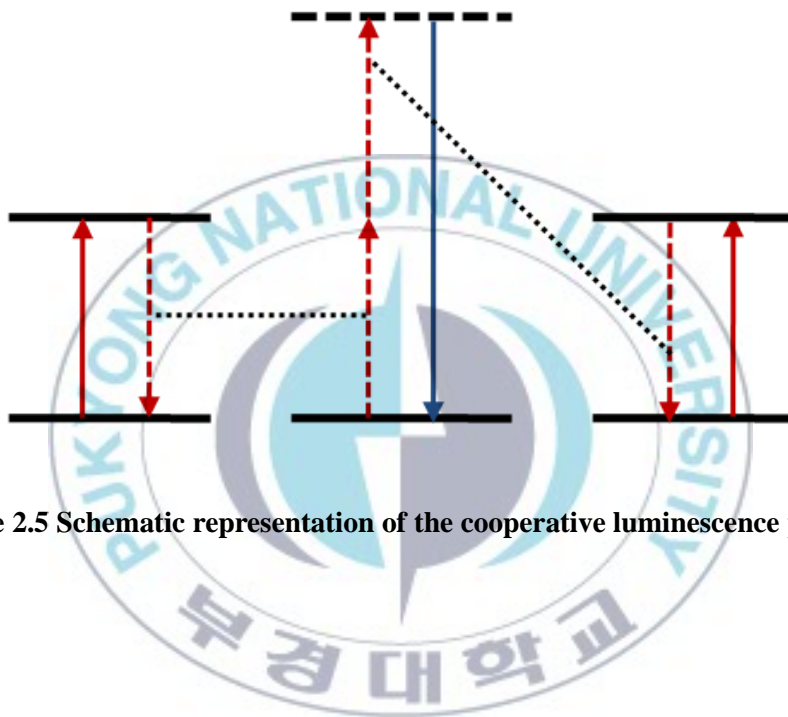


Figure 2.5 Schematic representation of the cooperative luminescence process.

2.2.4 Cooperative sensitization

The cooperative sensitization (Fig. 2.5) is similar to that of the cooperative luminescence. In this process, two excitation photons are sequentially absorbed by two different active ions, and thus bringing both of them into their excited states. Now the energy of the two excited ions is gently transferred to another ion, thus transferring it from its ground state into an excited state at energy resonant with the sum of the two excitation energies. As the final state is real, in contrast to the case of cooperative luminescence, the cooperative sensitization is more efficient than cooperative luminescence. In the same lines, the two ions absorbing the initial radiation need not be of the same species or in the same excited states. $\text{YF}_3:\text{Yb}^{3+}, \text{Tb}^{3+}$ shows cooperative sensitization of Tb^{3+} from the Yb^{3+} ions with an efficiency of $\sim 10^{-6} \text{ cm}^2\text{W}^{-1}$ [32]. Here the two excited Yb^{3+} ions simultaneously transfer their energy to Tb^{3+} , bringing it into an excited state at $\sim 20,000 \text{ cm}^{-1}$.

2.2.5 Photon avalanche in UC

The fundamental avalanche UC model (the three level models [33]) relies on an excited state absorption in resonance with the pumped wavelength, from a level which is populated by one cross-relaxation step. The following scheme gives an introduction to the basis of theory involved [33] which depicts the requisite and suffice condition to observe an avalanche.

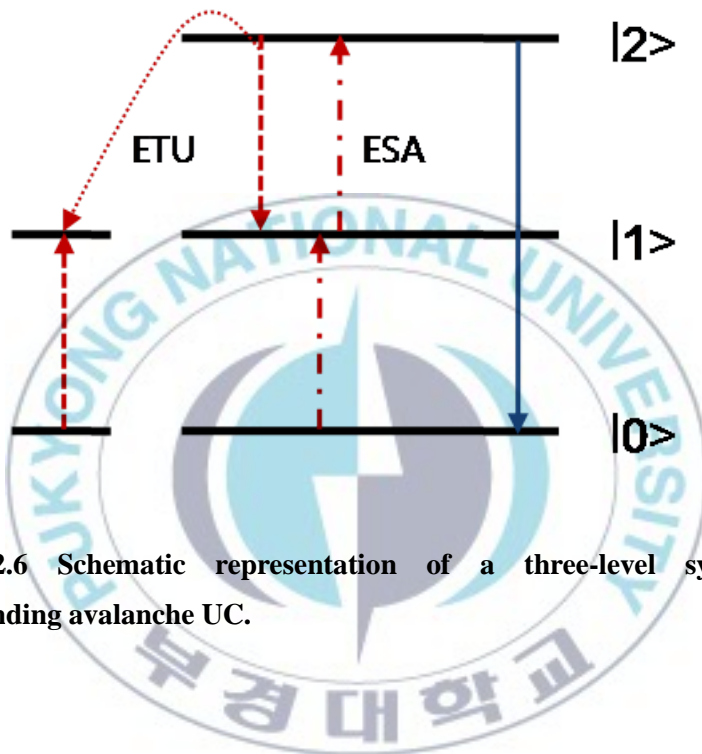


Figure 2.6 Schematic representation of a three-level system for understanding avalanche UC.

Fig. 2.6 shows a schematic representation of the three-level system that demonstrates the avalanche upconversion. For this effect to be observed it should fulfill three special conditions.

The photon avalanche process starts with population of level $|1\rangle$ by non-resonant weak GSA, followed by resonant ESA to populate upper visible-emitting level $|2\rangle$. After the metastable level population is established, cross-relaxation energy transfer (or ion pair relaxation) occurs between the excited ion and a neighboring ground state ion, resulting in both ions occupying the intermediate level $|1\rangle$. The two ions readily populate level $|2\rangle$ for further initiation of the cross-relaxation and exponential increase level $|2\rangle$ population by ESA, producing strong UC emission as an avalanche process.

2.3 Rate equations relevant to UC process

2.3.1 Rate equations in a three-level system

The rate equations for UC processes are usually non-trivial because, they involve many different energy states associated with the dopants incorporated in the host lattice. These dopants can be of different species, in which they have different energy levels. When framing the rate equations governing UC, various processes must be taken into consideration, which includes pump-induced transitions, radiative and non-radiative decays, energy transfers and cross-relaxations between dopants. In terms of modeling near-infrared (980 nm excitation) to green UC processes in Er^{3+} singly-doped materials, a simplified

three-level system is assumed. The three-levels considered are ${}^4I_{15/2}$ (ground state), ${}^4I_{13/2}$ (intermediate state) and ${}^4S_{3/2}$ (green UC emitting state) of Er^{3+} . It is assumed that all the Er^{3+} excited states located between ${}^4I_{11/2}$ and ${}^4S_{3/2}$ of Er^{3+} have very short lifetimes, implying that the electrons in these states decay rather quickly and non-radiatively to ${}^4I_{11/2}$ state of Er^{3+} . The schematic representations of UC processes in a three-level system are shown in Fig. 2.7.

In the Fig. 2.7, the two equations governing UC in three-level systems are:

$$\frac{dN_2}{dt} = R_1 N_1 + W N_1^2 - A_2 N_2 \quad (1.2)$$

$$\frac{dN_1}{dt} = R_0 N_0 - R_1 N_1 - 2W N_1^2 - A_1 N_1 \quad (1.3)$$

In this equation, R_0 is the absorption coefficient of ground state at an excitation of 975 nm, R_1 is the absorption coefficient of excited state, P is the incident pump power, W is energy transfer rate and A_i is the spontaneous emission rate. It was theoretically reported by Pollnau *et al.*, that if the population of the intermediate state is reduced through the UC process rather than direct decay to the ground state, the UC luminescence intensity has a linear dependence on excited pump power of P [34]. By solving this equation, one can easily determine the dependence of the power emitted by UC on the P in extreme cases, such as those described below.

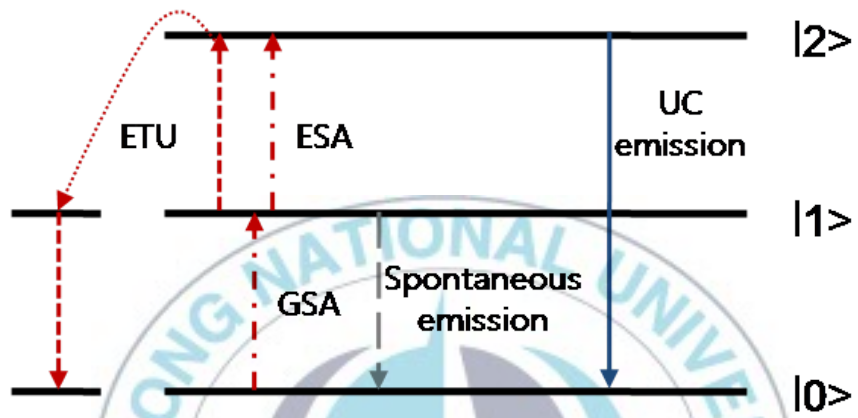


Figure 2.7 Schematic representations of UC processes in a three-level system.

2.3.2 Pump power dependence in ESA is dominant over ETU

Considering the case in which ESA is dominant over ETU, spontaneous emission rate should be larger than the UC rate, and so WN_l^2 can be neglected.

The rate equations can therefore be simplified as follows:

$$\frac{dN_2}{dt} = R_1N_1 - A_2N_2 \quad (1.4)$$

$$\frac{dN_1}{dt} = R_0N_0 - R_1N_1 - A_1N_1 \quad (1.5)$$

In the case, when the UC rate (by ESA) is high as compared to the spontaneous relaxation rate (i.e., $R_1N_1 \ll A_1N_1$), then one obtains: $N_2 \propto P$. On the contrary, if the spontaneous relaxation rate is dominated (i.e., $A_1N_1 \ll R_1N_1$), then $N_2 \propto P^2$.

Since the power of the UC emission is proportional to the population density N_2 of the UC emitting state, these results show that with increasing pump power, the dependence of the UC emission power on the excitation power changes from quadratic to linear. These results can be generalized to an $(n+1)$ energy level system in which n photons are involved. In that case, the UC luminescence originates from n 's state relaxation. The dependence of the UC emitted power on the pump power varies between $P_{uc} \propto P$ and $P_{uc} \propto P^2$.

2.3.3 Pump power dependence in ETU is dominant over ESA

In the particular case in which ETU is dominant over ESA, the UC rate should be larger than spontaneous emission rate, and therefore R_1N_1 can be neglected. The rate equations can therefore be simplified as follows:

$$\frac{dN_2}{dt} = WN_1^2 - A_2N_2 \quad (1.2)$$

$$\frac{dN_1}{dt} = R_0N_0 - 2WN_1^2 - A_1N_1 \quad (1.3)$$

In this case, if the UC (by ETU) rate is high when, compared to the spontaneous relaxation rate (i.e. $A_1N_1 \ll 2WN_1^2$), then $N_2 \propto P$. On the contrary, if the spontaneous relaxation rate dominates (i.e., $2WN_1^2 \ll A_1N_1$), then $N_2 \propto P^2$, which means that the population density of the UC emitting state is quadratic with an excitation pump power.

2.4 Center Luminescence

In the case of center luminescence, the emission is generated on an optical center, in contradiction to, e.g., emission, which results from optical transitions between host lattice band states or from a transition between two centers. Such an optical center can be an ion or a molecular ion complex. One speaks of characteristic luminescence when, in principle, the emission could also occur on the ion in a vacuum, i.e. when the optical transition involves electronic states of

the ion only. Characteristic luminescence possess a relatively sharp emission bands (spectral width of few nm, typically), but also of broad bands, which can have widths exceeding 50 nm in the visible part of the spectrum. Broad emission bands are observed when the nature of the chemical bonding in the ground and excited state differs considerably. This occurs simultaneously with a change in equilibrium distance between the emitting ion and its immediate chemical environment and is better explained with the configuration co-ordinate diagram (Fig. 2.8).

In this diagram, Q_g and Q_e represent the metal-ligand distances in the ground and excited states, respectively. E_a and E_e are the energies at which the absorption and emission bands have their maximum intensity, respectively. Δ is the energy of the zero phonon line; this transition involves completely relaxed excited and ground states, and no excited phonon states are involved – hence the name of this kind of transitions. The phonon frequencies of the ground and excited state are given as $\hbar\omega_g$ and $\hbar\omega_e$, respectively. The relaxation energies of the ground and excited states can be expressed as a product of the phonon energy and the so-called Huang-Rhys factors. The Huang-Rhys factors can be represented as S_e and S_g in the ground and excited state (being pure numbers), respectively, and it gives the mean value of phonons involved in the absorption and emission processes, respectively. In the harmonic approximation, the curvature of the parabolic band (determined by the bond strength), the phonon frequencies, and the Huang-Rhys factors are the same in the ground and excited state.

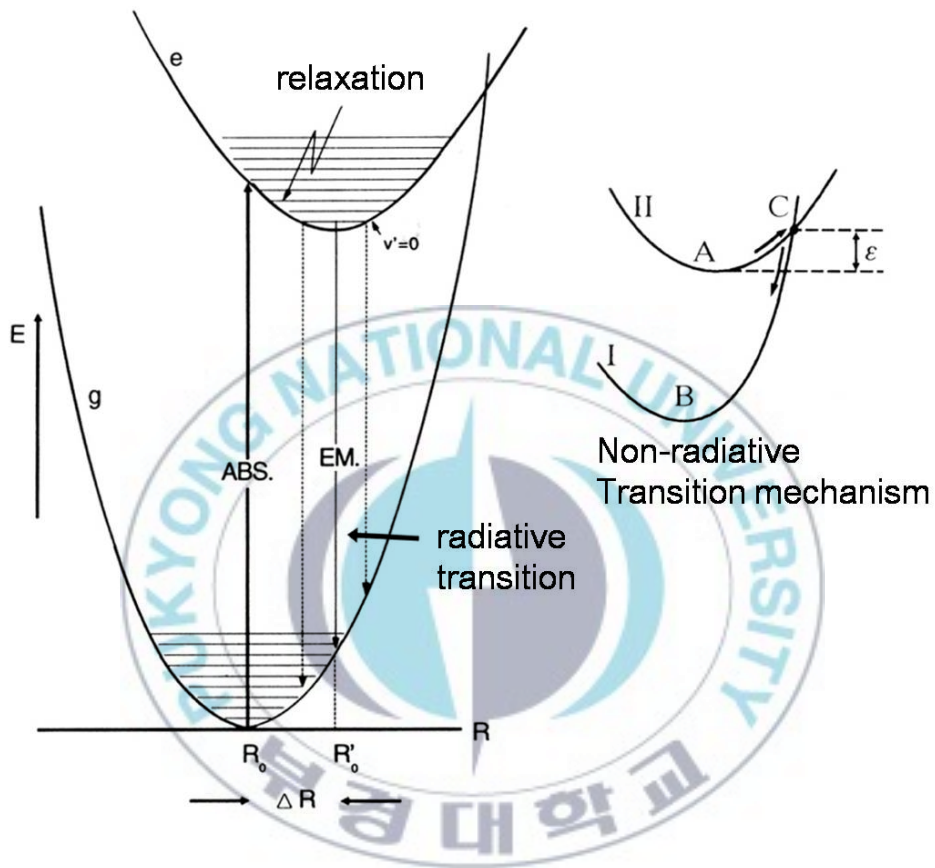


Figure 2.8 Schematic representation of the configurational coordination diagram.

2.5 Rare earth upconverter

Lanthanides (Ln) are a group of elements that can be found at the lower end of the periodic table. The 4f inner shells of lanthanides are partially filled with electrons. They are mostly stable in the trivalent state, and the Ln^{3+} ions have the electronic configuration of $4f^n 5s^2 5p^6$, where n varies between 0 and 14. The partially filled 4f inner shell is responsible for the characteristic optical and magnetic properties of the lanthanides. The number of configurations for n electrons divided over the 14 4f orbitals is large ($14/n$), and all of the configurations can have different energies.

Table 2.1 gives a summary of the basic properties of the trivalent rare earths, which includes the electronic configuration, the ground state and their corresponding ionic radius R. The characteristic energy levels of trivalent lanthanide ions are illustrated in Fig. 2.9. This energy level diagram was obtained experimentally by measuring the optical spectra of lanthanide ions by Dieke (1968) and Carnall *et al.* (1989), and this is also known as a *Dieke diagram*.

Most of the well-known upconverting phosphors contain trivalent rare earth ions as active components such as Pr^{3+} , Nd^{3+} , Er^{3+} , Tm^{3+} or Yb^{3+} , and there exists a possibility for the occurrence of other ions too. The reason for the vast majority of works reported in this field using the relatively small collection of ions can be attributed to the fact that these ions have their inner 4f (or 5f in the case of uranium) shell that contains the spectroscopically relevant electronic states.

Table 2.1 Tabulation of the basic properties of the trivalent rare earth elements [35,36].

Name of the Ion	Electronic Configuration	Ground state	R (Å)
La ³⁺	4f ⁰ 5s ² 5p ⁶	¹ S ₀	1.15
Ce ³⁺	4f ¹ 5s ² 5p ⁶	² F _{5/2}	1.02
Pr ³⁺	4f ² 5s ² 5p ⁶	³ H ₄	1.00
Nd ³⁺	4f ³ 5s ² 5p ⁶	⁴ I _{9/2}	0.99
Pm ³⁺	4f ⁴ 5s ² 5p ⁶	⁵ I ₄	0.98
Sm ³⁺	4f ⁵ 5s ² 5p ⁶	⁶ H _{5/2}	0.97
Eu ³⁺	4f ⁶ 5s ² 5p ⁶	⁷ F ₀	0.97
Gd ³⁺	4f ⁷ 5s ² 5p ⁶	⁸ S _{7/2}	0.97
Tb ³⁺	4f ⁸ 5s ² 5p ⁶	⁷ F ₆	1.00
Dy ³⁺	4f ⁹ 5s ² 5p ⁶	⁶ H _{15/2}	0.99
Ho ³⁺	4f ¹⁰ 5s ² 5p ⁶	⁵ I ₈	0.97
Er ³⁺	4f ¹¹ 5s ² 5p ⁶	⁴ I _{15/2}	0.96
Tm ³⁺	4f ¹² 5s ² 5p ⁶	³ H ₆	0.95
Yb ³⁺	4f ¹³ 5s ² 5p ⁶	² F _{7/2}	0.94
Lu ³⁺	4f ¹⁴ 5s ² 5p ⁶	¹ S ₀	0.93

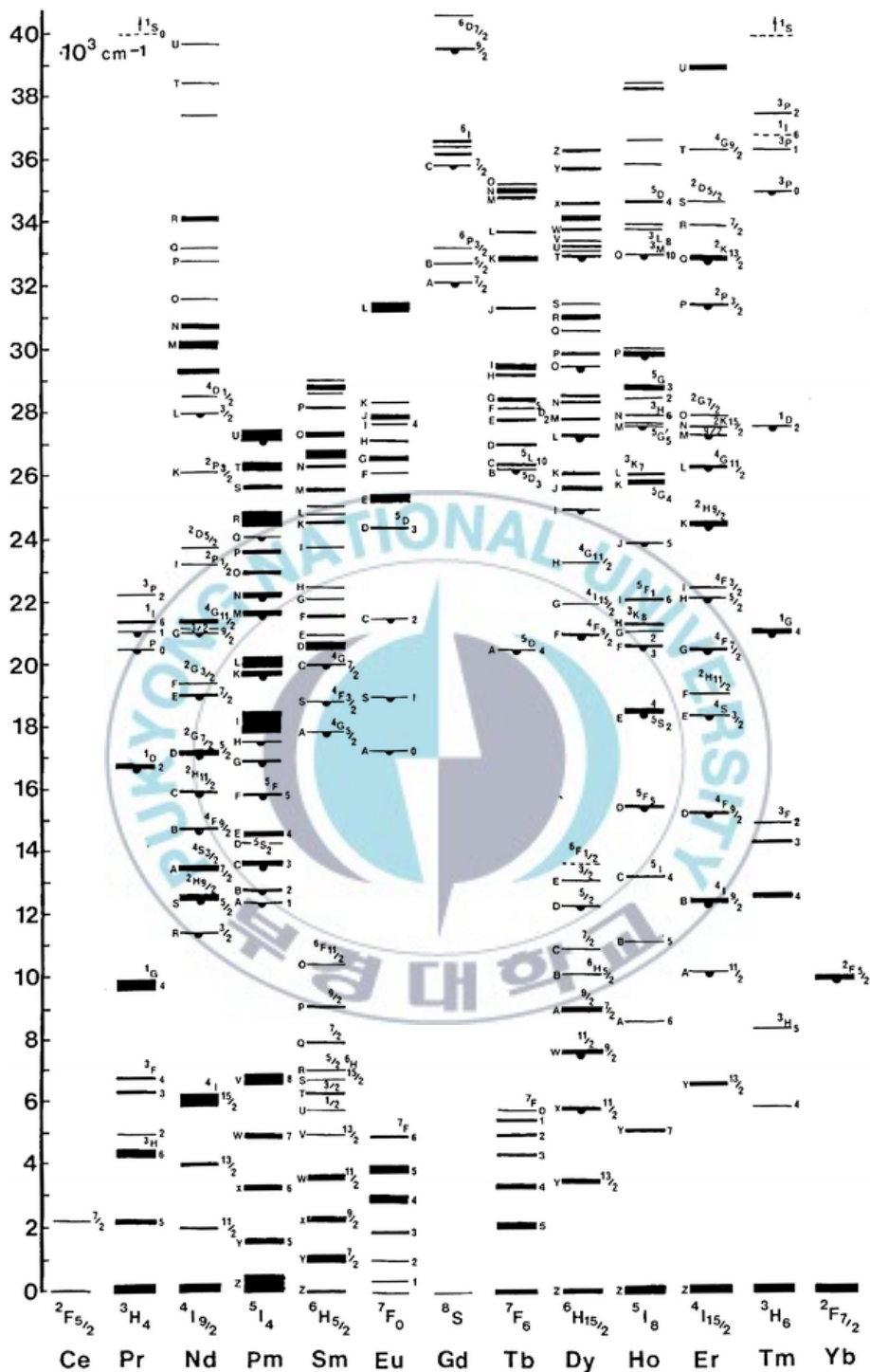


Figure 2.9 Illustration of the *Dieke diagram*: Energy levels of lanthanide ions [37].

As the outer 5s and 6p (6s and 6p for uranium) shells are involved in the bonding, the f states are rather insensitive to the precise nature of the surrounding host lattice (i.e. the exact crystal field and, to a lesser extent, the local site symmetry). As a result, a significant number of the excited f states have lifetimes that are longer to allow for UC processes to take place. UC was first observed in the rare earth ions, and are discovered by Auzel [4] and independently by Ovsyankin and Feofilov [6] in the mid-1960s.

Fig. 2.10 shows the near-infrared and visible part of the energy level structure of trivalent erbium, ytterbium, and thulium. These are few of the widely used ions in UC phosphors. Typically, one can distinguish three main types of (bulk) host materials that are used in the application of UC phosphors as single crystals, optical fibers, and glasses, respectively.

When the excitation energies are limited to the often used $\sim 10,000 \text{ cm}^{-1}$, it is discernible that only the ${}^2F_{5/2}$ (Yb^{3+}) and ${}^4I_{11/2}$ (Er^{3+}) states are at such energies that direct excitation into these states is possible. Given that the excitation cross-section for Yb^{3+} (${}^2F_{7/2} \rightarrow {}^2F_{5/2}$) that contains the full f-f oscillator strength, while the Er^{3+} (${}^4I_{15/2} \rightarrow {}^4I_{11/2}$) transition contains only a part of the oscillator strength, a reasonable estimate is that (at room temperature) the majority of the excitation photons will be absorbed by Yb^{3+} . As Yb^{3+} has no higher excited states than the ${}^2F_{5/2}$, this ion must perform energy transfer upconversion with another species (e.g. Er^{3+} or Tm^{3+}) for the occurrence of visible emission. Within the energy range shown in Fig. 2.10, Yb^{3+} has several energy transfer possibilities to both the ions, as indicated by the dotted arrows. When no strong multi-phonon

relaxation is considered, there are three energy transfer possibilities from Yb^{3+} to Er^{3+} (to induce the Er^{3+} transitions ${}^4\text{I}_{15/2} \rightarrow {}^4\text{I}_{11/2}$, ${}^4\text{I}_{11/2} \rightarrow {}^4\text{F}_{7/2}$, and ${}^4\text{F}_{9/2} \rightarrow {}^4\text{G}_{11/2}$, respectively) and four to Tm^{3+} (to induce the transitions ${}^3\text{H}_6 \rightarrow {}^3\text{H}_5$, ${}^3\text{F}_4 \rightarrow {}^3\text{F}_2$, ${}^3\text{H}_4 \rightarrow {}^1\text{G}_4$, and ${}^1\text{G}_1 \rightarrow {}^1\text{D}_2$, respectively). However, on inclusion of multiphonon relaxation (or strong cross-relaxation) a fourth energy transfer path to Er^{3+} is opened up: after, e.g., the nonradiative transition ${}^4\text{I}_{11/2} \rightarrow {}^4\text{I}_{13/2}$, the Er^{3+} transition ${}^4\text{I}_{13/2} \rightarrow {}^4\text{F}_{9/2}$ becomes possible via energy transfer upconversion. This is significant, since it implies that there are now two distinctly different Er^{3+} states (the ${}^4\text{F}_{9/2}$ and ${}^4\text{S}_{3/2}$) that are both populated *via* a 2-photon energy transfer upconversion process. However, as the rate constants for these two processes are not the same (partly because of the additional relaxation step required for reaching the ${}^4\text{F}_{9/2}$), the excitation powers required for reaching the high-power limit will not generally be identical for these two states. In the low-power limit the emission intensity of a state excited *via* a two-photon process will scale up with the laser power squared, while in the high-power limit it will be in linear with the laser power. As a result, in the intermediate-power regime, the populations of the ${}^4\text{F}_{9/2}$ and ${}^4\text{S}_{3/2}$ states will have different power dependence. This implies, in this region, the red to green emission ratio of any upconversion phosphor that has a ${}^4\text{I}_{13/2} \rightarrow {}^4\text{F}_{9/2}$ excitation pathway will depend on the excitation power. Clearly this widens up the possibilities, because in this way one can tune the emission color of an upconversion phosphor simply by varying the excitation power.

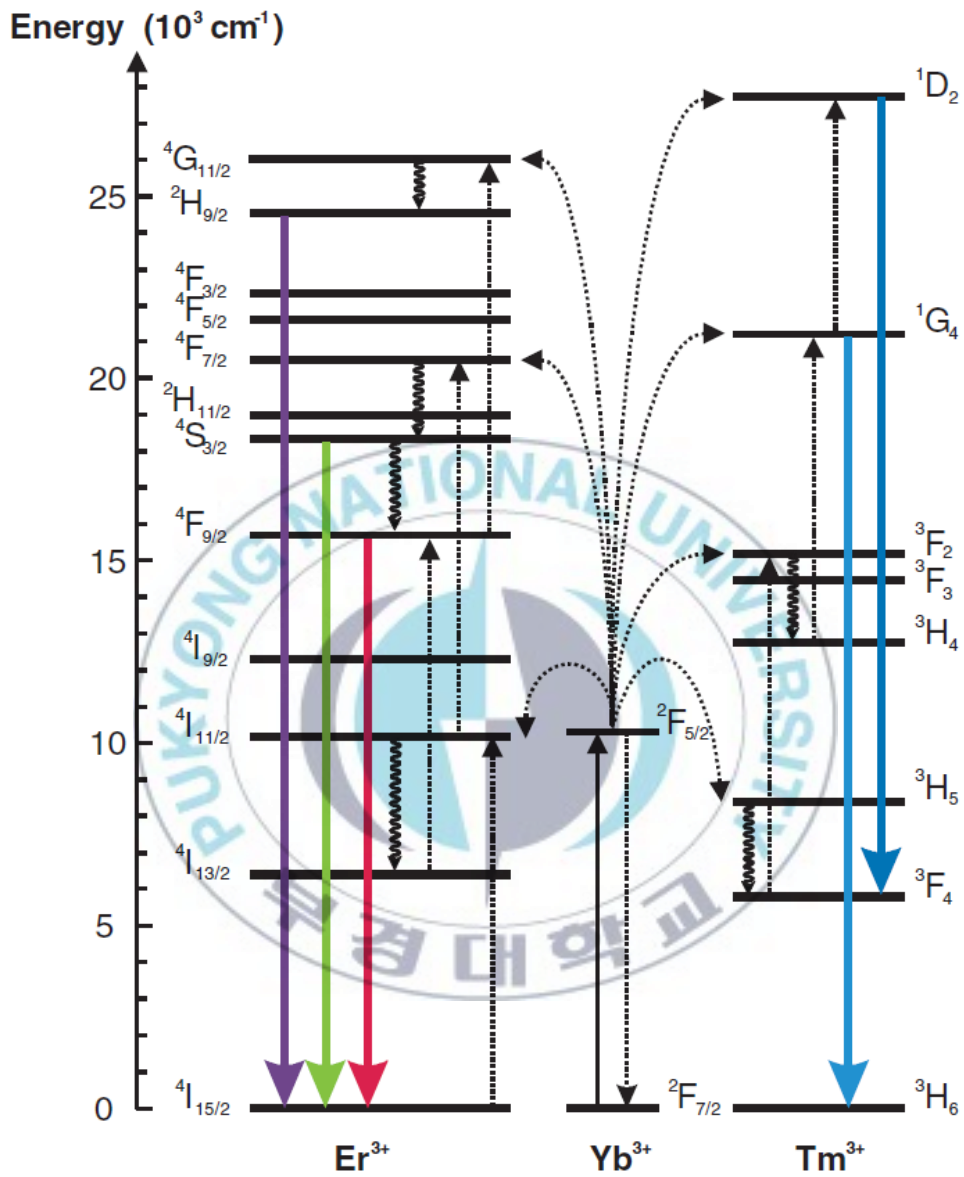


Figure 2.10 Illustration of the energy level diagrams of Yb^{3+} , Er^{3+} and Tm^{3+} .

2.6 Applications of UC

At present, there exists an immense interest in luminescent materials for efficient frequency conversion from infrared to visible radiation, mainly because a visible source pumped by a near infrared laser is useful for high-capacity data storage optical devices. These applications of UC materials are indicated in Fig. 2.11. This process can be obtained by UC mechanisms, where several infrared photons can be absorbed by the material doped with rare earth ions (RE) in order to populate more energy levels. Therefore, both the fluorescence lifetime and the stimulated emission cross-section of the RE excited level should be maximized, whereas the nonradiative decay mechanisms should be minimized. Oxyfluoride glass ceramics are ambivalent materials. Despite the fact that, they are mainly oxide glasses, they can exhibit optical properties of fluoride single crystals when they are doped with rare earth ions. They are often called nanocomposite materials. Their peculiar character is obtained by a classical melting and quenching preparation in air followed by an adapted thermal treatment during which fluoride phases are crystallized. The crystallite size, size distribution, and volume concentration of fluoride crystallites are crucial for photonic applications. For example, to be a promising optical functional material, the size of the crystallites should be smaller than at least half of the wavelength of the light used while the size distribution should be narrow and the crystallites should possess a homogeneous spatial distribution. In this way, according to the scattering theory developed by Rayleigh, a complete transparency of a light transmitting material can be attained.

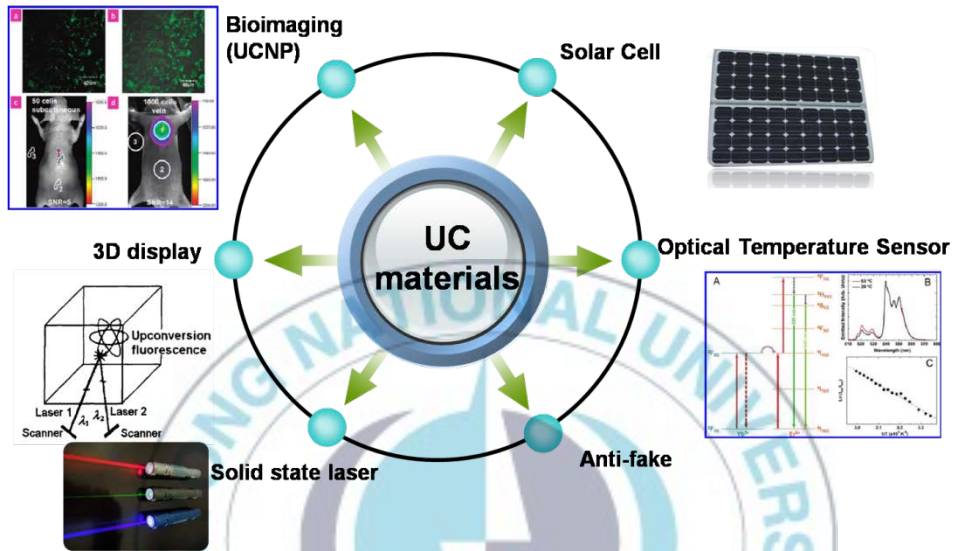


Figure 2.11 Diagrammatic representation of the variety of applications of UC materials.

The difference in the value of refractive index between the amorphous and crystalline phases should be less than 0.1. However, according to Beall and Pinckney, based on Hopper's model, crystal sizes of 30 nm and differences in refractive index of 0.3 may be an acceptable limit, provided that the crystal spacing is not greater than six times the average crystal size. Transparent Glass Ceramic (TGC) can also be obtained with even larger crystal sizes if optical isotropy is achieved within the glass ceramic. Consequently, the selection of the oxide glass composition and the fluoride phase composition is the key factor in obtaining the desired glass ceramic materials. The Er^{3+} ions are quite interesting due to their emission at $1.5 \mu\text{m}$ and the green UC obtained under near infrared excitation. In order to improve these emissions, the sensitization of this nanocomposite with Yb^{3+} ions may be a good choice because of the efficient energy transfer process from Yb^{3+} to Er^{3+} ions [38,39].

2.7 UC nanoparticles

In the late 1990s, Lanthanide-doped nanoparticles emerged due to the prevalent work on nanotechnology, thus causing a landmark in the modern lanthanide research. Although the optical transitions in lanthanide-doped nanoparticles resemble those in bulk materials, the nanostructure amenable to surface modifications provides new opportunities for research. Particularly, these nanoparticles are promising alternatives to molecular fluorophores for bioapplications. Their unique optical properties, such as large Stokes shift and nonblinking, have enabled a strong rival to the conventional luminescent probes

including single-molecule tracking and deep tissue imaging. Despite the promising aspects of these nanomaterials, one immediate need lies in front of the materials chemists is the synthesis of nanoparticles with tunable emissions, which are essential for applications in multiplexed imaging and sensing [40].



III. Experimental Method

3.1 Synthesis methods

3.1.1 Conventional solid state reaction and planetary ball milling method

A basic and well known preparation method namely, the solid state reaction method has the obvious advantage of simplicity. The solid state reaction method is the most widely used method for the preparation of polycrystalline solids from a mixture of solids as starting materials. Generally, solids do not react together at room temperature at normal time scales and therefore it becomes necessary to heat them to much higher temperatures, often to 1000 to 1500 °C in order for the appreciable rate reaction to take place.

The planetary ball mill is introduced to improve the process of conventional solid state reaction, which is affected by the impact of grinding balls. The processing of materials by planetary ball milling method is an attractive method for preparing novel materials [80,81], which decreases the crystalline and particle size and induces the continuous formation of structural defects through the cycling cut and deformation of large crystallites [82]. The most important advantage of the planetary ball milling process is that it can be used to synthesize the designed compounds at room temperature in a nanometer scale.

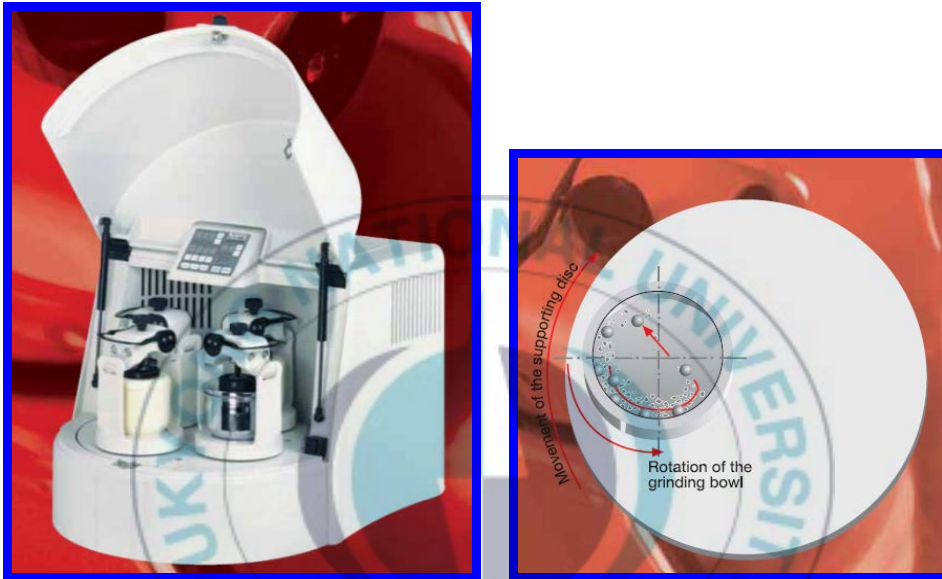


Figure 3.1 Depiction of the planetary ball mill “Pulverisette 5” and its working mechanism involved.

A description of the motion of this machine and its working mechanism are shown in Fig. 3.1

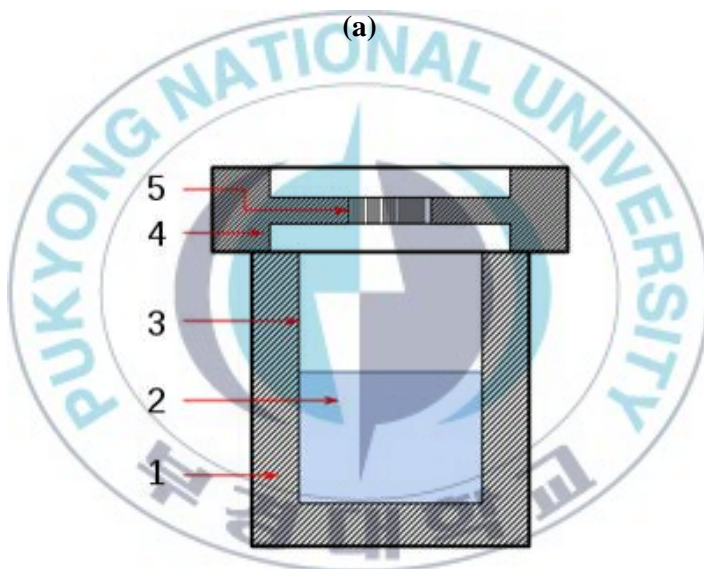
3.1.2 Solvothermal method

Solvothermal synthesis is a method similar to that of the hydrothermal route, where the synthesis is carried out in a stainless steel autoclave, the only difference being that the precursor solution is usually not aqueous (however, this is not always the case in all literature use of the expression). Using the solvothermal route one can gain the benefits of both the sol-gel [83] and hydrothermal routes [84]. Thus solvothermal synthesis allows for the precise control over the size, shape distribution, and crystallinity of metaloxide nanoparticles or nanostructures. These characteristics can be altered by changing the following experimental parameters, namely the reaction temperature, reaction time, solvent type, surfactant type, and precursor type.

Solvothermal synthesis has been used in laboratory to make nanostructured titanium dioxide [85], graphene [86], carbon [87] and other materials. For example, the high photocatalytic capacity of TiO_2 leads to the degradation of organic [88,89] and biological molecules [90,91] into smaller and less harmful compounds. Because of their small size, TiO_2 nanostructures provide an increased surface area at which photocatalytic reactions may occur, and thus increasing their activity. This photocatalytic activity may be applied for air purification [92], self-sterilization [93], water purification [94] and molecular hydrogen production [95].



(a)



(b)

Figure 3.2 (a) The autoclave system and (b) schematic diagram of solvothermal synthesis setup. (1) Stainless steel autoclave (2) precursor solution (3) teflon liner (4) stainless steel lid (5) spring.

Thus the ability of solvothermal synthesis to precisely tailor TiO₂ nanostructures has the potential to maximize the efficiency of those nanostructures in applications. The autoclave system and schematic diagram of solvothermal synthesis setup were shown in Fig. 3.2 (a) and (b), respectively.

3.2 Characterization Techniques

3.2.1 X-ray diffractometer (XRD)

For determination of crystal structure and lattice parameter, samples were investigated by X-ray diffractometer (XRD). It can analyze the structure of a material from the scattering pattern produced when a beam of radiation or particles interacts with it. The XRD profiles were measured within the range of 10-80° in steps of 0.02° using X-ray diffractometer (X'PERT PRO, PHILIPS) with CuK_α = 1.5406 Å radiation at 40 kV and 30 mA as shown in Fig. 3.3.

X-ray diffractometers consist of an X-ray generator, a goniometer, sample holder and X-ray detector such as photographic film or movable proportional counter. X-ray tubes generate X-rays by bombarding a metal target with high-energy (10 – 100 KeV) electrons that knock out core electrons. An electron in an outer shell fills the hole in the inner shell and emits an X-ray photon. The data obtained from the XRD were compared with the Joint Committee Powder Diffraction Standard (JCPDS) cards and the unit cell parameters were calculated using Powder-X diffraction analysis software.



Figure 3.3 X-ray diffractometer (X'PERT PRO, PHILIPS).

3.2.2 Field Emission Scanning Electron Microscope (FE-SEM)

The morphology and size of samples were measured by means of field emission scanning electron microscope (FE-SEM, JEOL JSM-6700F). The table 3.1 represents the specification of FE-SEM.

Table 3.1 Specifications of FE-SEM

SE resolution	1.0 nm (15 kV), 2.2 nm (1 kV)
Magnification	×25 ~ ×19,000 (LM mode), ×100 ~ ×300,000 (SEM mode)
Accelerating voltage	0.5 kV ~ 30 kV
Probe current	10^{-13} A ~ 10^{-9} A
Electron gun	Conical electron mode FEG
Objective lens	Strongly excited conical lens
Specimen Aperture	Fixed
EDS	Energy Dispersive X-ray Spectrometer

3.2.3 Upconversion spectrophotometer

Fig. 3.4 shows the schematic diagram of UC photoluminescence. A laser diode (LD) of 975 nm was used as the pumping source to get the luminescence spectra. The maximum laser power was about 1W, but for stable operation a power of 500 mW was chosen. The emitted light was focused into the monochromator and was detected by using a photomultiplier tube. The signal was fed to a digital oscilloscope.

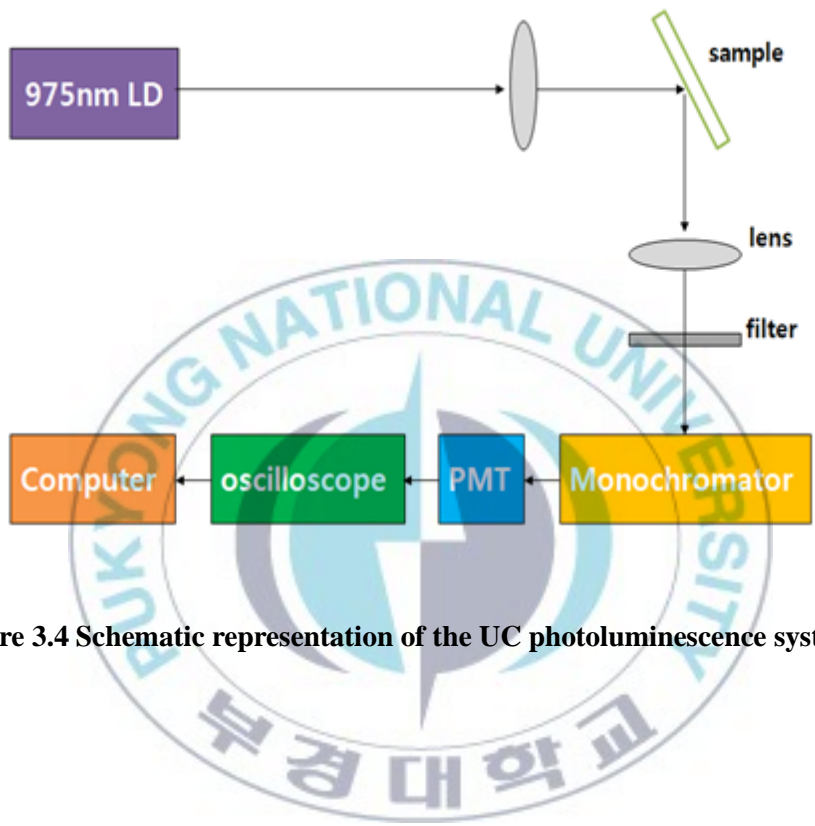


Figure 3.4 Schematic representation of the UC photoluminescence system.

IV. Results and Discussions

4.1 UC luminescence properties of Er³⁺ doped YAlO₃ (YAP) nanophosphors

Erbium doped yttrium orthoaluminate YAlO₃ (YAP) crystal is a well known laser material due to its high mechanical hardness, considerable heat conductivity and optical properties. Upconversion characteristics of YAP doped with Er³⁺ have been studied in bulk crystals [96-98] and nanophosphors [99]. The upconversion mechanism in Er³⁺ doped YAP crystals have been investigated under different pumping conditions and dopant concentrations [100,101]. For understanding the upconversion mechanism, it is very important to investigate the variation of pump power dependence of UC luminescence with different Er³⁺ concentration. But less report has been found on the effect of the dopant concentration on UC luminescence process. High concentrated Er:YAG and low-concentrated Er-YAP were compared [102] and Gd₂O₃ crystal doped with Er³⁺ and Yb³⁺ at different Yb³⁺ concentrations [103].

In this work, Er³⁺ doped Yttrium aluminum perovoskite (YAP:YAlO₃) nanophosphors with different concentrations (0.01, 0.02, 0.03, 0.05 and 0.07 mol) were synthesized by solvo-thermal reaction method. The stoichiometric amounts of high purity yttrium nitrate hexahydrate (Y(NO₃)₃·6H₂O, 99.99% Aldrich), erbium nitrate pentahydrate ((Er(NO₃)₃)₃·5H₂O, 99.99% Aldrich) and aluminum isopropoxide (((CH₃)₂CHO)₃Al, 98% Aldrich) were dissolved in 20 ml of 2-propanol. All reagents were used without any further purification and stirred

vigorously by using magnetic stirrer until the homogeneous solution was formed and transferred into stainless steel autoclave with a Teflon liner. It was then reacted at 210 °C and maintained for 12 h with magnetic stirring to make stable networks of Y–O–Al and Er–O–Al. After cooling gradually down to room temperature and then dried for a day in ambient vacuum. The dried powder was sintered at 1100 °C for 5 h.

X-ray diffraction patterns of Er³⁺:YAP nanophosphors were recorded on X'PERT-MPD system. The morphology of the Er³⁺:YAP nanophosphors sintered at 1100 °C was examined by means of Field Emission Scanning Electron Microscope (JEOL JSM-6700F). The upconversion emission spectrum was measured at room temperature by exciting the erbium ions under the excitation of 975 nm diode laser, and the signal was detected by a photomultiplier tube and finally amplified by a standard lock-in technique. The maximum laser power was about 1 W, but for stable operation a power of 500 mW was chosen.

Fig. 4.1 shows the X-ray diffraction patterns of YAP:Er³⁺ nanophosphors doping with 0.01 mol Er³⁺. It shows a typical orthorhombic crystal phase and basically accords with the standard X-ray diffraction card JCPDS 33–0041. In general, the crystallite size can be estimated by using the Scherrer's equation. The strongest diffraction peaks are used to calculate the crystallite size of YAP:Er³⁺ nanophosphor, sintered at 1100 °C, which yields an average value of about 68 nm.

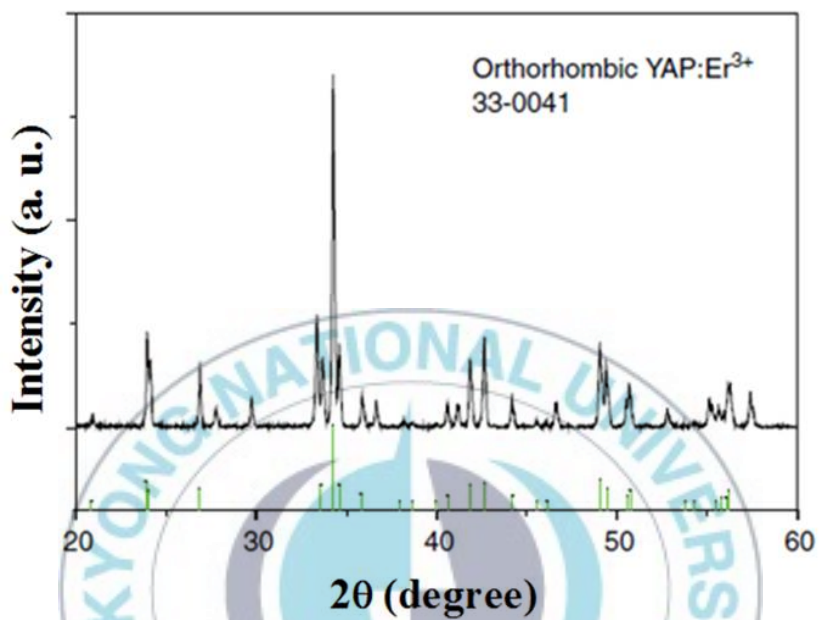


Figure 4.1 XRD patterns of YAP:Er³⁺ nanophosphors and the reference data of JCPDS card No. 33-0041 for orthorhombic YAP.

Fig. 4.2 shows the SEM image of YAP:Er³⁺ nanophosphors and from which round-shaped particles are noticed, those might be due to the occurrence of agglomerations amongst the YAP particles during the annealing period of the sample.

Fig. 4.3 shows the upconversion emission spectra of YAP:Er³⁺ nanophosphors with different concentrations (0.01, 0.02, 0.03, 0.05 and 0.07 mol) under the excitation of 975 nm LD. There were two main emission bands: the red emission centered at 660 nm and green centered at 550 nm. All the transitions are related with the transition from the excited states of the Er³⁺ ion to its ground state ⁴I_{15/2}; the intense green portion of the spectrum has originated from the ²H_{11/2} and ⁴S_{3/2} excited states centered and another strong emission is the red emission centered at 660 nm, corresponding to the transition of ⁴F_{9/2} → ⁴I_{15/2}.

The intensity of green emission increased almost linearly in going from the 0.01 mol sample to the 0.05 mol one and then showing a slight decrease for the Er³⁺ concentration over 0.07 mol. However, the intensity of red emission increased more rapidly as Er³⁺ concentration was increased. The enhancement of the red upconversion (UC) emission has been also reported in other systems like the bulk and nanocrystalline Y₂O₃ doped with Er³⁺ at various concentration [104-106].

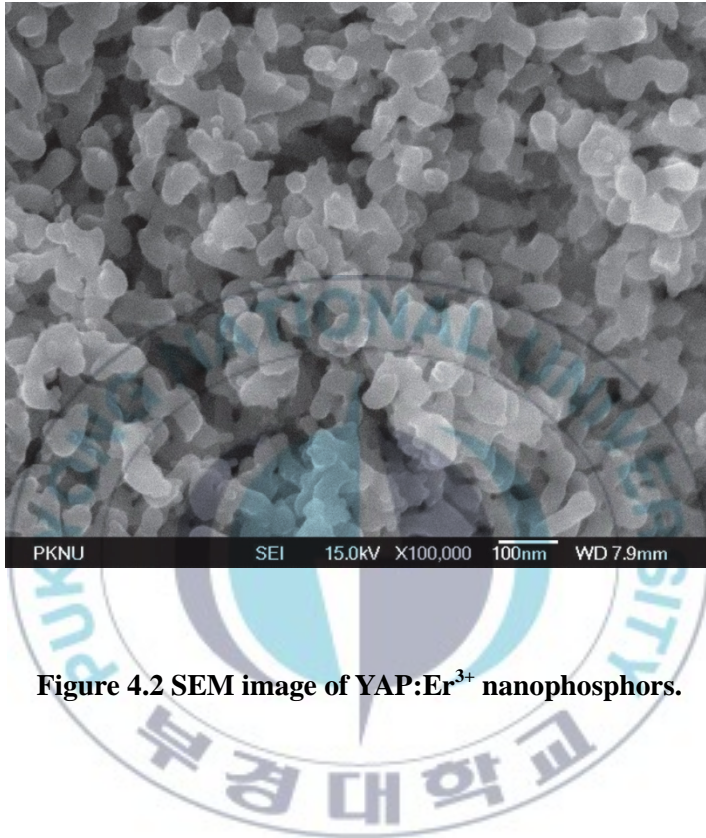


Figure 4.2 SEM image of YAP:Er³⁺ nanophosphors.

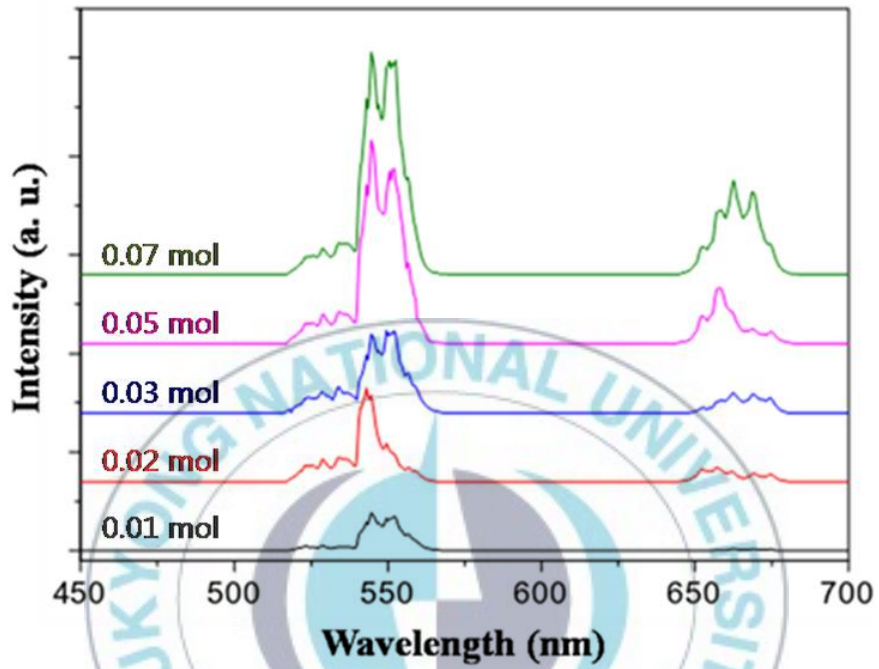


Figure 4.3 UC luminescence spectra of YAP:Er³⁺ with different concentrations under the excitation of 975 nm LD.

Fig. 4.4 shows the energy level diagrams of the Er^{3+} ion in YAlO_3 as well as the proposed UC processes under excitation at 975 nm. The green transitions from the ${}^2\text{H}_{11/2}$, ${}^4\text{S}_{3/2} \rightarrow {}^4\text{I}_{15/2}$ comes from ESA and ETU. In case of ESA, the absorption of a first IR pump-photon excites the electrons from the ground state to the ${}^4\text{I}_{11/2}$ state and subsequently ESA of a second 975 pump photon promotes the electrons to the ${}^4\text{F}_{7/2}$ level, and finally relaxes to ${}^2\text{H}_{11/2}$, ${}^4\text{S}_{3/2}$ levels via a multi-phonon process. Another possibility is the ETU processes that occurs between two Er^{3+} ions occupied in the ${}^4\text{I}_{11/2}$ level. This process is pictured in Fig. 4.4.

The transition of red emission is the ${}^4\text{F}_{9/2} \rightarrow {}^4\text{I}_{15/2}$, the upper state ${}^4\text{F}_{9/2}$ can be populated from ${}^4\text{S}_{3/2}$ by multiphonon relaxation. The multi-phonon relaxation rate is dependent of the energy gap (ΔE) between neighbor states and highest optical phonon energy of samples ($h\nu$). If the energy gap ΔE is larger than five phonon energies, multi-phonon relaxation rate can be neglected. The energy gap between ${}^4\text{S}_{3/2}$ and ${}^4\text{F}_{9/2}$ is 3140 cm^{-1} is larger by a factor of 5.5 than the phonon energy of the YAP lattice (570 cm^{-1}) [107-109], the multi-phonon relaxation rate from ${}^4\text{S}_{3/2}$ level to ${}^4\text{F}_{9/2}$ is very low. Therefore, the red emission state of ${}^4\text{F}_{9/2}$ must be populated another route. This state can be populated from the transition of ${}^4\text{I}_{13/2} \rightarrow {}^4\text{F}_{9/2}$ under the 975 nm excitation. The population of ${}^4\text{I}_{13/2}$ level can be fed from the ${}^4\text{I}_{11/2}$ level by multi-phonon relaxation or cross-relaxation (${}^2\text{H}_{11/2} \rightarrow {}^4\text{I}_{9/2}$; ${}^4\text{I}_{15/2} \rightarrow {}^4\text{I}_{13/2}$) process. As the energy gap between ${}^4\text{I}_{13/2}$ and ${}^4\text{I}_{11/2}$ level is $3,636 \text{ cm}^{-1}$, the multi-phonon relaxation of ${}^4\text{I}_{11/2} \rightarrow {}^4\text{I}_{13/2}$ can be neglected. However, the cross-relaxation (CR) rate is dependent on the population of the

$^2H_{11/2}$ state and on the distance between Er^{3+} ions. As can be seen in Fig. 4.3, red UC emission of YAP doped with 0.01 mol Er^{3+} ions can hardly arise, but the red emission is increased with increasing concentration of Er^{3+} . Therefore the UC red emission is attributed to cross-relaxation.

To get a better understanding of upconversion of YAP: Er^{3+} phosphors, the luminescence intensity versus pump power for YAP: Er^{3+} phosphors was investigated. Fig. 4.5 shows the log-log plots of pump power dependence of the green and red emissions with the different Er^{3+} concentration of Er^{3+} ions. To investigate the excitation mechanisms for populating the $^4S_{3/2}$ and $^4F_{9/2}$ levels after IR excitation, we have measured the UC emission intensities at 550 and 660 nm as a function of pumping power. The UC emission intensity I_{em} depends on the incident pump power P_{pump} according to the relation $I_{em} \propto (P_{pump})^n$, where n is the number of photons involved in the pumping mechanism. For the Er^{3+} 0.01 mol sample (Fig. 4.5 (a)), the n values for the green and red emissions were 1.77 and 2.01, which means that the UC luminescence of the $^2H_{11/2}$, $^4S_{3/2}$ and $^4F_{9/2}$ level might be populated via a two-photon absorption processes. For the near infra red (NIR: $^4I_{11/2}$ level) emission, the slope n was about 1, which shows that this state was populated via single photon absorption from the ground state. For the 0.07 mol sample (Fig. 4.5 (b)), we obtained $n \approx 1$ for both of the green and red emissions, and for NIR emission, $n = 0.84$. It is unexpected results, since it is known that the pump power dependence of the green and red upconversion is attributed to the two photon process. It means that at high Er^{3+} concentrations, only a one-photon excitation is needed for the green and red UC emission.

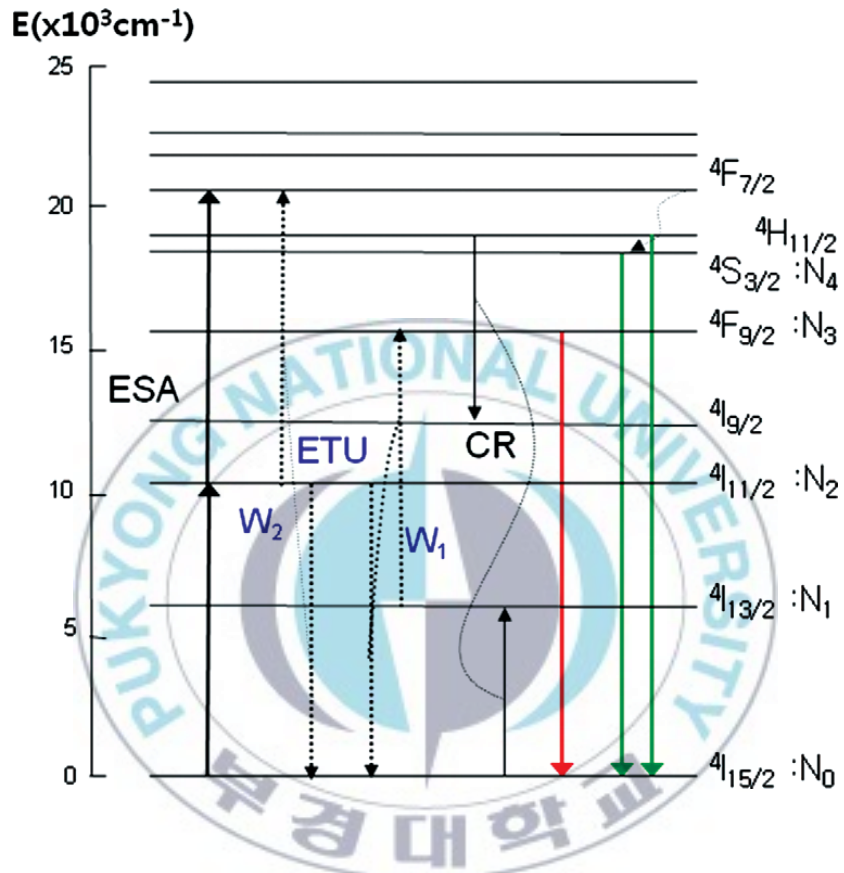


Figure 4.4 Energy level diagram of the Er³⁺ ions and mechanisms for the UC luminescence in YAlO₃.

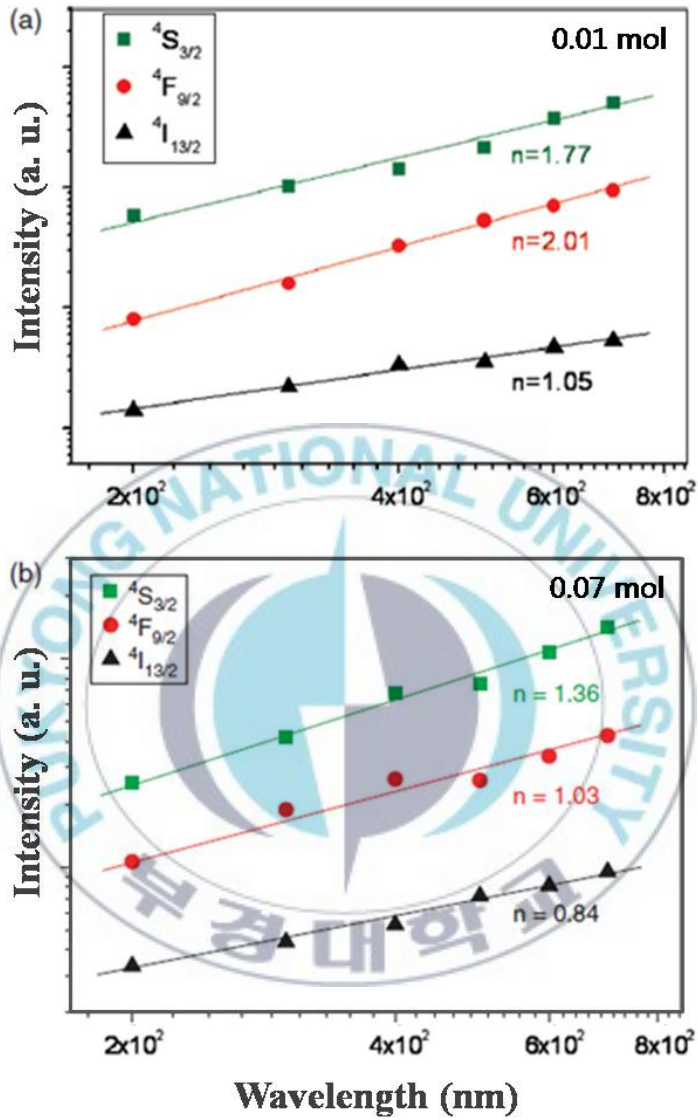


Figure 4.5 Pump power dependence of UC photoluminescence in YAP nanophosphors doped with (a) 0.01 mol and (b) 0.07 mol Er³⁺ ions.

To interpret theoretically the power dependence behavior we utilized the following steady-state equation:

$$dN_4/dt = R N_2 + W_2 N_2^2 - C_{CR} N_4 N_0 - A_4 N_4 = 0 \quad (4.1)$$

$$dN_3/dt = W_1 N_2 N_1 - A_3 N_3 = 0 \quad (4.2)$$

$$dN_2/dt = R N_0 + C_{CR} N_4 N_0 - 2W_2 N_2^2 - W_1 N_2 N_1 - A_2 N_2 = 0 \quad (4.3)$$

$$dN_1/dt = C_{CR} N_4 N_0 - W_1 N_2 N_1 - A_1 N_1 = 0 \quad (4.4)$$

Where, N_0 , N_1 , N_2 , N_3 and N_4 are the population densities of ${}^4I_{15/2}$, ${}^4I_{13/2}$, ${}^4I_{11/2}$, ${}^4F_{9/2}$, and ${}^4S_{3/2}$ states, respectively and assume the ground state population N_0 is constant. A_i is radiative decay rate of each level and W_1 and W_2 are energy transfer rates of the ${}^4I_{11/2} \rightarrow {}^4I_{15/2}$; ${}^4I_{13/2} \rightarrow {}^4F_{9/2}$ transitions and ${}^4I_{11/2} \rightarrow {}^4I_{15/2}$; ${}^2I_{11/2} \rightarrow {}^4F_{7/2}$ transitions, respectively. And C_{CR} is the cross-relaxation rate of ${}^2H_{11/2} \rightarrow {}^4I_{9/2}$; ${}^4I_{15/2} \rightarrow {}^4I_{13/2}$ transition. The absorption coefficient R_i of ${}^4I_{11/2}$ level is $\sigma/h\nu P$ with σ the absorption cross section, h Planck's constant, ν the pump, and P the incident pump power. In Eq. (4.4), the radiative decay of ${}^4I_{13/2}$ level is omitted as compared to the UC rate due to its long lifetime. At lower Er^{3+} concentrations, the linear decay rate from the ${}^4I_{11/2}$ state, $A_2 N_2$ should be larger than the UC rate, and thus, the UC rate $2W_2 N_2^2 + W_1 N_2 N_1$ in Eq. (4.3) can be neglected. From Eqs. (4.1 ~ 4.4), we get

$$N_4 = W_2 N_2^2 / (A_4 + C_{CR} N_0) \propto P^2 \quad (4.5)$$

$$N_3 = C_{CR} N_0 W_2 W_1 N_2^2 / A_3 W_1 (A_4 + C_{CR} N_0) \propto P^2 \quad (4.6)$$

$$N_1 = C_{CR} W_2 N_0 N_2 / W_1 (A_4 + C_{CR} N_0) \propto P \quad (4.7)$$

These results agree well with the experiments of Fig. 4.5 (a), where the green and the red emissions were found to involve two-photon processes. At higher Er^{3+} concentration, the UC rate $2W_2N_2^2$, $W_1N_2N_1$ dominates and the linear decay A_2N_2 can be neglected in Eq. (4.3). In contrast, we have

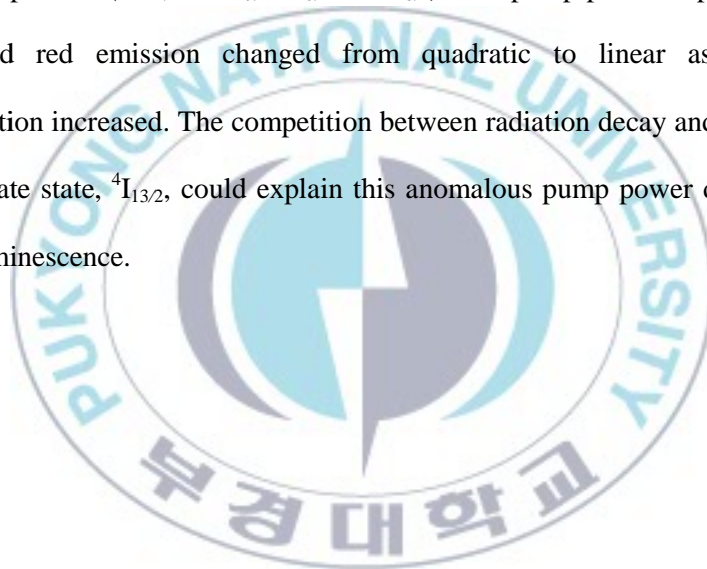
$$N_4 = W_2 N_2^2 / (A_4 + C_{CR} N_0) \propto P \quad (4.8)$$

$$N_3 = C_{CR} N_0 W_2 N_2^2 / A_3 W_1 (A_4 + C_{CR} N_0) \propto P \quad (4.9)$$

$$N_1 = C_{CR} W_2 N_0 N_2 / W_1 (A_4 + C_{CR} N_0) \propto P^{1/2} \quad (4.10)$$

These results give good explanation for anomalous behavior of pump power dependence at high Er^{3+} concentration; the result of Fig. 4.5(b).

In summary, different concentration (0.01, 0.02, 0.03, 0.05 and 0.07 mol) of Er^{3+} doped YAP nanophosphors were synthesized by solvothermal reaction method. There were two main emission bands: the red emission centered at 660 nm and green centered at 550 nm. Under the excitation of 975 nm laser diode, the green transitions from ${}^2\text{H}_{11/2}$, ${}^4\text{S}_{3/2} \rightarrow {}^4\text{I}_{15/2}$ of Er^{3+} ions are ESA and ETU. For high concentration of Er^{3+} ions, red emitting state, ${}^4\text{F}_{9/2}$, can be populated from the long-lived ${}^4\text{I}_{13/2}$ level by absorption of one laser photon, which follows cross-relaxation process (${}^2\text{H}_{11/2} \rightarrow {}^4\text{I}_{9/2}; {}^4\text{I}_{15/2} \rightarrow {}^4\text{I}_{13/2}$). The pump power dependence of green and red emission changed from quadratic to linear as Er^{3+} ion concentration increased. The competition between radiation decay and UC of the intermediate state, ${}^4\text{I}_{13/2}$, could explain this anomalous pump power dependence of UC luminescence.



4.2 UC luminescence properties of Er³⁺ and Yb³⁺ co-doped zirconium oxide

Upconversion luminescence, in which a material emits high energy photons via the absorbance of low-energy pumping photons, has attracted great interest. This is because materials displaying this phenomenon may have a wide range of applications as media for near-infrared (NIR) quantum counting devices, solid-state lasers, bioassays, high-density memories [110-114], and so on. In recent years, many nanocrystalline materials have been proposed as efficient upconverters, among which the wide band gap nanosized ZrO₂ has proven to be a good candidate for visible upconversion emission. The rare earth ions Ho³⁺, Pr³⁺, Tm³⁺, Tb³⁺, and Er³⁺ have also been investigated [115-121]. Among the candidates for upconversion materials, trivalent erbium has excellent upconversion properties [122,123]. The Yb³⁺ ion exhibits a strong and broad absorption band between 800 and 1100 nm and can easily be pumped with infrared laser diodes that are commercially available, giving rise to upconversion in the visible spectral region. For a system co-doped with Er³⁺ and Yb³⁺ ions, the large spectral overlap between Yb³⁺ emission (²F_{5/2} - ²F_{7/2}) and Er³⁺ absorption (⁴I_{15/2} - ⁴I_{11/2}) results in an efficient energy transfer process [124,125]. Red and green emissions from Er³⁺ doped and Er³⁺, Yb³⁺ co-doped oxide nanocrystals have been widely reported [126,128] and some studies showed strong emission from ZrO₂ [129,130]. However, only a few studies on the analysis of the ion concentration effect have been reported [131,132].

In this thesis, $\text{ZrO}_2:\text{Er}^{3+}$ and $\text{ZrO}_2:\text{Er}^{3+}, \text{Yb}^{3+}$ phosphors were synthesized by a solvothermal reaction method with the following starting materials: $\text{ZrO}(\text{NO}_3)_2 \cdot 2\text{H}_2\text{O}$ (99.9%, Aldrich), $\text{Er}(\text{NO}_3)_3 \cdot 5\text{H}_2\text{O}$ (99.9%, Aldrich) and $\text{Yb}(\text{NO}_3)_3 \cdot 5\text{H}_2\text{O}$ (99.9%, Aldrich). Firstly, the starting materials were dissolved in 20 ml of 2-propanol for to $\text{Zr}_{1-x-y}\text{Er}_x\text{Yb}_y\text{O}_2$ ($x = 0:0.1$ mol; $y = 0, 0.01, 0.05, 0.1$ mol). The starting materials were used without any further purification and were stirred vigorously using a magnetic stirrer until a homogeneous solution was formed, which was then transferred into a stainless steel autoclave with a Teflon liner. It was then reacted at 250°C and maintained for 12 h with stirring with a magnetic stirrer to form a stable network. After cooling gradually to room temperature and then drying for a day, the obtained powder samples were sintered in air at $800, 1000$ and 1200°C for 2 h.

The crystal structure and phase of the synthesized samples were characterized by X-ray diffraction (XRD) using a Philips X'Pert/MPD diffraction system with $\text{Cu K}_{\alpha 1}$ radiation ($\lambda = 1.54056 \text{ \AA}$). The surface morphology of the powders was examined by field-emission scanning electron microscopy (FESEM; JEOL JSM-6700). The upconversion emission spectrum was measured at room temperature by exciting the erbium ions using a 975 nm laser diode (LD) and a photomultiplier tube to detect the signal, which was amplified by a standard lock-in technique. The maximum laser power was about 1 W, but a power of 600 mW was chosen for stable operation.

The XRD patterns of $\text{ZrO}_2:\text{Er}^{3+}$ and $\text{ZrO}_2:\text{Er}^{3+}$ co-doped with different concentrations (0, 0.01, 0.05, and 0.1 mol) of Yb^{3+} sintered at 800 ~ 1200 °C are shown in Fig. 4.6. For $\text{ZrO}_2:\text{Er}^{3+}$ co-doped with low concentrations (0, 0.01 mol) of Yb^{3+} , it is shown that the crystal structure change from the tetragonal to monoclinic phase as the sintering temperature is increased. As the concentration of Yb^{3+} ions increases to 0.05 and 0.1 mol, the $\text{ZrO}_2:\text{Er}^{3+}$ phosphors have a very stable tetragonal phase. It is known that ZrO_2 can exist in three distinct crystal phases: the room temperature phase, the monoclinic phase and the two high-temperature phases, tetragonal and cubic [133,134]. However, when MgO , Y_2O_3 , CaO or rare earth metal ions are added, a zirconia crystal shows a stable tetragonal phase; moreover with increasing concentration of impurities that promote the stabilization, the temperature in the phase change from tetragonal to monoclinic increases [135]. This confirms that Yb^{3+} ion concentration influences the stability of the tetragonal phase, as shown in Figs. 4.6 (c) and (d).

Fig. 4.7 shows the SEM images for $\text{ZrO}_2:\text{Er}^{3+}$ phosphors co-doped with different concentrations of Yb^{3+} sintered at 1000 °C. As shown in Fig. 4.7, the sizes of the particles are in the range from 300 nm to 1.5 μm and nearly all the particles are spherical. It is particularly well known that, phosphors with spherical particles are of great importance because of their high packing density, limited light scattering, bright luminescence, high definition, and high screen packing density [136].

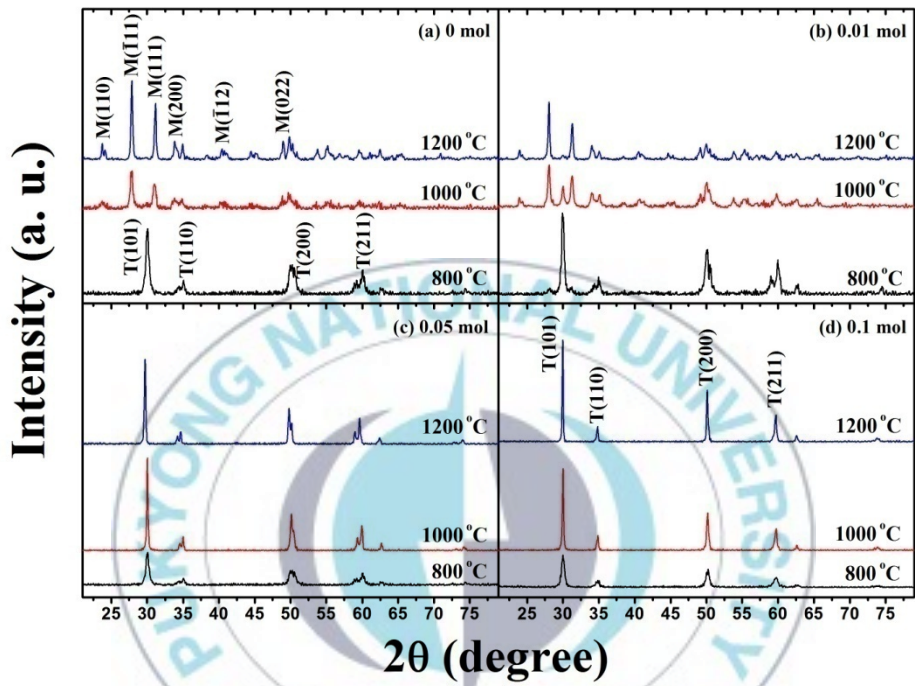


Figure 4.6 XRD patterns of ZrO₂:Er³⁺ and ZrO₂:Er³⁺ co-doped with different concentrations of Yb³⁺ sintered at 800 ~ 1200 °C.

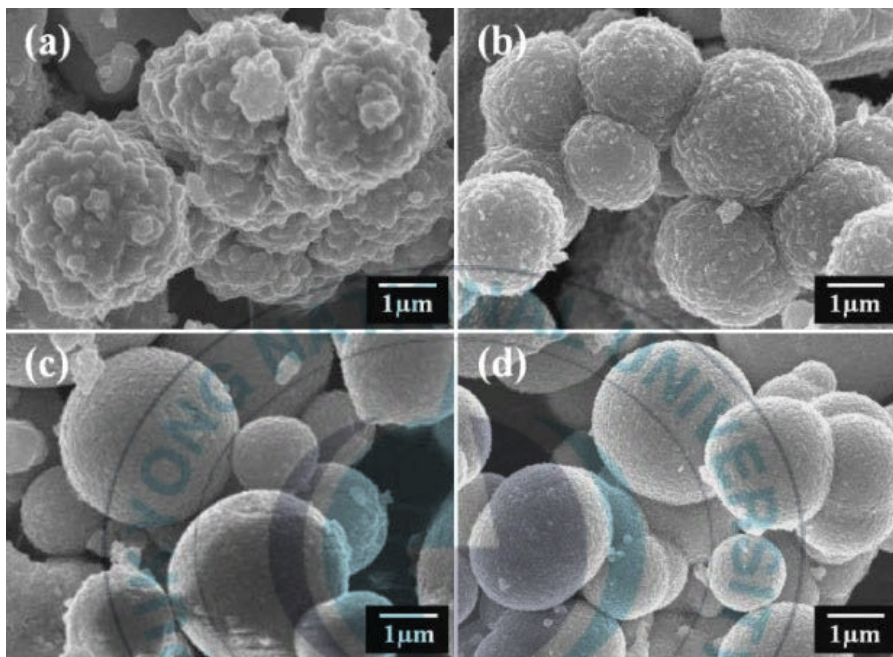


Figure 4.7 SEM images for different of Yb^{3+} co-doped $\text{ZrO}_2:\text{Er}^{3+}$ phosphors sintered at 1000 °C.

Fig. 4.8 shows the upconversion spectra of $\text{ZrO}_2:\text{Er}^{3+}$, Yb^{3+} phosphors sintered at 800, 1000, and 1200 °C that have been excited by a 975 nm LD. The spectra have two upconverted emission bands. One upconversion emission peak is located in the 520 ~ 570 nm regions, while the other is located in the 635 ~ 710 nm regions. The former band is attributed to the ${}^4\text{H}_{11/2}, {}^4\text{S}_{3/2} \rightarrow {}^4\text{I}_{15/2}$ transition and the latter band is attributed to the ${}^4\text{F}_{9/2} \rightarrow {}^4\text{I}_{15/2}$ transition. The upconversion emission intensity decreases as the crystal structure changes from the tetragonal to monoclinic phase (0, 0.01 mol of Yb^{3+}). However, in the case of the stable tetragonal phase (0.05, 0.1 mol of Yb^{3+}), the upconversion emission intensity increases at higher sintering temperatures, and the intensity of the red emission is higher than that of the green emission. This indicates that the concentration of Yb^{3+} ions affects the upconversion intensity. Therefore, depending on the concentration of Yb^{3+} , the crystal structure is stabilized and its upconversion intensity is increased.

Fig. 4.9 shows the upconversion emission spectra for $\text{ZrO}_2:\text{Er}^{3+}$ phosphors co-doped with different concentrations of Yb^{3+} sintered at 1000 °C. The green emission intensity increased almost linearly as the concentration of Yb^{3+} ions increased from 0 to 0.05 mol, but then showed a decrease with further increases in Yb^{3+} ion concentration above 0.05 mol. The red emission intensity increased more rapidly than the green emission intensity as Yb^{3+} concentration increased. The inset figure shows the ratio of red emission intensity of Er^{3+} and Yb^{3+} co-doped ZrO_2 to that of ZrO_2 doped with only Er^{3+} ions, which raised with increasing Yb^{3+} concentration.

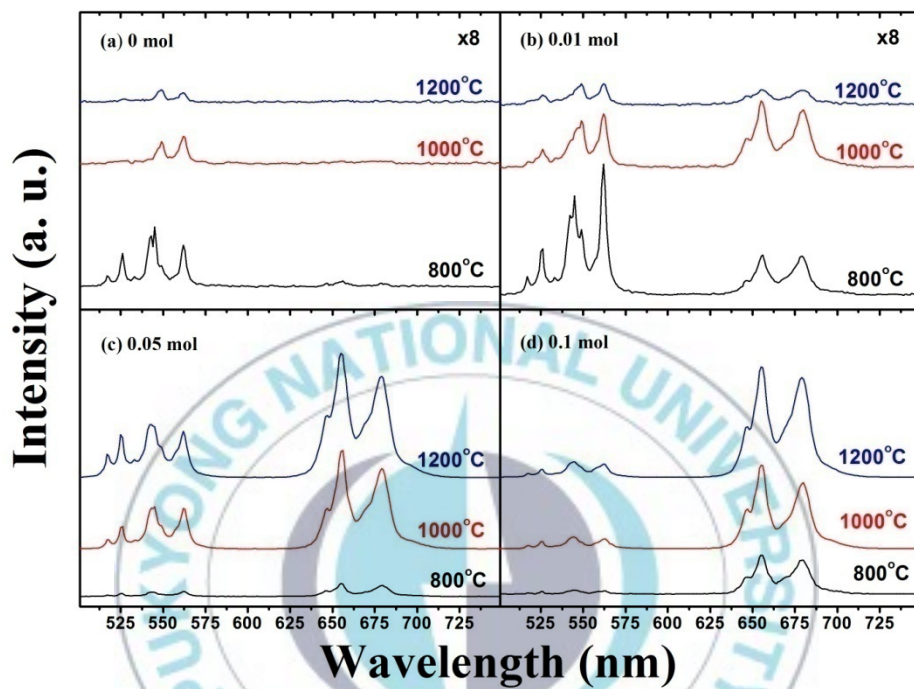


Figure 4.8 UC emission spectra of Yb^{3+} co-doped $\text{ZrO}_2\text{:Er}^{3+}$ at 800 ~ 1200 °C with (a) 0, (b) 0.01, (c) 0.05 and (d) 0.1 mol of Yb^{3+} .

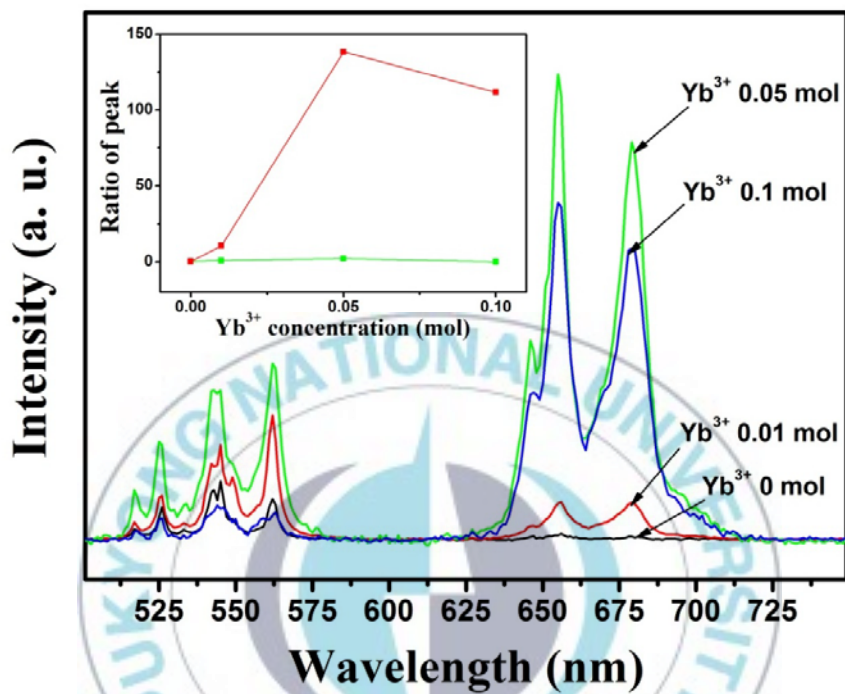


Figure 4.9 UC spectra of $\text{ZrO}_2:\text{Er}^{3+}, \text{Yb}^{3+}$ phosphors at $1000\text{ }^\circ\text{C}$. The inset shows the intensity ratio of red to green emission.

The red emission intensity is about 70 times higher than the green emission intensity for doping with 0.05 mol of Yb^{3+} ion. Above the 0.05 mol of the Yb^{3+} concentration, the intensities of emission were decreased. The upconversion emission spectra of ZrO_2 phosphors show that optimum concentration of Yb^{3+} ions in ZrO_2 matrix is 0.05 mol with fixed Er^{3+} concentration (0.01 mol). These results indicated that the Yb^{3+} ion plays an important role in the upconversion emission process. Fig. 4.10 shows the Commission Internationale de l'Eclairage (CIE) chromaticity diagrams of Er^{3+} , Yb^{3+} co-doped ZrO_2 under excitation at 975 nm. As shown in Fig. 4.10, the total luminescence appears from green to red color with increasing Yb^{3+} concentrations. The chromaticity coordinates of x and y were from 0.370 to 0.547 and from 0.610 to 0.443, respectively.

To explain the enhanced red emission, we propose the energy level diagram of Er^{3+} and Yb^{3+} ions on the basis, which the possible upconversion mechanism is shown in Fig. 4.11. The green emission from $^2\text{H}_{11/2}$ and $^4\text{S}_{3/2}$ to the $^4\text{I}_{15/2}$ level comes from ESA and ETU. In the case of ESA, the absorption of the first IR pump photon excites the electrons from the ground state to the $^4\text{I}_{11/2}$ state and subsequently the ESA of the second 975 nm pump photon promotes the excitation of the electrons to the $^4\text{F}_{7/2}$ level, and the system finally relaxes into the $^2\text{H}_{11/2}$ and $^4\text{S}_{3/2}$ levels by a multiphonon process. However, the ESAs of Er^{3+} ions are neglected, since the Yb^{3+} ion has a much larger absorption cross section and an efficient energy transfer to Er^{3+} ions under laser excitation of 975 nm [132,137]. Therefore, the ETU process predominantly occurs between Er^{3+} and Yb^{3+} ions.

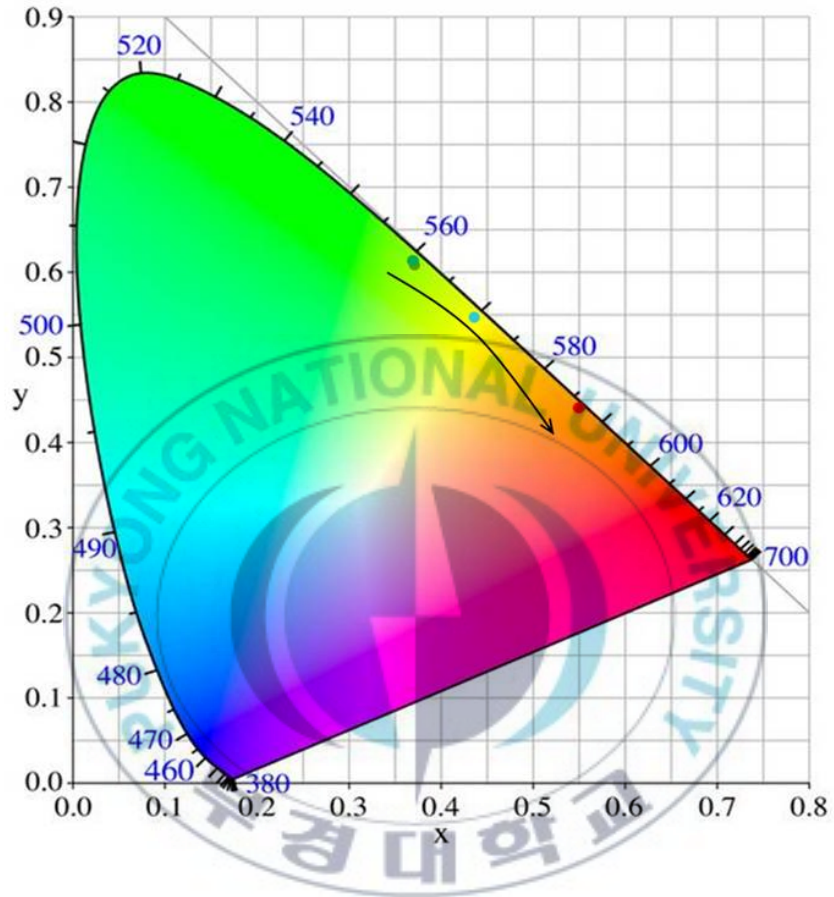


Figure 4.10 CIE chromaticity coordinates of Er³⁺, Yb³⁺ co-doped ZrO₂ with increasing Yb³⁺ concentrations.

The red emission shows the ${}^4F_{9/2} \rightarrow {}^4I_{15/2}$ transition, and the upper state ${}^4F_{9/2}$ can be populated from the ${}^4S_{3/2}$ level by multiphonon relaxation. However, the multiphonon relaxation rate from ${}^4S_{3/2}$ to the ${}^4F_{9/2}$ level is very low, as shown for ZrO_2 doped with only Er^{3+} ions, because the energy gap between the ${}^4F_{7/2}$ and ${}^4S_{3/2}$ levels is about $3,060\text{ cm}^{-1}$, which is larger than the maximum optical phonon energy of ZrO_2 (470 cm^{-1}). Therefore, the red emission state of ${}^4F_{9/2}$ must be populated via another route. We considered the red emission mechanisms excited from the ${}^4I_{13/2}$ level, in which case population processes of the ${}^4I_{13/2}$ level play a key role in the red upconversion emission. One possible mechanism of the population of the ${}^4I_{13/2}$ level is a cross-relaxation (CR) process, ${}^2H_{11/2} \rightarrow {}^4I_{9/2}; {}^4I_{15/2} \rightarrow {}^4I_{13/2}$. It is well known that the CR rate is dependent on the distance between Er^{3+} ions. However, the red upconversion emission of Er^{3+} doped ZrO_2 hardly arises. The red emission may appear at higher concentrations of Er^{3+} , but the Er^{3+} ion concentration of our sample is fixed at 0.01 mol. The other possible mechanism is an EBT process from Er^{3+} to Yb^{3+} ions, ${}^4S_{3/2}; {}^4I_{13/2}(Er^{3+}) \rightarrow {}^2F_{7/2}; {}^2F_{5/2}(Yb^{3+})$. As a result, increasing the concentration of Yb^{3+} ions causes the enhancement of energy transfer from ${}^2F_{5/2}; {}^2F_{7/2}(Yb^{3+})$ to ${}^4I_{11/2}; {}^4F_{7/2}(Er^{3+})$. Therefore, the EBT process becomes more prominent owing to the reduced average distance between the Yb^{3+} and Er^{3+} ions. The EBT process is the predominant route to the red emission level of ${}^4F_{9/2}$ over the CR process at high Yb^{3+} ion concentrations. It is known from much research that at high Yb^{3+} ion concentrations, the ${}^2H_{11/2}$ and ${}^4S_{3/2}$ level lifetimes decrease rapidly as Yb^{3+} concentration increases owing to the EBT process [138]. Although the transition

from the ${}^2\text{H}_{11/2}$ and ${}^4\text{S}_{3/2}$ levels to the ${}^4\text{I}_{13/2}$ level predominates and the population of the ${}^4\text{I}_{13/2}$ level increases, the transition from ${}^4\text{I}_{13/2}$ to ${}^4\text{F}_{9/2}$ occurs actively. Therefore, the red emission from the ${}^4\text{F}_{9/2}$ level is enhanced but the green emission from the ${}^4\text{S}_{3/2}$ level is suppressed. We therefore conclude that the saturation of the ${}^4\text{I}_{13/2}$ level arises from the efficient EBT process.

Fig. 4.12 shows the pump power dependence of green and red upconversion emission intensities, which was investigated to identify the EBT process. It is well known that the number of photons required to populate the upper emission state can be obtained by the following relation [139]:

$$I_{up} \propto P^n$$

where I_{up} is the upconversion emission intensity, P is the power of the pump laser and n is the number of laser photons required. Fig. 4.10 (a) shows that the n value of green emission is about 2, which indicates that the green emission is a two-photon process. For the red emission, the n value is 1.71 for 0.01 mol of Yb^{3+} ion, which also indicates a two photon process. As the Yb^{3+} ion concentration increases, the n value decreases to 1.22 at a concentration of 0.1 mol of Yb^{3+} ion. It seems that at high concentrations of Yb^{3+} ions, only the one-photon process is needed to excite the electrons to the ${}^4\text{F}_{9/2}$ state. The EBT process occurs, increasing the population of the ${}^4\text{I}_{13/2}$ level, which finally becomes saturated owing to the long life time of this level. It can then populate the ${}^4\text{F}_{9/2}$ level by a one photon process ETU (${}^2\text{F}_{5/2}; {}^2\text{F}_{7/2} \rightarrow {}^4\text{I}_{13/2}; {}^4\text{F}_{9/2}$) transition. Therefore, the EBT process can explain the increase in red emission intensity.

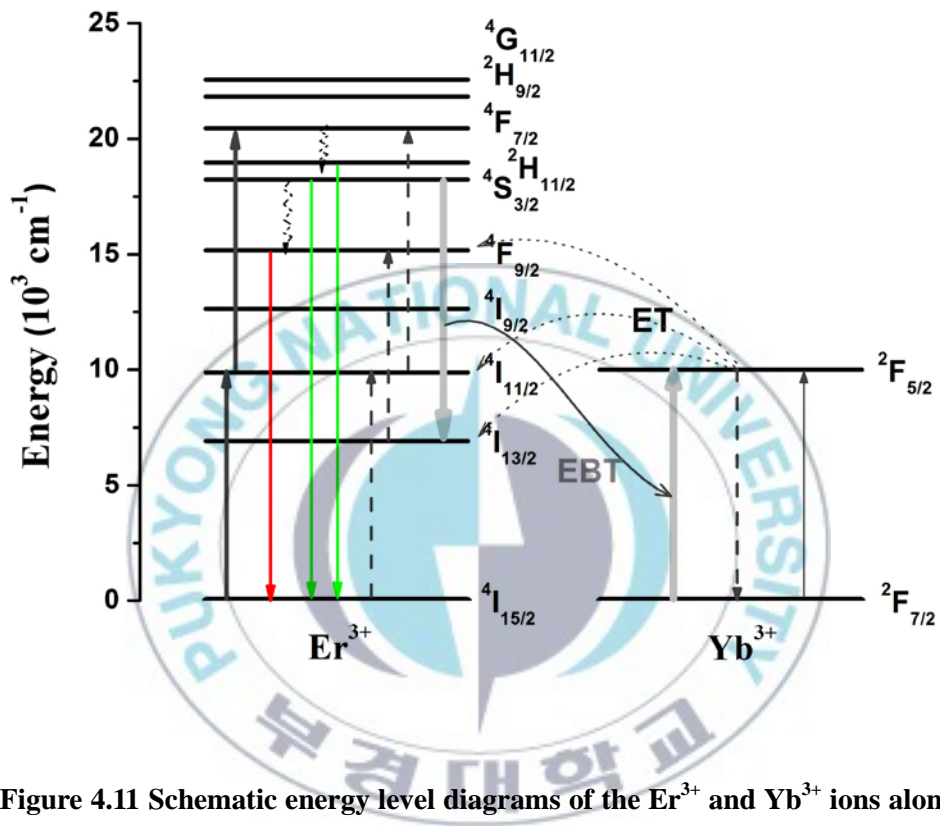


Figure 4.11 Schematic energy level diagrams of the Er^{3+} and Yb^{3+} ions along with the proposed mechanism.

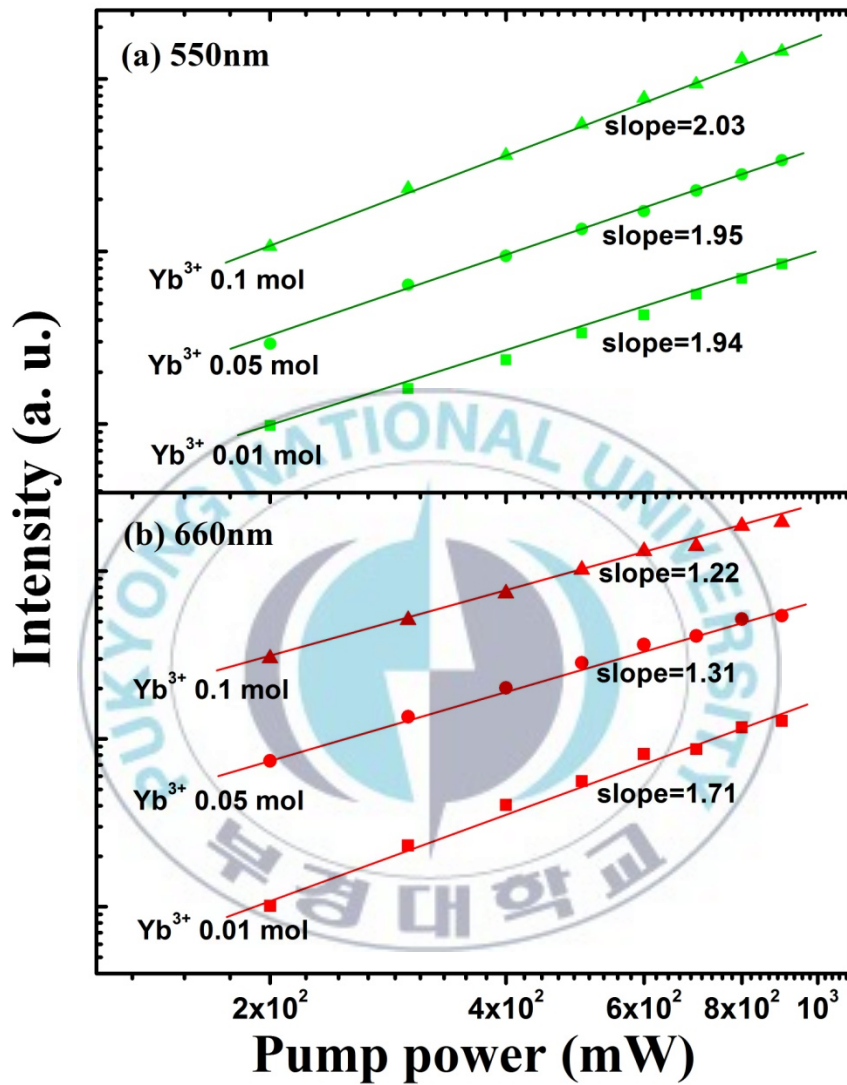


Figure 4.12 Pump power dependence of UC emission band centered at (a) 550 nm and (b) 660 nm.

In summary, $\text{ZrO}_2:\text{Er}^{3+}$ and $\text{ZrO}_2:\text{Er}^{3+}, \text{Yb}^{3+}$ phosphors were synthesized via a solvothermal reaction method. There were two upconverted emission bands: a green emission centered at 550 nm and a red emission centered at 660 nm under excitation by a 975 nm LD. The green transitions from ${}^2\text{H}_{11/2}$ and ${}^4\text{S}_{3/2}$ to the ${}^4\text{I}_{15/2}$ level of Er^{3+} ions come from the ETU process from the Yb^{3+} to the Er^{3+} ions. For high concentrations of Yb^{3+} ions, the red emission state ${}^4\text{F}_{9/2}$ can be populated from the long-lived ${}^4\text{I}_{13/2}$ level by the absorption of one laser photon in an EBT process (${}^4\text{S}_{3/2}:\text{}^4\text{I}_{13/2} \rightarrow \text{}^2\text{F}_{7/2}:\text{}^2\text{F}_{5/2}$). This phenomenon was confirmed by the pump power dependence of green and red upconversion emission intensities: the slopes of pump power dependence were close to 2 and 1, respectively. These results indicated that the concentration of Yb^{3+} ions is an important factor affecting the upconversion emission process and that the EBT process also plays a key role in producing a bright red upconversion emission.

4.3 UC luminescence properties of Ho³⁺ and Yb³⁺ co-doped zirconium oxide

Rare-earth doped infrared (IR) to visible frequency upconversion (UC) nanocrystals have attracted a great scientific interest due to their potential applications in bio-probe, solid-state lasers and three-dimensional display [140-142] and so on. Optical properties of trivalent lanthanide ions such as Er³⁺, Tm³⁺ and Ho³⁺ in glasses, crystals, or glass ceramics have been extensively studied to achieve infrared to visible upconversion photoluminescence (UCPL) [143-146]. The interest in the rare earth doped phosphors is to produce visible emission when pumped with ultraviolet (downconversion) or near infrared NIR (upconversion) light. It is well known that Ho³⁺ is an excellent candidate to produce green and red emission as has been shown recently for different matrix [147-149]. Especially, with the advent of cheaply available and powerful IR laser diodes (LD), there were interested for Ho³⁺/Yb³⁺ UC, taking advantage of Yb³⁺ → Ho³⁺ energy transfer (ET) [135,150].

In this work, ZrO₂:Ho³⁺ and ZrO₂:Ho³⁺, Yb³⁺ nanophosphors were synthesized via a solvothermal reaction method with the following starting materials: ZrO(NO₃)₂·2H₂O (99.9%, Aldrich), Ho(NO₃)₃·5H₂O (99.9%, Aldrich), and Yb(NO₃)₃·5H₂O (99.9%, Aldrich). Firstly, the starting materials were dissolved in 20 ml of 2-propanol according to Zr_{1-x-y}Ho_xYb_yO₂ (x = 0.01 mol; y = 0, 0.01, 0.05, 0.1 mol). The starting materials were used without any further purification and stirred vigorously by using a magnetic stirrer until a

homogeneous solution formed, which was then transferred into a stainless steel autoclave with a Teflon liner. It was then reacted at 250 °C and maintained for 20 h with magnetic stirring to make a stable network. After cooling gradually down to room temperature and then being dried for a day, the powder samples were sintered in air at 1000 °C for 2 h.

The crystal structure and phase of the synthesized samples were characterized by X-ray diffraction (XRD) using a Philips X'Pert/MPD diffraction system with CuK₁ radiation ($\lambda = 1.54056 \text{ \AA}$). The morphology of samples was examined by scanning electron microscopy (SEM, HITECHI S-4200 FESEM). The mean particle size of the ZrO₂ nanophosphors were calculated from the width of the XRD peaks using Scherrer's equation. The energy dispersive X-ray spectroscopy (EDX) is an analytical technique used for the elemental analysis of a sample. The upconversion emission spectrum was measured at room temperature by exciting the erbium ions using a 975 nm LD and using a photomultiplier tube to detect the signal, which was amplified by a standard lock-in technique. The maximum laser power was about 1 W, but a power of 600 mW was chosen for stable operation.

The XRD patterns of ZrO₂:Ho³⁺ and different concentrations (0, 1, 3, 5, 7 and 10 mol%) of Yb³⁺ co-doped ZrO₂:Ho³⁺ sintered at 1000 °C are shown in Fig. 4.13. The diffraction patterns for 0, 1 mol% Yb³⁺ doped samples were dominated monoclinic phase. As the concentrations of Yb³⁺ ions increases to 3 mol%, the ZrO₂:Ho³⁺, Yb³⁺ nanophosphors have a mixture of monoclinic and tetragonal phase and more 5 mol% Yb³⁺ has a very stable tetragonal phase. This confirms

that the dopant concentration influences the stability of the tetragonal phase, as was previously reported [135].

Fig. 4.14 shows the SEM image and EDX for $\text{ZrO}_2\text{:Ho}^{3+}$, 5 mol% Yb^{3+} sample. As shown in Fig. 4.14, the particle size is up to 80 nm and the shape showed uniform round types. EDX was used to examine the elemental composition of the $\text{ZrO}_2\text{:Ho}^{3+}$, Yb^{3+} powders. It confirmed the presence of zirconium (Zr), oxygen (O), holmium (Ho) and ytterbium (Yb) in the $\text{ZrO}_2\text{:Ho}^{3+}$, Yb^{3+} powders and the Yb^{3+} concentration in the $\text{ZrO}_2\text{:Ho}^{3+}$, Yb^{3+} were determined to be 0.92, 4.87%. As shown in Fig. 4.13, the $\text{ZrO}_2\text{:Ho}^{3+}$, Yb^{3+} powders did not determine the other component.

Fig. 4.15 presents the UC emission spectra of 1 mol% Ho^{3+} and various Yb^{3+} concentration (0, 1, 3, 5, 7 and 10 mol%) under 975 nm LD, matching perfectly the Yb^{3+} absorption band. Three emission bands were observed, and according to the energy diagram of the Ho^{3+} ion, the anti-Stokes emission corresponds to 4f–4f transitions. The strong green band (550 nm) was attributed to the $^5\text{F}_4/^5\text{S}_2 \rightarrow ^5\text{I}_8$ transition and very weak red (660 nm) and near infrared (NIR) (757 nm) bands were attributed to the $^5\text{F}_5 \rightarrow ^5\text{I}_8$, $^5\text{S}_2 \rightarrow ^5\text{I}_7$ transition, respectively.

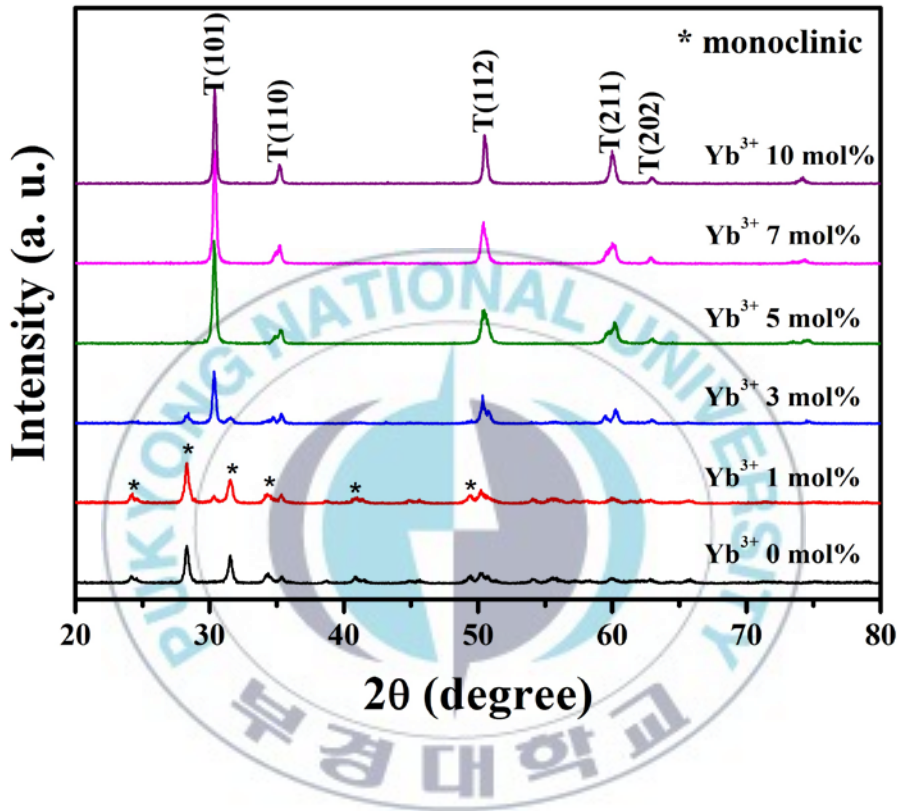


Figure 4.13 XRD patterns of $\text{ZrO}_2:\text{Ho}^{3+}$ and different concentrations of Yb^{3+} co-doped $\text{ZrO}_2:\text{Ho}^{3+}$ sintered at 1000°C .

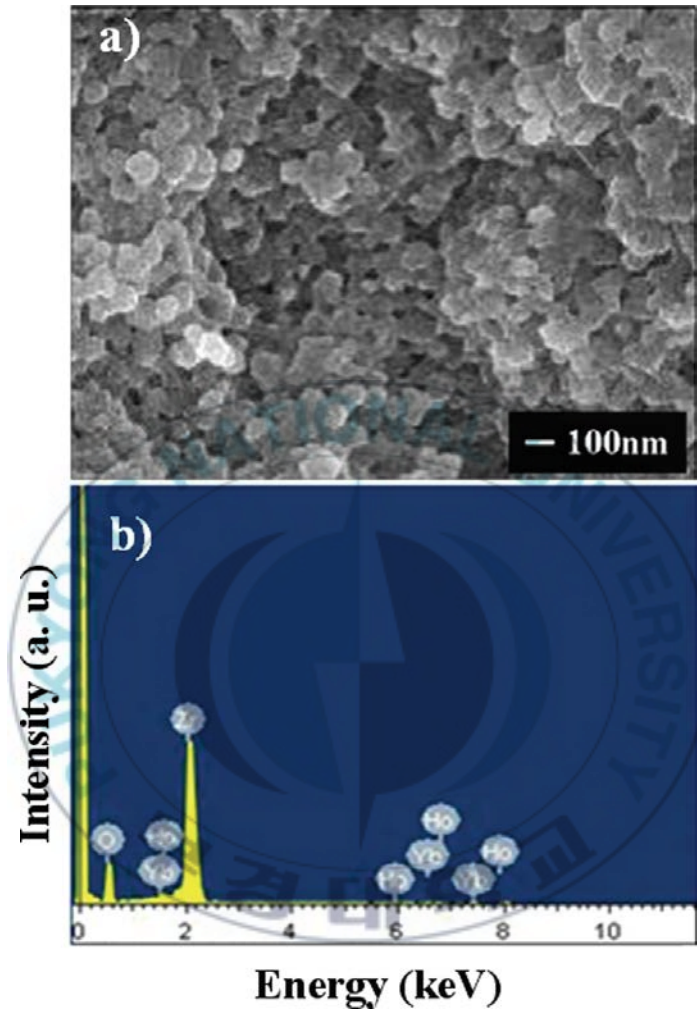


Figure 4.14 (a) SEM image and (b) energy-dispersive X-ray (EDX) spectroscopy of $\text{ZrO}_2:\text{Ho}^{3+}, \text{Yb}^{3+}$ sample.

Fig. 4.16 shows the UC emission intensity behavior according to the energy transfer state as a function of Yb^{3+} concentration. As shown in Fig. 4.16, both the green and NIR UC emissions increase with Yb^{3+} concentration from 0 to 7 mol%, but then showed a decrease for further increases in Yb^{3+} ion concentration above 7 mol%. The energy transfer of the green and NIR UC emissions with Yb^{3+} concentrations arises from the fact that both emissions are emitted from the same upper $^5\text{F}_4/^5\text{S}_2$ state. On the other hand, the red UC emission at 660 nm continuously increased as the concentration of Yb^{3+} ions was increased from 0 to 10 mol%. We can consider the energy transfer takes place in a different path rather than a transition from the $^5\text{F}_4/^5\text{S}_2$ state.

To identify the detailed UC mechanism, the pump power dependence of UC emissions was investigated. Fig. 4.17 shows that the pump power dependence of 550 and 660 nm UC emissions of 1 mol% Ho^{3+} /7 mol% Yb^{3+} co-doped ZrO_2 . The UC emission intensities at 550 and 660 nm have been found to be fitted to the slopes of 1.88 and 1.83, respectively. These values indicate the presence of two photon absorption mechanism involved. The visible emission by UC mechanism is result of the energy transfer from Yb^{3+} (donor) to the Ho^{3+} (acceptor) promoting electrons from the ground state to different excited states. The proposed UC mechanism considers the absorption in Fig. 4.18. The initial 975 nm photon will populate the $^2\text{F}_{5/2}$ level of the Yb^{3+} ion, which will then transfer its energy to a nearby Ho^{3+} ion thus populating the $^5\text{I}_6$ level. The difference in energy between the two states will be dissipated by vibration of the lattice.

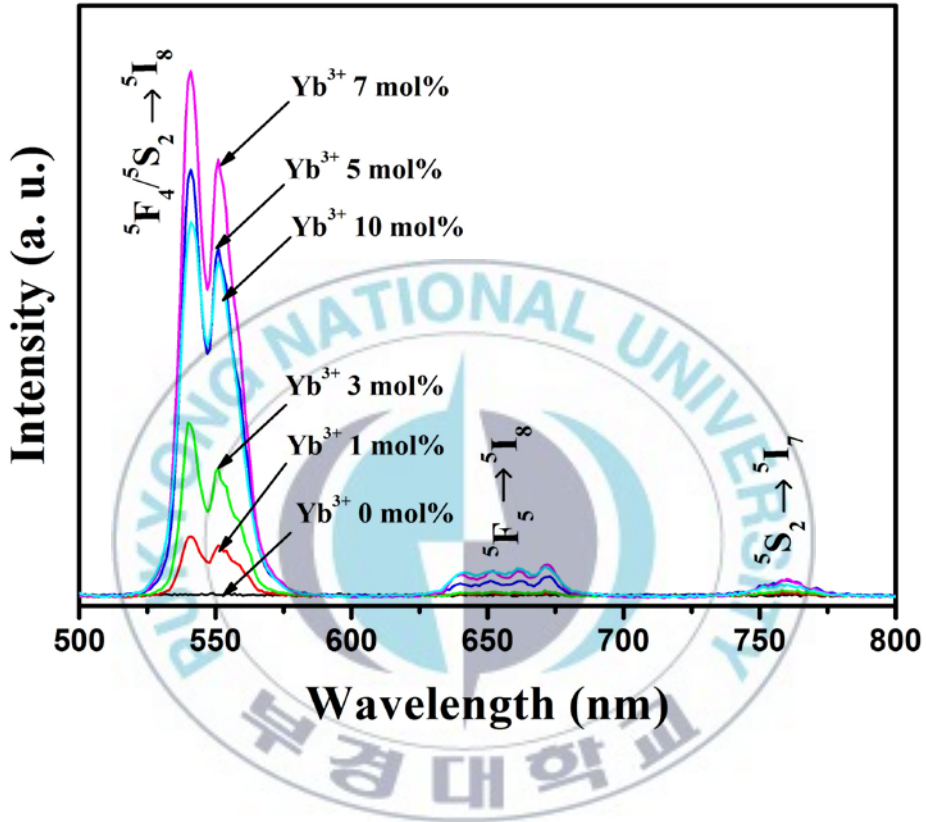


Figure 4.15 UC emission spectra of 1 mol% Ho^{3+} and various Yb^{3+} concentrations under 975 nm LD.

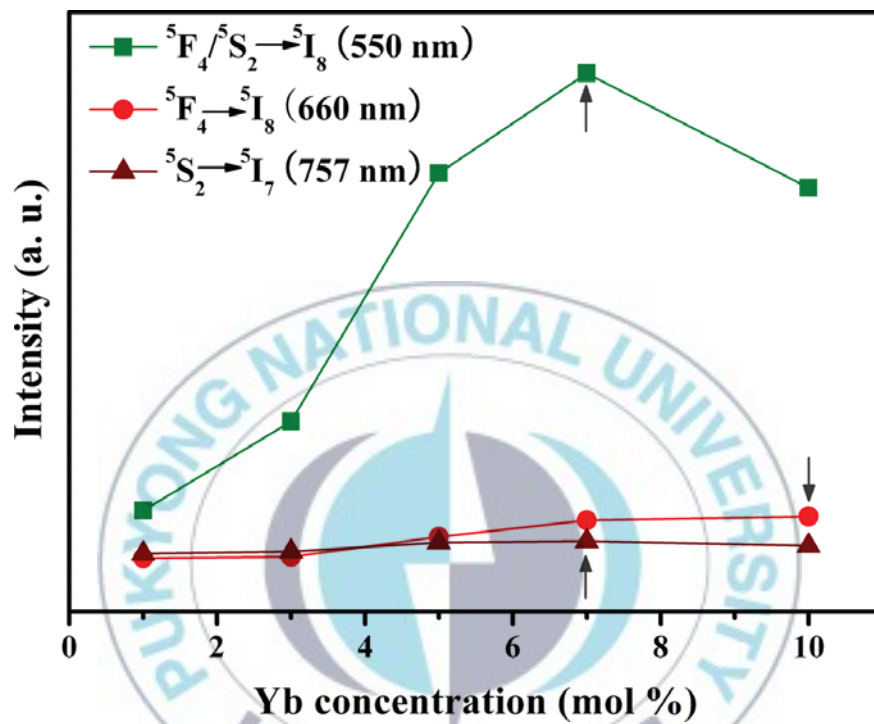


Figure 4.16 UC emissions peaked at 550, 660 and 757 nm with the increase of Yb^{3+} concentrations.

The population in the 5I_6 level is promoted to the ${}^5F_4/{}^5S_2$ level either through another energy transfer (ET) from Yb^{3+} ion in the ${}^2F_{5/2}$ state or excites state absorption (ESA) via the absorption of 975 nm pump photon. When the ${}^5F_4/{}^5S_2$ level is populated, the major part of excited electrons relaxes to the ground state producing the strong green emissions. And part of excited electrons can non-radiative decay a by multi-phonon relaxation to the 5F_5 and 5I_4 states that in turn decay to the ground state producing the weak red and NIR emission, respectively. However, the multiphonon relaxation rate from 5S_2 to the 5F_5 level is very low, because the energy gap between the 5S_2 and 5F_5 levels is about $3,300\text{ cm}^{-1}$, which is larger by a factor of 7 than the phonon energy of ZrO_2 (470 cm^{-1}).

The multi-phonon relaxation rate is dependent of the energy gap between neighbor states and highest optical phonon energy of samples. If the energy gap is larger than five phonon energies, multi-phonon relaxation rate can be neglected. Therefore the 5I_7 state is populated either by non-radiative relaxation from the 5I_6 state or by radiative decay from the 5S_2 state. The ${}^5S_2 \rightarrow {}^5I_7$ transition also produces UC emission at 757 nm. The ${}^5S_2 \rightarrow {}^5I_7$ transition is dominant because the green and NIR emission intensities are emitted from the same upper the 5S_2 state, as shown in Fig. 4.18. And then ET from Yb^{3+} ion or ESA takes the Ho^{3+} ion up to the 5F_5 state, which indicates the red emission via the ${}^5F_5 \rightarrow {}^5I_8$ transition.

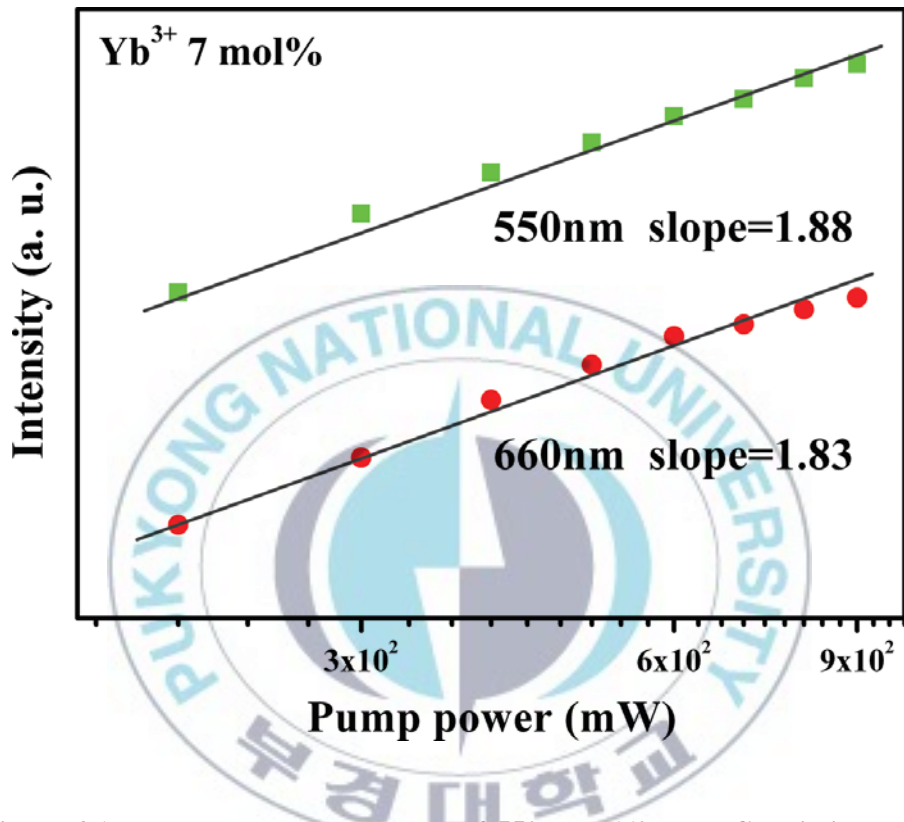


Figure 4.17 Pump power dependence of 550 and 660 nm UC emissions of 1 mol% Ho³⁺/7 mol% Yb³⁺ co-doped ZrO₂.

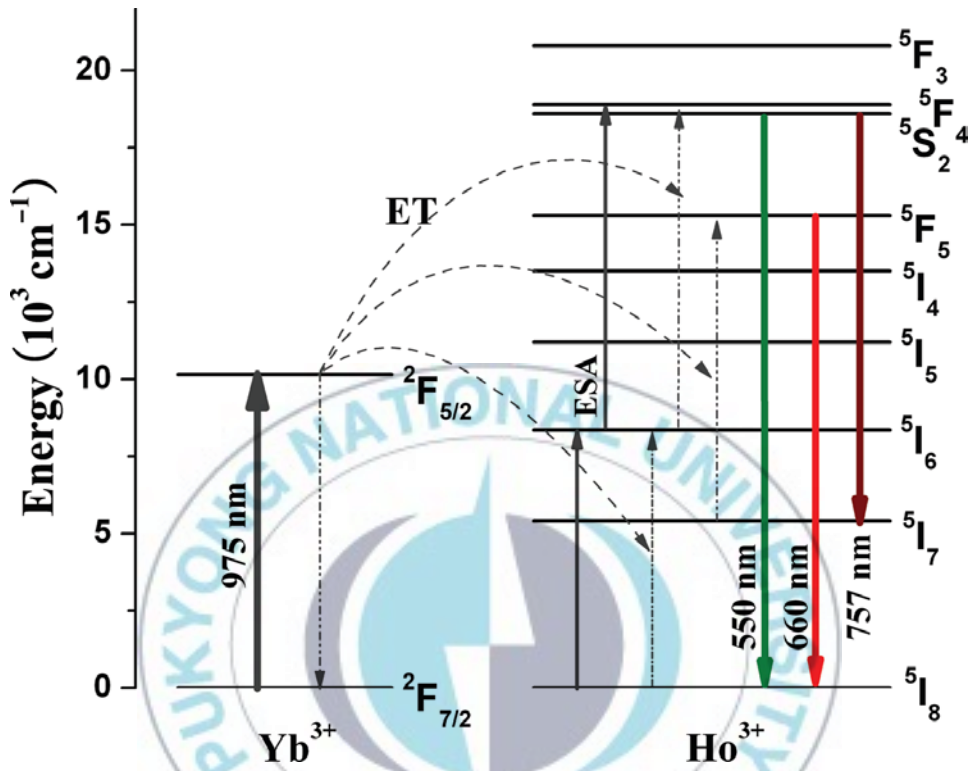
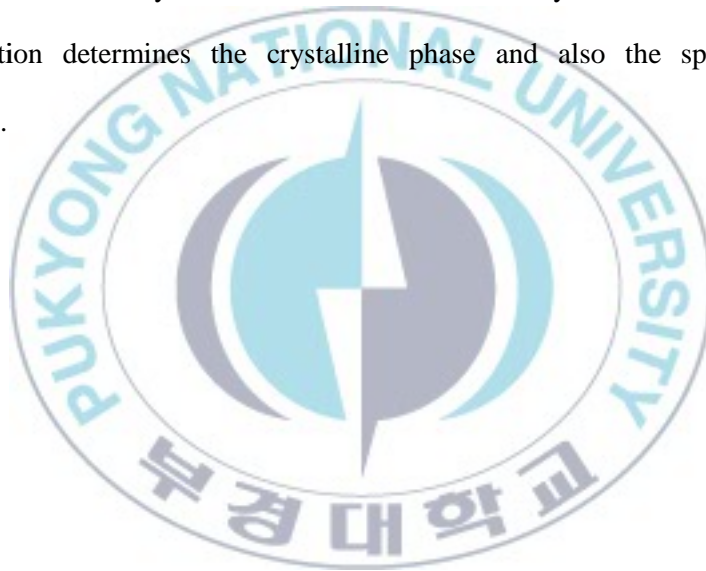


Figure 4.18 Schematic energy level diagrams of Ho^{3+} and Yb^{3+} ions along with the proposed UC mechanism.

In summary, the Yb^{3+} ion concentration dependence of the intensities of visible and NIR UC emissions of Ho^{3+} ions were investigated under a 975 nm laser diode excitation. Intense green, red and NIR UC emissions at 550, 660 and 757 nm can be observed, which are assigned to the transitions of ${}^5\text{F}_4/{}^5\text{S}_2 \rightarrow {}^5\text{I}_8$, ${}^5\text{F}_5 \rightarrow {}^5\text{I}_8$ and ${}^5\text{S}_2 \rightarrow {}^5\text{I}_7$ of Ho^{3+} , respectively. The crystallite size up to 80 nm and then main crystallite phase was the tetragonal structure as the Yb^{3+} concentration is increased. It was shown that the UC mechanism is based on the absorption of two photons either by the ET from Yb^{3+} ion or by ESA. The sensitizer concentration determines the crystalline phase and also the spectroscopic properties.



4.4 Li doping effects on the UC luminescence of Yb³⁺/Er³⁺-doped ABO₄ (A=Ca, Sr; B=W, Mo)

UC materials have been attracted attention as potential solid state lasers or biological fluorescence devices [151-153]. For the solid state hosts for upconversion, most previous attention has been paid to halides, sulfides because of their high upconversion efficiency. However, the application is greatly restricted due to the high production cost or the poor chemical stability. Recently, oxide ceramics or nanopowders with high chemical stability and low phonon energy have been adopted as the candidate host for upconversion materials [154-156]. Tungstate including CaWO₄ and SrWO₄ is a very important family of oxide materials that have various application fields such as a scintillator, optical fibers, electrochemical cells, microwave and photoluminescence [157-159]. And CaMoO₄ and SrMoO₄ have attracted particular interest in a variety of applications such as hosts for lanthanide activated lasers, luminescence materials, microwave applications and catalysts [160,161].

In this work, the powder samples of (A_{0.85-x}Yb_{0.10}Er_{0.05}Li_x)BO₄ were prepared by solid-state reaction method at high temperature, where A is Ca or Sr, and B is W or Mo, and x is 0.000, 0.075, 0.150 and 0.225. The starting materials were calcium carbonate (CaCO₃, 99%, Aldrich), strontium carbonate (SrCO₃, 99.9% Aldrich), molybdenum tri-oxide (MoO₃, 99.9%, Aldrich), tungsten oxide (WO₃, 99.9%, Aldrich), lithium carbonate (Li₂CO₃, 99.9%, Aldrich), ytterbium oxide (Yb₂O₃, 99.9%, Aldrich) and erbium oxide (Er₂O₃,

99.9%, Aldrich). In this work, the concentrations of Er^{3+} and Yb^{3+} were fixed at 0.05 and 0.10 mol respectively for detailed investigation on effects of Li^+ concentration ranging from 0 to 0.225 mol. The starting powders with the designed stoichiometric quantities were ball-milled for 10 h, and then were calcined ranging from 800 to 950 °C for 10 h in air. The calcination temperature was determined. The crystalline phase of calcined powders was identified by X-ray power diffraction (XRD, X'Pert-MPD system, Philips). A 975 nm laser diode was used as the pumping source to get the luminescence spectra. The maximum laser power was about 1W, but for stable operation a power of 200 mW was chosen. The emitted light was focused into the monochromator and was detected by using a photomultiplier tube. The signal was fed to a digital oscilloscope.

Fig. 4.19 shows the XRD patterns of ABO_4 ($A = \text{Ca}, \text{Sr}; B = \text{W}, \text{Mo}$) phosphors doped with 0.05 mol of Er^{3+} , 0.10 mol of Yb^{3+} and tri-doped with different concentrations of Li^+ ion calcined at 800 ~ 950 °C for 10 h. The diffraction patterns of the products can be indexed with a pure tetragonal phase (space group: $I4_1/a$), which is mostly consistent with the standard data of scheelite structured CaWO_4 (JCPDS card no. 41-1431), CaMoO_4 (JCPDS card no. 07-0212), SrWO_4 (JCPDS card no. 08-0490), SrMoO_4 (JCPDS card no. 08-0482) respectively. And no secondary phases could be identified with the variation of Li^+ concentration. It is suggested that all the obtained samples are single-phase scheelite structure and cannot be changed the crystal phase of ABO_4 by introducing Li^+ ions ranging from 0 to 0.225 mol. The highest intensity peaks around 27-29° (2θ) are attributed to the reflection of (1 1 2) plane.

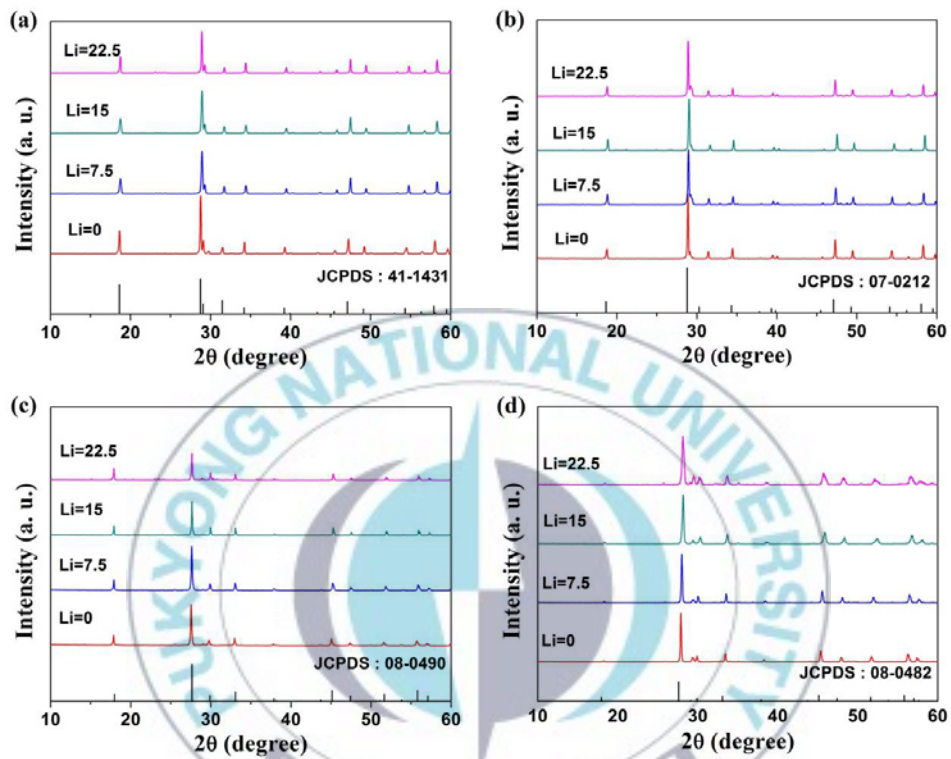


Figure 4.19 XRD patterns of (a) CaWO_4 , (b) CaMoO_4 , (c) SrWO_4 , and (d) SrMoO_4 tri-doped with 5 mol% of Er^{3+} , 10 mol% of Yb^{3+} and different concentration of Li^+ ions.

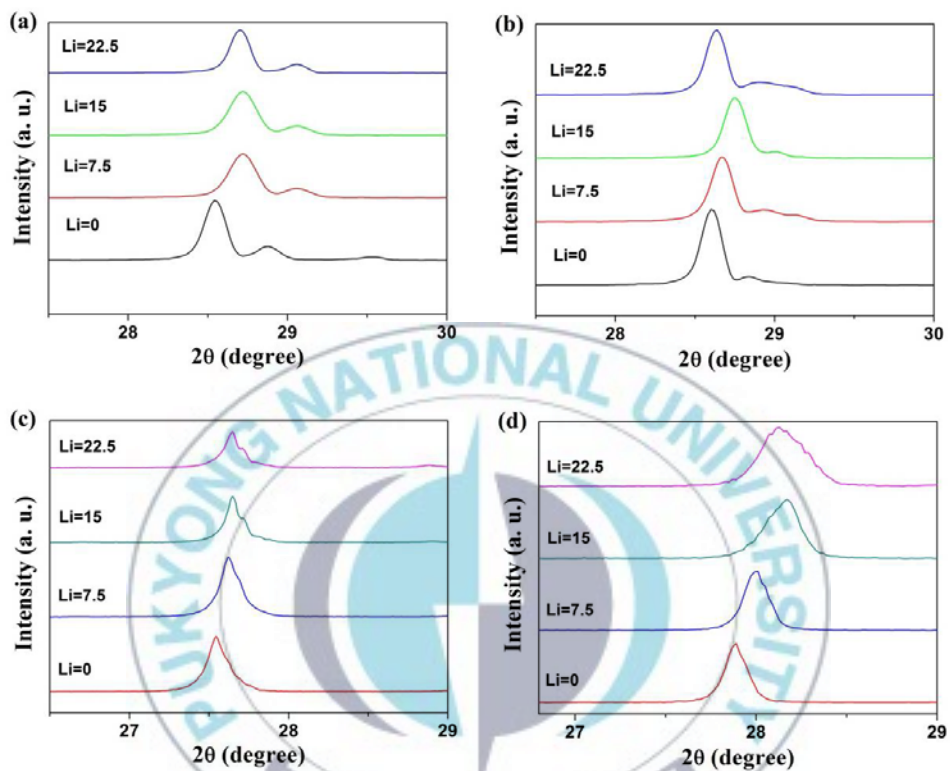


Figure 4.20 Enlarged XRD patterns near 27-29° (2θ) for (1 1 2) main peak of (a) $\text{CaWO}_4:\text{Er}^{3+}/\text{Yb}^{3+}$, (b) $\text{CaMoO}_4:\text{Er}^{3+}/\text{Yb}^{3+}$, (c) $\text{SrWO}_4:\text{Er}^{3+}/\text{Yb}^{3+}$ and (d) $\text{SrMoO}_4:\text{Er}^{3+}/\text{Yb}^{3+}$ doped with different concentration of Li^+ ions.

As can be seen in Fig. 4.20, these main diffraction peaks shift to higher angles for Li^+ ion concentration up to 0.15 mol, suggesting the decrease of the lattice constants by Li^+ ions doping.

When the concentration of Li^+ ions was 22.5 mol%, which exceeds the optimum concentration for charge compensation, the angles of the peaks were reduced. The charge discrepancy of Ca^{2+} with Er^{3+} and Yb^{3+} ions could be compensated by Li^+ co-doping. The molar ratio of the cations was as follows: $(0.85-x)\text{Ca}^{2+} + 0.10\text{Yb}^{3+} + 0.05\text{Er}^{3+} + x\text{Li}^+ + \text{W}^{6+}$. Base on this formula, we can get the optimum charge compensation condition when the concentration of Li^+ ion (x) is 0.150. Substituting the $\text{Ca}^{2+}/\text{Sr}^{2+}$ ions by the smaller sized Li^+ ions would cause the change of the lattice constants. The lattice constant decreases with the increasing Li^+ concentration because of the smaller ionic radius of Li^+ [0.92 Å, coordination number(CN)=8] compared with $\text{Ca}^{2+}/\text{Sr}^{2+}$ [1.12 Å, CN=8/1.26 Å, CN=8] [162]. But the (1 1 2) peaks of the samples of x=0.225 are reduced comparing with those of the optimizing samples of x=0.150 that were can be seen in Fig. 4.20. And the lattice parameters of all samples were listed in Table 4.1 It is believed that an excess of Li^+ ions over charge compensation condition of 15mol% can be occupied in the interstitial sites due to its small size, which lead the expansion of host lattice constant.

Fig. 4.21 presents the upconversion emission spectra of $\text{ABO}_4:\text{Er}^{3+}/\text{Yb}^{3+}/\text{Li}^+$ phosphors under the 975 nm laser diode excitation for different concentrations of Li^+ .

Table 4.1 Lattice constants of ABO₄ (A = Ca, Sr; B = W, Mo) phosphors tri-doped with 5 mol% of Er³⁺, 10 mol% of Yb³⁺ and different concentration of Li⁺ ions.

Li ⁺ (mol%)	CaWO ₄		CaMoO ₄		SrWO ₄		SrMoO ₄	
	a=b	c	a=b	c	a=b	c	a=b	c
JCPDS	5.2429	11.3730	5.2260	11.4300	5.4168	11.9510	5.3944	12.0200
0	5.2468	11.2687	5.2138	11.3947	5.3854	11.9638	5.3708	11.9799
7.5	5.2179	11.1985	5.2019	11.3871	5.3743	11.9144	5.3621	11.9313
15	5.1937	11.1770	5.1765	11.3580	5.3719	11.8771	5.3283	11.8347
22.5	5.2175	11.2295	5.2111	11.3878	5.3792	12.1779	5.3390	11.8634

All the phosphor exhibit the strong green emissions (530 and 550 nm) and weak red emission (between 650 and 679 nm) from the intra-4f electronic transition $^2H_{11/2}/^4S_{3/2} \rightarrow ^4I_{15/2}$ and $^4F_{9/2} \rightarrow ^4I_{15/2}$ transitions of the Er³⁺ ions, respectively. By introducing Li⁺ ion the position of emission peaks does not varies, but the intensity of UCPL changes significantly. The insets of Fig. 4.21 show the green emission intensities emitted from the ABO₄ (A = Ca, Sr; B = W, Mo) phosphors as function of the concentrations of Li⁺ ion. Up to 15 mol% of Li⁺ concentration which satisfied the charge compensation condition, the UC luminescence intensities were increased. The intensities of UCPL emitted from CaBO₄ (B = W, Mo) phosphors doped with 15 mol% of Li⁺ enhanced about 2~3 times higher than those of Li⁺ un-doped phosphors. And the UCPL intensities of SrBO₄ (B = W, Mo) phosphors doped with 15 mol% of Li⁺ increased about 4~10 times. The UCPL intensities emitted from the samples of 22.5 mol% are lower than those of 15 mol% samples.

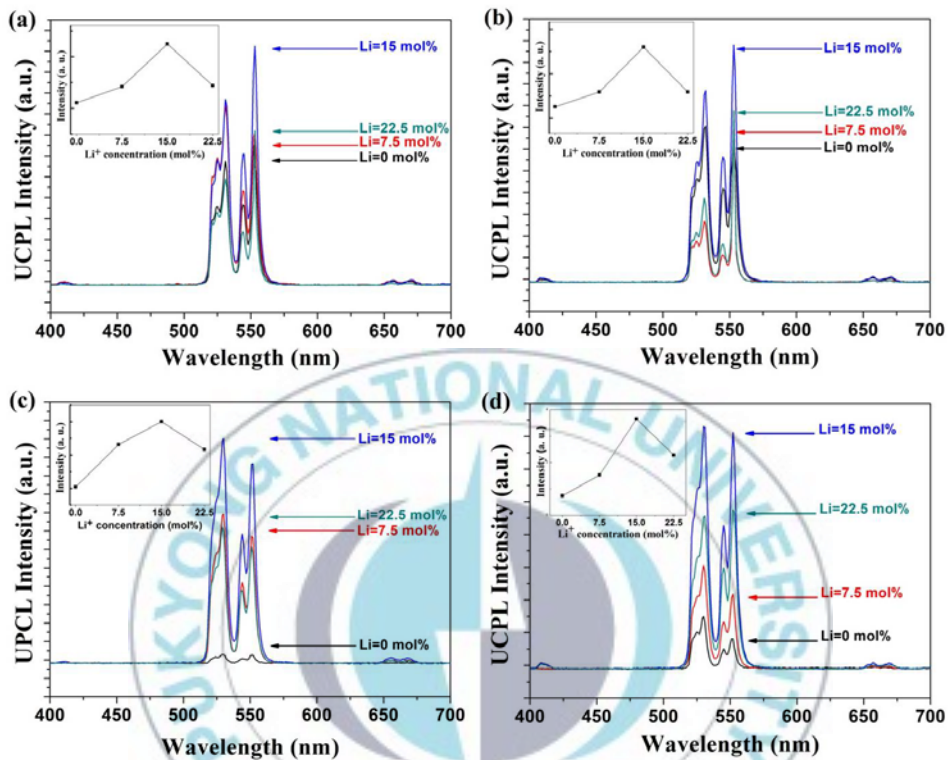


Figure 4.21 UC luminescence spectra of (a) $\text{CaWO}_4:\text{Er}^{3+}/\text{Yb}^{3+}$, (b) $\text{CaMoO}_4:\text{Er}^{3+}/\text{Yb}^{3+}$, (c) $\text{SrWO}_4:\text{Er}^{3+}/\text{Yb}^{3+}$ and (d) $\text{SrMoO}_4:\text{Er}^{3+}/\text{Yb}^{3+}$ doped with different concentration of Li^+ ; the insert shows the enhancement factor of green UC emission as a function of the Li^+ concentration.

The UCPL mechanism in Er^{3+} and Yb^{3+} co-doped systems are presented schematically in Fig. 4.22. First, the Er^{3+} ion is excited from the ground state $^4\text{I}_{15/2}$ to the excited state $^4\text{I}_{11/2}$. Subsequent multi-phonon non-radiative relaxations of $^4\text{I}_{11/2} \rightarrow ^4\text{I}_{13/2}$ also populate the $^4\text{I}_{13/2}$ level. From the second-step excitation, the excited-state ions are excited from the $^4\text{I}_{11/2}$ to the $^4\text{F}_{7/2}$ states or from the $^4\text{I}_{13/2}$ to $^4\text{F}_{9/2}$ states. The populated $^4\text{F}_{7/2}$ may mostly non-radiative relax to $^2\text{H}_{11/2}$ and $^4\text{S}_{3/2}$ states, which produce green UCPL. The populated $^4\text{F}_{9/2}$ level causes red UC emissions. The multi-phonon relaxation rate is dependent of the energy gap (ΔE) between neighbor states and highest optical phonon energy of samples ($h\nu$). If the energy gap is larger than four phonon energies, multi-phonon relaxation rate can be neglected. The energy gap between $^4\text{I}_{13/2}$ and $^4\text{I}_{11/2}$ (3670 cm^{-1}) is larger by a factor of 4 than the phonon energies of the ABO_4 ($A = \text{Ca, Sr}$; $B = \text{W, Mo}$) phosphors ranging $880 \sim 930 \text{ cm}^{-1}$ [163-165]. However the lifetime of $^4\text{I}_{13/2}$ level is long, this level nearly can be populated from to the low multi-phonon relaxation rate of $^4\text{I}_{11/2} \rightarrow ^4\text{I}_{13/2}$. This is the reason that red UCPL is very weak intensity under the excitation of 975 nm LD.

Fig. 4.23 shows the pump power dependence of green and red upconversion emission intensities, the UCPL intensity was measured as the function of the pump power P . The number of photons required to populate the upper emission state can be obtained by a relation of $I \propto P^n$, where n value is the number of pump photons to produce UC emission. The plots of $\log I$ versus $\log P$ for the green and red emission of the ABO_4 ($A = \text{Ca, Sr}$; $B = \text{W, Mo}$): $\text{Er}^{3+}/\text{Yb}^{3+}$ phosphor doped with 15 mol% Li^+ ion were drawn in Fig. 4.22. The n values of green

emission are 1.88 at lower pumping energy and 1.36 at higher energy side in Fig. 4.23(a), which indicates that the green emission is due to a two-photon process. And in the high-power limit, it is well known that the n value is reduced to unity ($n=1$) [166], and this tendency can be seen at all of slopes in Fig. 4.23. The slopes for the red UCPL emitted from ABO_4 ($A = Ca, Sr; B = W, Mo$): $Er^{3+}/Yb^{3+}/Li^+$ phosphor were about unity as can be seen in the figures. The population of $^4I_{13/2}$ state can be reduced by a transition to ground state and this state jump to red emission state of $^4F_{9/2}$ by absorbing an incident photon. Since $^4I_{13/2}$ state is a meta-stable state, the upconversion process is more active than the decay to ground state. If the red UCPL is attributed to the route of $^4I_{13/2}$ state, the n value of red UCPL must be a unity.

The population processes for the green and red UCPL in ABO_4 ($A = Ca, Sr; B = W, Mo$): Er^{3+}/Yb^{3+} phosphor system were illustrated in Fig. 4.22. Two main UC emission mechanisms are the ESA and the ETU process. The ETU is sensitive to the distance between optical active ions, but the ESA process is independent to the distance. In the ABO_4 ($A = Ca, Sr; B = W, Mo$) phosphors doped with 5 mol% of Er^{3+} , 10 mol% of Yb^{3+} , the average distance between optical active ions is fixed. However, by introducing Li^+ ion into these samples, the lattice constant of the samples will be changed. Consequently, the variation of the distance between active ions affects the rate of ETU. And it is well known that the doping of Li^+ ion can be distorted the local crystal field of the rare-earth ions due to the capability to intermix their f states with higher electronic configurations [167-168].

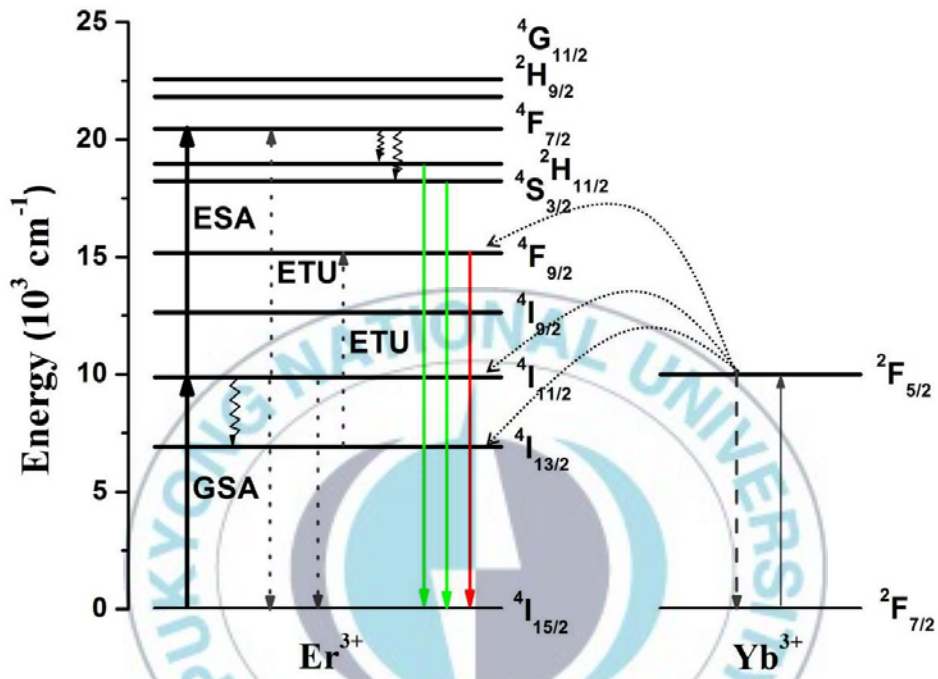


Figure 4.22 Energy level diagrams of Er^{3+} and Yb^{3+} ion.

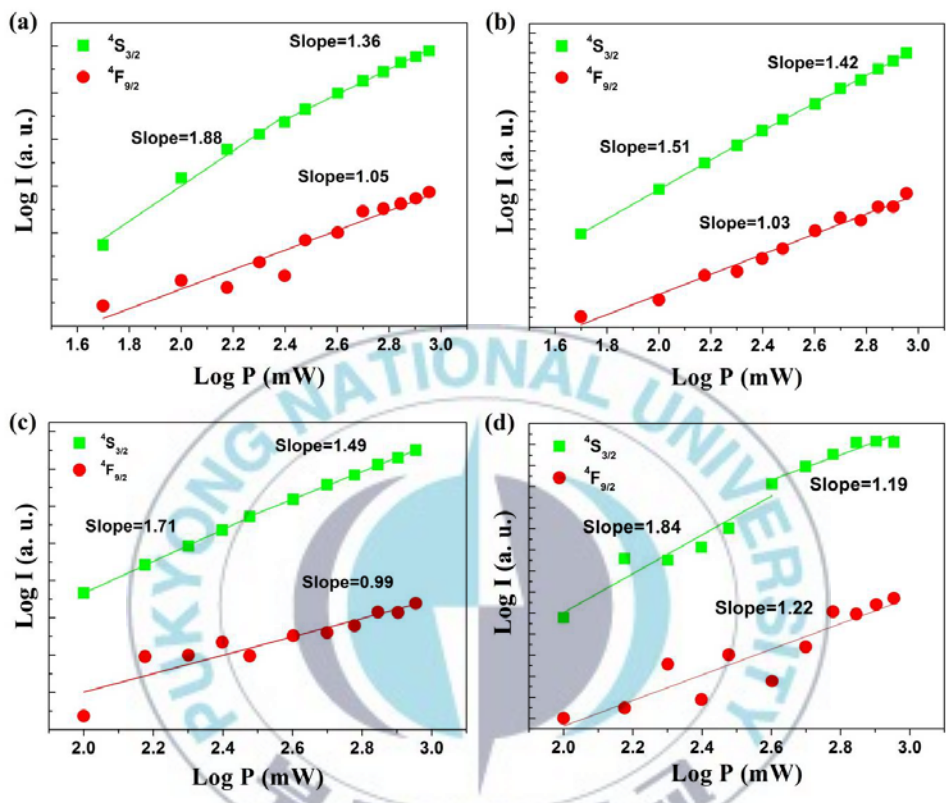
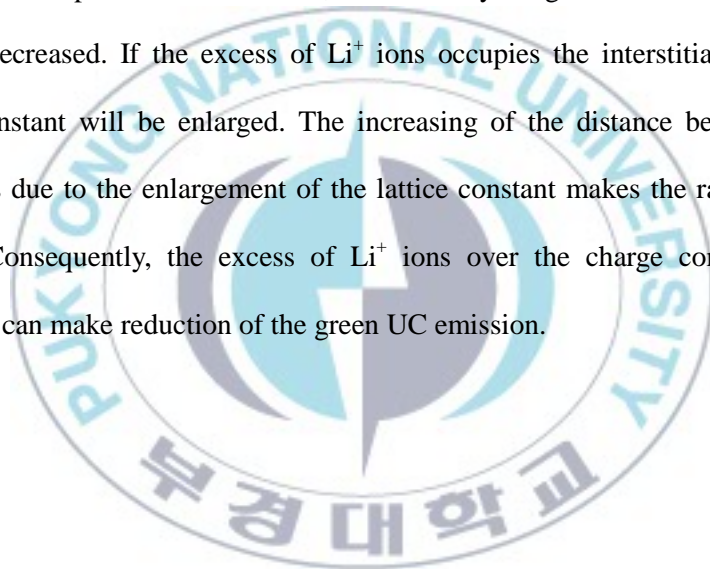


Figure 4.23 Pump power dependence of the green and red UC luminescence of (a) $\text{CaWO}_4:\text{Er}^{3+}/\text{Yb}^{3+}$, (b) $\text{CaMoO}_4:\text{Er}^{3+}/\text{Yb}^{3+}$, (c) $\text{SrWO}_4:\text{Er}^{3+}/\text{Yb}^{3+}$ and (d) $\text{SrMoO}_4:\text{Er}^{3+}/\text{Yb}^{3+}$ doped with 15 mol% of Li^+ ions.

Fig. 4.24 shows variation of UCPL intensity as function of the concentration of Li^+ ions and of lattice constants for the ABO_4 ($\text{A} = \text{Ca}, \text{Sr}; \text{B} = \text{W}, \text{Mo}$): $\text{Er}^{3+}/\text{Yb}^{3+}$ phosphor doped with Li^+ ion ranging from 0 to 22.5 mol%. As the concentration of Li^+ was increased up to 15 mol%, which satisfies the charge compensation conditions, the intensities of green UC emission of all samples were increased. It is attributed to the reduction of lattice constant and distortion of local crystal field symmetry around RE ion. When the amount of Li^+ exceeds the charge compensation conditions, the intensity of green UC emission was slightly decreased. If the excess of Li^+ ions occupies the interstitial sites, the lattice constant will be enlarged. The increasing of the distance between rare earth ions due to the enlargement of the lattice constant makes the rate of ETU reduce. Consequently, the excess of Li^+ ions over the charge compensation condition can make reduction of the green UC emission.



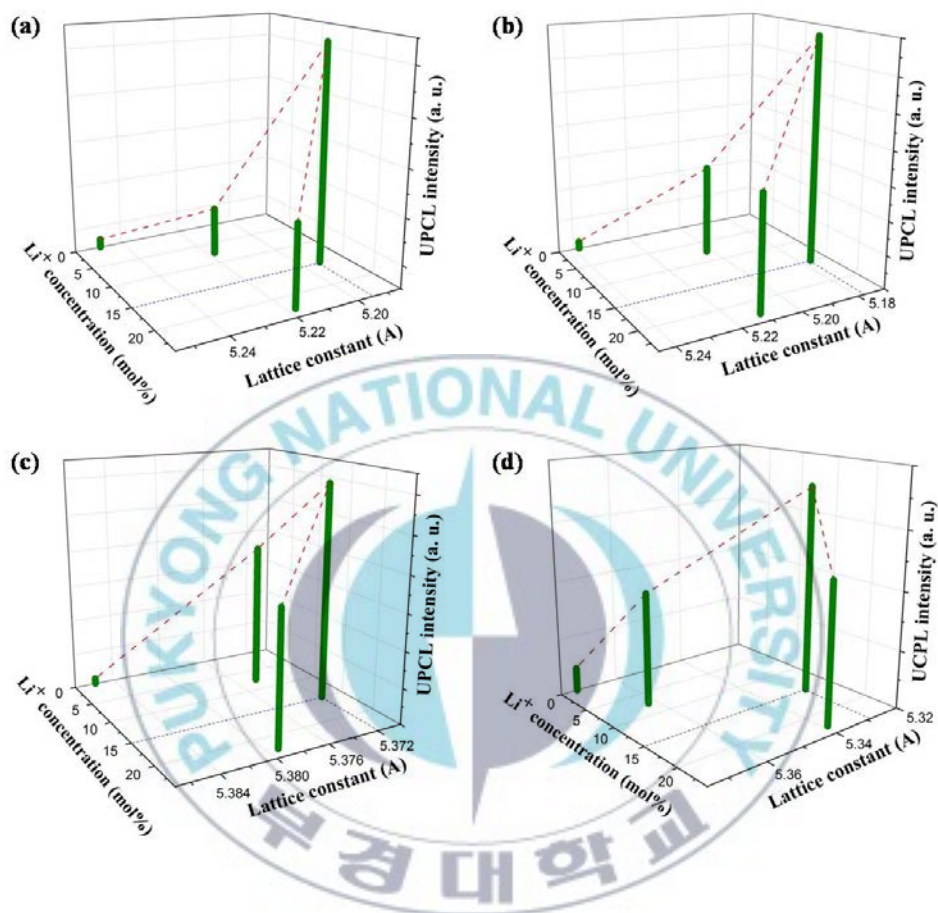
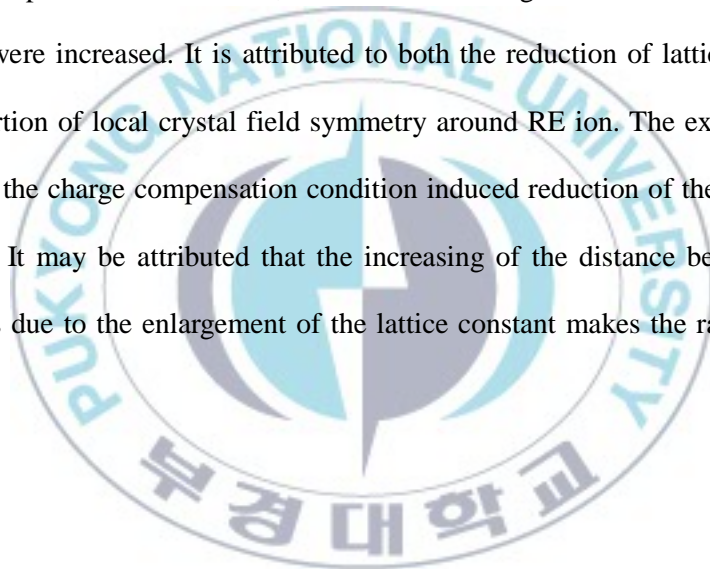


Figure 4.24 The dependence of lattice constant on the UC luminescence intensity of (a) CaWO₄:Er³⁺/Yb³⁺, (b) CaMoO₄:Er³⁺/Yb³⁺, (c) SrWO₄:Er³⁺/Yb³⁺ and (d) SrMoO₄:Er³⁺/Yb³⁺ doped with different concentration of Li⁺ ions.

In summary, ABO_4 ($A = Ca, Sr$; $B = W, Mo$) phosphors doped with 5 mol% of Er^{3+} , 10 mol% of Yb^{3+} and tri-doped with different concentrations of Li^+ ion ranging from 0 to 22.5 mol% were prepared by using a solid-state reaction method. And their upconversion (UC) luminescence properties were investigated under a 975 nm laser-diode excitation. The four kinds of phosphors showed strong green UC emission peaks at 530 and 550 nm and weak red UC emission. As the concentration of Li^+ was increased up to 15 mol%, which satisfies the charge compensation conditions, the intensities of green UC emission of all samples were increased. It is attributed to both the reduction of lattice constant and distortion of local crystal field symmetry around RE ion. The excess of Li^+ ions over the charge compensation condition induced reduction of the green UC emission. It may be attributed that the increasing of the distance between rare earth ions due to the enlargement of the lattice constant makes the rate of ETU reduce.



V. Conclusions

In this work, synthesis and UC luminescence properties of the lanthanide doped oxide phosphors (YAP: Er³⁺, ZrO₂: Er³⁺/Yb³⁺, ZrO₂: Ho³⁺/Yb³⁺ and ABO₄ (A= Ca, Sr; B=W, Mo):Er³⁺/Yb³⁺/Li⁺) have been investigated in detail. The phosphors studied in this work were prepared using high energy ball milling and solvothermal method. The results obtained from these studies are summarized as follows;

1. UC luminescence at different concentrations (0.01, 0.02, 0.03, 0.05 and 0.07 mol) of Er³⁺ doped YAP nanophosphors were synthesized by solvothermal reaction method. In YAP:Er³⁺ nanophosphors, the green transitions of Er³⁺ ions are ESA and ETU. For high concentration of Er³⁺ ions, red emitting state, ⁴F_{9/2}, can be populated from the long-lived ⁴I_{13/2} level by absorption of one laser photon, which follows cross-relaxation process (²H_{11/2} → ⁴I_{9/2}; ⁴I_{15/2} → ⁴I_{13/2}). The pump power dependence of green and red emission changed from quadratic to linear as Er³⁺ ion concentration is increased. The competition between radiation decay and UC of the intermediate state, ⁴I_{13/2}, could explain this anomalous pump power dependence of UCPL.

2. ZrO₂:Er³⁺ and ZrO₂:Er³⁺, Yb³⁺ phosphors were synthesized *via* a solvothermal reaction method. The green transitions from ²H_{11/2} and ⁴S_{3/2} to the ⁴I_{15/2} level of Er³⁺ ions come from the ETU process from the Yb³⁺ to the Er³⁺ ions.

For high concentrations of Yb^{3+} ions, the red emission state ${}^4\text{F}_{9/2}$ can be populated from the long-lived ${}^4\text{I}_{13/2}$ level by the absorption of one laser photon in an EBT process (${}^4\text{S}_{3/2} : {}^4\text{I}_{13/2} \rightarrow {}^2\text{F}_{7/2} : {}^2\text{F}_{5/2}$). This phenomenon was confirmed by the pump power dependence of green and red upconversion emission intensities: the slopes of pump power dependence were close to 2 and 1, respectively. These results indicated that the concentration of Yb^{3+} ions is an important factor affecting the upconversion emission process and that the EBT process also plays a key role in the production of a bright red upconversion emission.

3. The Yb^{3+} ion concentration dependence of the intensities of visible and NIR UC emissions of Ho^{3+} ions were investigated under a 975 nm laser diode excitation. Intense green, red and NIR UC emissions at 550, 660 and 757 nm can be observed, which are assigned to the transitions of ${}^5\text{F}_4/{}^5\text{S}_2 \rightarrow {}^5\text{I}_8$, ${}^5\text{F}_5 \rightarrow {}^5\text{I}_8$ and ${}^5\text{S}_2 \rightarrow {}^5\text{I}_7$ of Ho^{3+} , respectively. The crystallite size was up to 80 nm and then main crystallite phase was the tetragonal structure as the Yb^{3+} concentration is increased. It was shown that the UC mechanism is based on the absorption of two photons either by the ETU from Yb^{3+} ion or by ESA. The sensitizer concentration determines the crystalline phase and also the spectroscopic properties.

4. ABO_4 (A = Ca, Sr; B = W, Mo) phosphors doped with 5 mol% of Er^{3+} , 10 mol% of Yb^{3+} and tri-doped with different concentrations of Li^+ ion ranging from 0 to 22.5 mol% were prepared by using a solid-state reaction method. The four

kinds of phosphors showed strong green UC emission peaks at 530 and 550 nm and weak red UC emission. As the concentration of Li^+ was increased up to 15 mol%, which satisfies the charge compensation conditions, the intensities of green UC emission of all samples were increased. It is attributed to both the reduction of lattice constant and distortion of local crystal field symmetry around RE ion. The excess of Li^+ ions over the charge compensation condition induced reduction of the green UC emission. It might be attributed that the increasing distance between rare earth ions due to the enlargement of the lattice constant retards the rate of ETU.

The experimental results from this thesis would be used for the synthesis of UC phosphors, and it might be extended to numerous other applications. Therefore, it is concluded that lanthanide doped oxide UC phosphors could be one of the promising candidates to meet the requirement for the biomedical application, display and white lighting source for LEDs.

References

- [1] L. H. Li, H. Naoto, X. R. Jun, S. Takayuki, M. Mamoru, *Sci. Techno. Adv. Mater.* **8** (2007) 601.
- [2] R. Kane, H. Sell, "Revolution in lamps: a chronicle of 50 years of progress (2nd ed.)", The Fairmont Press, Inc. 2001.
- [3] F. Auzel, *C. R. Acad. Sci. (Paris)* 263B (1966) 819.
- [4] F. Auzel, *C. R. Acad. Sci. (Paris)* 262 (1966) 1016.
- [5] V. V. Ovsyankin and P. P. Feofilov, *Jetp Lett.* 4 (1966) 317.
- [6] S. Heer, K. Kömpe, H. U. Güdel and M. Haase, *adv. Mater.* 16 (2004) 2102.
- [7] A. Aebischer, S. Heer, D. Biner, K. Krämer, M. Haase and H. U. Güdel, *Chem. Phys. Lett.* 407 (2005) 124.
- [8] M. Pollnau, D. R. Gamelin, S. R. Lüthi, H. U. Güdel and M. P. Hehlen, *Phys. Rev. B* 61 (2000) 3337.
- [9] J. C. Boyer, F. Vetrone, L. A. Cuccia and J. A. Capobianco, *J. Am. Chem. Soc.* 128 (2006) 7444.
- [10] J. J. Owen, A. K. Cheetham, N. A. Nighman, R. H. Jarman and R. J. Thrash, *J. Opt. Soc. Am. B* 11 (1994) 919.
- [11] J. J. Owen, A. K. Cheetham and R. A. McFarlane, *J. Opt. Soc. Am. B* 15 (1998) 684.
- [12] A. Patra, C. S. Friend, R. Kapoor and P. N. Prasad, *J. Phys. Chem. B* 106 (2002) 1909.
- [13] J. A. Capobianco, F. Vetrone, J. C. Boyer, A. Speghini and M. Bettinelli, *Opt.*

Mater. 19 (2002) 259.

[14] A. Patra, C. S. Friend, R. Kapoor and P. N. Prasad, *Chem. Mater.* 15 (2003) 3650.

[15] A. M. Pires, O. A. Serrra, S. Heer and H. U. Güdel, *J. Appl. Phys.* 98 (2005) 063529.

[16] Y. H. Wang and J. Ohwaki, *Appl. Phys. Lett.* 63 (1993) 3268.

[17] X. Zou, and T. Izumitani, *J. Non-Crys. Solids* 162 (1993) 68.

[18] S. Tanabe, S. Yoshii, K. Hirao and N. Soga, *Phys. Rev. B* 45 (1992) 4620.

[19] M. P. Hehlen, N. J. Cockroft, T. R. Gosnell and A. J. Bruce, *Phys. Rev. B* 56 (1997) 9302.

[20] M. E. Koch, A. W. Kueny and W. E. Case, *Appl. Phys. Lett.* 56 (1990) 1083.

[21] R. G. Smart, D. C. Hanna, A. C. Tropper, S. T. Davey, S. F. Carter and D. Szebesta, *American Optics Society*, (1991) Postdeadline Paper CODP13-2.

[22] R. M. Macfarlane, F. Tong, A. J. Silversmith and W. Lenth, *Appl. Phys. Lett.* 52 (1988) 1300.

[23] R. M. Macfarlane, A. J. Silversmith, F. Tong and W. Lenth, "Proceedings of the International Conference on laser Science and Laser Materials" (1988) p.24.

[24] J. Y. Allain, M. Monerie and H. Poignant, *Electron Lett.* 26 (1990) 261.

[25] A. J. Silversmith, W. Lenth and R. M. Macfarlane, *Appl. Phys. Lett.* 51 (1987) 1977.

[26] B. M. Antipenko, S. P. Voronin and T. A. Privalova, *Sov. Phys. Tech. Phys.* 32 (1978) 208.

[27] R. A. McFarlane, *Appl. Phys. Lett.* 54 (1989) 2301.

- [28] T. Hebert, R. Wannernacher, W. Lenth and R. M. Macfarlane, *Appl. Phys. Lett.* 57 (1990) 1727.
- [29] D. C. Nguyen, G. E. Faulkner and M. Dulick, *Appl. Opt.* 28 (1989) 3553.
- [30] J. F. Suijver, in "Luminescence: from theory to applications", ed by C. Ronda, Wiley-VCH Verlag GmbH & Co. KGaA, Weinheim, 2008, pp.134.
- [31] F. Auzel. *Proc. IEEE* 61 758 (1973).
- [32] F. Auzel, *Chem. Rev.* 104 (2004) 139.
- [33] M. F. Joubert, S. Guy and B. Jacquier, *Phys. Rev. B* 48 (1993) 10031.
- [34] M. Pollnau, D. R. Gamelin, S. R. Luthi, H. U. Gudel and M. P. Hehlen, *Phys. Rev. B* 61 (2000) 3337.
- [35] S. Hüfner, "Optical spectra of transparent rare earth component", Academic press New York, San Francisco, London, 1978.
- [36] Alexander A. Kaminskii (ed.), "Laser crystals", Springer series in Optical Science, 14 p12-15.
- [37] G. H. Dieke, in "Spectra and energy levels of rare earth ions in crystals", Wiley Interscience Publishers, New York, 1968.
- [38] M. H. Imanieh, I. R. Martín, B. Eftekhari Yekta, V. K. Marghussian and S. Shakhesi, *Journal of the American Ceramic Society* 95 (2012) 3827.
- [39] M. H. Imanieh, I. R. Martín, J. Gonzalez-Platas, B. Eftekhari Yekta, V. K. Marghussian and S. Shakhesi, *Journal of Nanomaterials* 2014 (2014) 1.
- [40] F. Wang and X. Liu, "Multicolor Tuning of Lanthanide-Doped Nanoparticles by Single Wavelength Excitation". *Accounts of Chemical Research* 2014.

- [41] A. Mendioroz, J. Fernández, M. Voda, M. Al-Saleh, R. Balda and A. J. García-Adeva, *Opt. Lett.* 27 (2002) 1525.
- [42] M. Liu, S. W. Wang, J. Zhang, L. Q. An and L. D. Chen, *Opt. Mater.* 29 (2007) 1352.
- [43] S. Hinojosa, O. Barbosa-Garcia, M. A. Meneses-Nava, J. L. Maldonado, E. D. Rosa-Cruz and G. Ramos-Ortiz, *Opt. Mater.* 27 (2005) 1844.
- [44] M. Medraj, R. Hammond, M. A. Parvez, R.A.L. Drew and W. T. Thompson, *J. Eur. Ceram. Soc.* 26 (2006) 3515.
- [45] I. Warshaw and R. Roy, *J. Am. Ceram. Soc.* 42 (1959) 434.
- [46] S. Mathur, H. Shen, R. Rapalaviciute, A. Kareiva and N. Donia, *J. Mater. Chem.* 14 (2004) 3259.
- [47] J. F. Carvalho, F.S. De Vicente, S. Pairis, P. Odier, A.C. Hernandez and A. Ibanez, *J. Eur. Ceram. Soc.* 29 (2009) 2511.
- [48] V. V. Laguta, M. Niki, A. Vedda, E. Mihokova, J. Rosa and K. Blazek, *Phys. Rev. B* 80 (2009) 045114.
- [49] E. De la Rosa-Cruz, L. A. Diaz-Torres, P. Salas, R. A. Rodríguez, G. A. Kumar, M. A. Meneses, J. F. Mosin˜o, J. M. Hernández and O. Barbosa-García, *J. Appl. Phys.* 94 (2003) 3509.
- [50] L. Chen, Y. Liu and Y. Li, *J. Alloys Compd.* 381 (2004) 266.
- [51] A. Patra, C. S. Friend, R. Kapoor and P. Prasad, *J. Phys. Chem. B* 106 (2002) 1909.
- [52] A. Patra, S. Saha, M. A. R. C. Alentar and N. Harkov, G. Maciel, *Chem. Phys. Lett.* 407 (2005) 477.

- [53] P. Riello, S. Bucella, R. Krsmanovic, S. Meneghetti, S. Pietrantoni and R. Francini, *J. Phys. Chem. B* 109 (2005) 13430.
- [54] E. De la Rosa, P. Salas, H. Desirena, C. Angeles and R. A. Rodriguez, *Appl. Phys. Lett.* 87 (2005) 241912.
- [55] G. De, W. Qin, J. Zhang, J. Zhang, Y. Wang, C. Cao and Y. Cui, *J. Lumin.* 119–120 (2006) 258.
- [56] S. Xu, D. Fang, Z. Zhang and Z. Jiang, *J. Solid State Chem.* 178 (2005) 2159.
- [57] E. De la Rosa-Cruz, L. A. Diaz-Torres, R. A. Rodriguez-Rojas, M. A. Meneses-Nava, O. Barbosa-Garcia and P. Salas, *Appl. Phys. Lett.* 83 (2003) 4903.
- [58] N. Menyuk, K. Dwight, and J. W. Pierce, *Appl. Phys. Lett.* 21 (1972) 159.
- [59] L. A. Di'az-Torres, E. De la Rosa-Cruz, P. Salas and C. Angeles-Chavez, *J. Phys. D: Appl. Phys.* 37 (2004) 2489.
- [60] E. De la Rosa, P. Salas, L. A. Diaz-Torres, A. Martinez and C. Angeles, *J. Nanosci. Nanotech.* 5 (2005) 1480.
- [61] T. Thongtem, A. Phuruangrat and S. Thongtem, *Appl. Surf. Sci.* 254 (2008) 7581.
- [62] J. S. Liao, B. Qiu, H. R. Wen, J. L. Chen and W. X. You, *Mater. Res. Bull.* 44 (2009) 1863.
- [63] Y. G. Su, L. P. Li and G. S. Li, *Chem. Mater.* 20 (2008) 6060.
- [64] X. M. Lou and D. H. Chen, *Mater. Lett.* 62 (2008) 1681.
- [65] V. B. Mikhailik, H. Kraus, G. Miller, M. S. Mykhaylyk and D. Wahl, *J. Appl. Phys.* 97 (2005) 083523.

- [66] L. Cavalcante, J. Sczancoski, R. Tranquilin, M. Joya, P. Pizani, J. Varela and E. Longo, *J. Phys. Chem. Solid* 69 (2008) 2674.
- [67] L. Cavalcante, J. Sczancoski, J. Espinoza, J. Varela, P. Pizani and E. Longo, *J. Alloy Compd.* 474 (2009) 195.
- [68] Y. Yang, X. Li, W. Feng, W. Yang, L. Li, and C. Tao, *J. Alloys Compd.* 509, 845 (2011).
- [69] L. Li, X. Shen, I. Li, X. Feng, *J. Sol-Gel Sci. Technol.* 57, 198 (2011).
- [70] T. K. Anh, P. Benalloul, C. Barthou, L. Giang, N. Vu and L. Minh, *J. Nanomater.* 2007 (2007) 48247.
- [71] D. Matsuura, *Appl. Phys. Lett.* 81 (2002) 4526.
- [72] S. Ivanova and F. Pelle', *Journal of the Optical Society of America B* 26 (2009) 1930.
- [73] N. Yamada, S. Shionoya and T. Kushida, *Journal of the Physical Society of Japan* 32 (1972) 32.
- [74] S. A. Pollack, D. B. Chang, and N. L. Moise, *J. Appl. Phys.* 60 (1986) 4077.
- [75] O. L. Malta, E. Antic-Fidancev, M. Lemaitre-Blaise, J. Dexpert- Ghys, and B. Piriou, *Chem. Phys. Lett.* 129 (1986) 557.
- [76] T. Y. Fan, G. L. Dixon, and R. L. Byer, *Opt. Lett.* 11 (1986) 204.
- [77] E. Cantelar, J. A. Sanz-Garca and F. Cusso, *J. Cryst. Growth* 205 (1999) 5.
- [78] F. Lahoz, I. R. Martl' and A. Briones, *J. Appl. Phys.* 95 (2004) 2957.
- [79] X. Y. Huang and G. F. Wang, *J. Lumin.* 130 (2010) 1702.
- [80] L. Zhaolin, Y. Aishui and J. Y. Lee, *J. Power Source* 74 (1997) 288.
- [81] M. N. Obrocal, O. Mao and J. R. Dahn, *Solid State Ionics* 9 (1998) 112.

- [82] H. Chen, J. M. Wang, T. Pan, H. M. Xiao, J. Q. Zhang and C. N. Cao, *Int. J. Hydrogen Energy* 28 (2003) 199.
- [83] M. M. Oliveira, D. C. Schnitzler and, A. J. G. Zarbin, *Chemistry of Materials* 15 (2003) 1903.
- [84] M. Andersson, L. Österlund, S. Ljungström and A. Palmqvist, *The Journal of Physical Chemistry B* 106 (2002) 10674.
- [85] R. C. Xie and J. K. Shang, *Journal of Materials Science* 42 (2007) 6583.
- [86] M. Choucair, P. Thordarson and J. A. Stride, *Nature Nanotechnology* 4 (2008) 30.
- [87] G. Hu, D. Ma, M. Cheng, L. Liu and X. Bao, *Chemical Communications* 17 (2002) 1948.
- [88] W. Kongsuebchart, P. Prasertdam, J. Panpranot, A. Sirisuk, P. Supphasirongjaroen, and C. Satayaprasert, *J. Cryst. Growth* 297 (2006) 234.
- [89] M. Kus, W. Gernjak, P. Fernández Ibáñez, S. M. Rodríguez, J. B. Gálvez and S. Icli, *Journal of Solar Energy Engineering* 128 (2006) 331.
- [90] Y. W. Cheng, Raphael C. Y. Chan and P. K. Wong, *Water Research* 41 (2007) 842.
- [91] P. Amezagamadrid, R. Silveyramorales, L. Cordobafierro, G. Nevarezmoorillon, M. Mikiyoshida, E. Orrantiaborunda and F. Solis, *Journal of Photochemistry and Photobiology B: Biology* 70 (2003) 45.
- [92] S. Josset, J. Taranto, N. Keller, V. Keller, M. Lett, M. Ledoux, V. Bonnet and S. Rougeau, *Catalysis Today* 129 (2007) 215.

- [93] D. Mitoraj, A. Jańczyk, M. Strus, H. Kisch, G. Stochel, P. B. Heczko and W. Macyk, *Photochemical & Photobiological Sciences* 6 (2007) 642.
- [94] S. Yurdakal, V. Loddo, V. Augugliaro, H. Berber, G. Palmisano and L. Palmisano, *Catalysis Today* 129 (2007) 9.
- [95] H. Park, C. D. Vecitis, W. Choi, O. Weres and M. R. Hoffmann, *Journal of Physical Chemistry C* 112 (2008) 885.
- [96] J. Wang and D. J. Simkin, *Phys. Rev. B* 52 (1995) 3309.
- [97] H. Xu and Z. Jiang, *Chem. Phys.* 287 (2003) 155.
- [98] N. Zu, H. Yang, and Z. Dai, *Phys. B* 403 (2008) 174.
- [99] R. Francini, S. Pietrantonio, M. Zambelli, A. Speghini, and M. Bettinelli, *J. Alloys and Comp.* 380 (2004) 34.
- [100] A. Brenier and A. M. Jurdyc, *J. Lumin.* 69 (1996) 131.
- [101] R. Scheeps, *Opt. Mater.* 7 (1997) 75.
- [102] H. Xu, L. Zhou, Z. Dai, and Z. Jiang, *Physica B* 342 (2002) 43.
- [103] Y. Li, G. Hong, Y. Zhan, and Y. Yu, *J. Alloys and Comp.* 456 (2008) 247.
- [104] G. Qin, J. Lu, J. F. Bisson, U. Feng, K-I. Ueda, H. Yagi, and T. Tamgotamo, *Solid State Comm.* 132 (2004) 103.
- [105] J. A. Capobianco, F. Vetrone, J. C. Boyer, A. Speghini, and M Bettinelli, *J. Phys. Chem. B* 106 (2002) 1181.
- [106] F. Vetrone, J. C. Boyer, J. A. Capobianco, A. Speghini, and M. Bettinelli, *J. Phys. Chem. Mater.* 15 (2003) 2737.
- [107] H. Xu, L. Zhou, Z. Dai, and Z. Jiang, *Physica B* 324 (2002) 43.
- [108] T. T. Basiev, Y. V. Orlovskii, K. K. Pukhov, V. B. Sigachev, M. E.

- Doroshenko, and I. N. Vorobvev, *J. Lumin.* 68 (1996) 241.
- [109] M. Pollnau, D. R. Gamelin, S. R. Luthi, H. U. Gudel, and M. P. Hehlen, *Phys. Rev. B*, 61 (2000) 3337.
- [110] J. S. Chivian, W. E. Case, and D. D. Eden, *Appl. Phys. Lett.* 35 (1979) 124.
- [111] I. I. Leonidov, V. G. Zubkov, A. P. Tyutyunnik, N. V. Tarakina, L. L. Surat, O. V. Koryakova and E. G. Vovkotrub, *J. Alloys Compd.* 509 (2011) 1339.
- [112] E. Downing, L. Hesselink, J. Ralston and R. Macfarlane, *Science* 273 (1996) 1185.
- [113] G. Morgan, S. Dad and A. C. Mitchell, *J. Alloys Compd.* 451 (2008) 526.
- [114] I. Gugov, M. Muller and C. Russel, *J. Solid State Chem.* 184 (2011) 1001.
- [115] G. Blasse and B. C. Grabmaier, "Luminescent Materials" (Springer, Berlin, 1994) p. 195.
- [116] F. Auzel and B. Di Bartolo, "Spectroscopy and Dynamics of Collective Excitations in Solids" (Springer, Berlin, 1997) p. 537.
- [117] M. Malinowski, Z. Frukacz, M. F. Joubert and B. Jacquier, *J. Lumin.* 75 (1997) 333.
- [118] I. R. Martí'n, V. D. Rodri'guez, V. Lavi'n and U. R. Rodri'guez-Mendoza, *J. Lumin.* 72–74 (1997) 954.
- [119] B. Simondi-Teisseire, B. Viana, D. Vivien and A. M. Lejus, *Opt. Mater.* 6 (1996) 267.
- [120] J. A. Hutchinson, H. R. Verdun, B. H. T. Chai and L. D. Merkle, *Opt. Mater.* 3 (1994) 287.
- [121] E. Cantelar and F. Cusso, *Appl. Phys. B* 69 (1999) 29.

- [122] S. Ivanova and F. Pelle', *J. Opt. Soc. Am. B* 26 (2009) 1930.
- [123] N. Yamada, S. Shionoya and T. Kushida, *J. Phys. Soc. Jpn.* 32 (1972) 1577.
- [124] E. Cantelar, J. A. Sanz-García and F. Cusso, *J. Cryst. Growth* 205 (1999) 196.
- [125] X. Changfu, Y. Qibin, R. Guozhong and L. Yunxina, *J. Alloys Compd.* 503 (2010) 82.
- [126] S. Hinojosa, O. Barbosa-García, M. A. Meneses-Nava, J. L. Maldonado, E. de la Rosa-Cruz and G. Ramos-Ortiz, *Opt. Mater.* 27 (2005) 1839.
- [127] Y. P. Li, J. H. Zhang, X. Zhang, Y. S. Luo, X. G. Ren, H. F. Zhao, X. J. Wang, L. D. Sun and C. H. Yan, *J. Phys. Chem. C* 113 (2009) 4413.
- [128] G. De, W. Qin, J. Zhang, J. Zhang, Y. Wang, C. Cao and Y. Cui, *J. Lumin.* 119–120 (2006) 258.
- [129] E. de la Rosa, D. Solís, L. A. Díaz-Torres, P. Salas, C. Angeles-Chavez and O. Meza, *J. Appl. Phys.* 104 (2008) 103508.
- [130] D. Solís, T. López-Luke, E. De la Rosa, P. Salas and C. Angeles-Chavez, *J. Lumin.* 129 (2009) 449.
- [131] P. Salas, C. Angeles-Chavez, J. A. Montoya, E. De la Rosa, L. A. Díaz Torres, H. Desirena, A. Martínez, M. A. Romero-Romo and J. Morales, *Opt. Mater.* 27 (2005) 1295.
- [132] G. Y. Chen, G. Somesfalean, Y. Liu, Z. G. Zhang, Q. Sun and F. P. Wang, *Phys. Rev. B* 75 (2007) 195204.
- [133] N. Claussen and J. Jahn, *J. Am. Ceram. Soc.* 61 (1978) 94.
- [134] T. K. Gupta, F. F. Lauge and J. H. Bechtold, *J. Mater. Sci.* 13 (1978) 1464.

- [135] B. K. Moon, I. M. Kwon, J. H. Jeong, C. S. Kim, S. S. Yi, P. S. Kim, H. Y. Choi and J. H. Kim, *J. Lumin.* 122–123 (2007) 855.
- [136] G. Seeta Rama Raju and S. Buddhudu, *Mater. Lett.* 62 (2008) 1259.
- [137] F. Vetrone, J. Boyer, J. A. Capobianco, A. Speghini and M. Bettinelli, *J. Appl. Phys.* 96 (2004) 661.
- [138] H. W. Song, B. J. Sun, T. Wang, S. Z. Lu, M. Ybng, B. J. Chen, X. J. Wang and X. G. Kong, *Solid State Commun.* 132 (2004) 409.
- [139] F. Pandozzi, F. Vetrone, J. Boyer, R. Naccache, J. A. Capobianco, A. Speghini and M. Bettinelli, *J. Phys. Chem. B* 109 (2005) 17400.
- [140] G. S. Yi and G. M. Chow, *J. Mater. Chem.* 43, 4460 (2005).
- [141] Q. Y. Zhang, T. Li, Z. H. Jiang, and S. Buddhudu, *Appl. Phys. Lett.* 87 (2005) 171911.
- [142] D. Lande, S. S. Orlov, A. Akella, L. Hesselink, and R. R. Neurgaonkar, *Opt. Lett.* 22 (1997) 1722.
- [143] S. Tanabe, H. Hayashi, T. Hanada, and N. Onodera, *Opt. Mater.* 19 (2002) 343.
- [144] H. R. Zheng, D. L. Gao, X. Y. Zhang, E. J. He, and X. S. Zhang, *J. Appl. Phys.* 104 (2008) 013506.
- [145] V. K. Tikhomirova, C. Gorller-Walranda, and K. Driesen, *J. Alloys Compd.* 451 (2008) 542.
- [146] X. X. Luo and W. H. Cao, *Mater. Lett.* 61 (2007) 3696.
- [147] J. C. Boyer, F. Vetrone, J. A. Capobianco, A. Speghini, and M. Bettinelli, *Chem. Phys. Lett.* 390 (2003) 403.

- [148] A. V. Kiryanov, V. Aboites, A. M. Belovolov, M. I. Timoshechkin, M. I. Belovolov, M. J. Damzen, and A. Minassian, *Opt. Express* 10 (2002) 832.
- [149] F. Lahoz, I. R. Martl, and A. Briones, *J. Appl. Phys.* 95 (2004) 2957.
- [150] X. Y. Huang and G. F. Wang, *J. Lumin.* 130 (2010) 1702.
- [151] A. Patra, S. Szha, M. Alencar, M. Rakov and G. Naciel, *Chem. Phys. Lett.* 407 (2005) 477.
- [152] S. Heer, M. Wermuth, K. Kamaer, D. Ehrentraut and H. Gudel, *J. Lumin.* 94 (2001) 337.
- [153] J. Boyer, F. Vetrone, J. Capobianco, A. Speghini, M. Zambelli and M. Bettinelli, *J. Lumin.* 105 (2004) 263.
- [154] L. Wan, S. Lu, L. Sun, and X. Qu, *Opt. Mater.* 36 (2014) 628.
- [155] G. Chen, H. Liu, G. Somesfalean, Y. Sheng, H. Liang, Z. Zhang, Q. Sun, F. Wang, *App. Phys. Lett.* 92 (2008) 113114.
- [156] J. Chung, J. Ryu, S. Lee, S. Kang, C. Shim, *Ceramics Int.* 39(2) (2013) 1951.
- [157] M. Treadaway and R. Powell, *J. Chem. Phys.* 61 (1974) 4003.
- [158] L. Bardelli, M. Bini and P. Bizzeti, *Nucl. Instrum. Meth.* A569 (2006) 743.
- [159] H. Wang, F. Medina, Y. Zhou and Q. Zhang, *Phys. Rev. B* 45 (1992) 10356.
- [160] T. Thongtem, A. Phuruangrat, and S. Thongtem, *Mater. Lett.* 62 (2008) 454.
- [161] J. Liu, J. Ma, M. Lin, Y. Ren, X. Jiang, J. Tao and X. Zhu, *Ceramics Int.* 34 (2008) 1557.
- [162] R. D. Shannon. "Revised Effective Ionic Radii and Systematic Studies of Interatomic Distances in Halides and Chalcogenides" (*Acta Crystallographica*,

U.S.A, 1976).

[163] J. Liao, B. Qiu, H. Wen, J. Chen, W. You and L. Liu, *J. Alloys Compd.* 487 (2009) 758.

[164] T. Thongtem, A. Phuruangrat and S. Thongtem, *Mater. Lett.* 62 (2008) 454.

[165] T. Thongtem, A. Phuruangrat and S. Thongtem, *Appl. Surf. Sci.* 254 (2008) 7581.

[166] M. Pollnau, D. R. Gamelin, S. R. Luthi, and H. U. Gudel, *Phys. Rev. B* 61(5) (2000) 3337.

[167] G. Chen, H. Liu, H. Liang, G. Somesfalean and Z. Zhang, *J. Phys. Chem. C.* 112 (2008) 12030.

[168] Y. Bai, Y. Wang, K. Yang, X. Zhang, G. Peng and Y. Song, *J. Phys. Chem. C.* 112 (2008) 12259.



감사의 글

먼저 박사학위논문을 준비하는 동안 아낌없는 지원과 조언으로 지도해주신 정중현 지도 교수님께 깊은 감사의 말씀을 올립니다. 부족한 저에게 많은 가르침을 주시고 연구에 집중할 수 있는 환경을 만들어 주셔서 정말 감사합니다. 학위논문을 작성하면서 많은 어려움에 처했을 때 아낌없는 조언과 지도 해주신 동의대학교 김중환 교수님께 감사 드립니다.

논문 심사위원으로서 연구의 방향과 보완점을 조언해주신 최병춘 교수님, 항상 웃으며 격려해 주시는 문병기 교수님, 부족한 부분이 많은데도 밝은 미소로 많은 조언해 주신 창원대학교 장기완 교수님께도 깊은 감사의 말씀을 전합니다. 또한 저의 연구에 많은 관심과 조언 아끼지 않으신 신라대학교 이성수 교수님, 언제나 웃으며 좋은 기도 많이 해주시는 동의대학교 최혜영 교수님께도 감사 드립니다.

실험실 생활을 하는 동안 많은 조언과 도움을 주신 심규성 박사님, 양현경 박사님, 김동유 박사님께 감사 드립니다. 또한 연구실 선배로서 각자의 분야에서 연구원으로 활동하고 있는 박성욱 선배님, 정종원 선배님, 연구의 막힘이 있을 때 많은 질문에도 웃으며 조언해 준 박진영 선배님, 정홍채 선배님에게도 감사합니다.

여자가 혼자밖에 없어 삭막했던 연구실에 활기를 불어넣어 준 서연우 언니와 김은옥, 힘들고 지치는 일이 많았지만 함께 연구하고 어울려 다니며 많은 추억을 만들 수 있게 해주어 고맙다고 전하고 싶습니다. 같이 학위논문을 준비한 권숙현, 이주현 그리고 같은 연구실에서 많은 일을 도와준 오주현에게도 고맙습니다.

박사학위논문을 완성하기 까지 정말 많은 사람들의 도움이 있었습니다. 그 부분을 마음에 새기어 앞으로의 연구에 최선을 다하겠습니다.

지금 이 순간 '감사의 글'을 적기까지 많은 일이 있었습니다. 사랑하는 사람과 결혼을 해서 평생 함께하는 멋진 동반자가 생겼고 부모님만큼 저를 사랑해 주시는 시부모님을 만났습니다. 옆에서 많은 도움과 사랑 주셔서 진심으로 감사합니다.

제가 여기까지 올 수 있었던 것은 항상 믿고 아낌없는 사랑을 주신 부모님 덕분입니다. 정말 감사 드리고 사랑합니다. 그리고 새로운 가정을 꾸려 행복한 신혼생활을 하고 있는 동생 태영이에게도 고맙습니다. 지금 이 마음 변치 않고 앞으로 많은 사람들에게 보답할 수 있도록 노력하겠습니다.



2014년 7월
노현미 올림